

# **Robust and Cost-effective Vehicle Sideslip Estimation by using GPS**

by

Jong-Hwa Yoon

A dissertation submitted in partial fulfillment  
of the requirements for the degree of  
Doctor of Philosophy  
(Mechanical Engineering)  
in The University of Michigan  
2013

Doctoral Committee:

Professor Huei Peng, Chair  
Professor Noel C. Perkins  
Professor Timothy J. Gordon  
Assistant Professor Ryan M. Eustice

© Jong-Hwa Yoon

---

2013

## ACKNOWLEDGEMENTS

First of all, I would like to thank to my advisor, Professor Huei Peng, for his guidance and mentoring. His keen insight has given me academic challenges all the time and that provides me with continual inspiration throughout my doctoral research. Every time when I was stuck for progress, he guided me to the right path with patience. I also thank to my committee members. Comments from Professor Timothy J. Gordon were full of constructive criticism and his rich knowledge on vehicle dynamics deepened my research. Discerning insights of Professor Noel C. Perkins on dynamics and sensor signal processing broadened my perspective. Professor Ryan M. Eustice amazed me with abundant knowledge on the stochastic system and the Kalman filtering. He was always full of smart ideas and my dissertation became more elegant by virtue of them.

I owe a debt of gratitude to TRW Automotive for its financial support and test equipments. I owe a special thanks to Danny Milot. Without his support and understanding, my work would have been almost impossible. I also thank to my colleagues of TRW Automotive for general support: Kevin Fontenot, Jeremy Reeves, John Hildebrand, Scott Grit, Chuck Bartlett, Mandy McIvor, Seth Bunin, Som Khamly, Tim Sullivan, and Dr. Mark Elwell.

I want to express my gratitude to my colleagues at the University of Michigan's Vehicle Dynamics Lab (VDL). Many thanks Chiao-Ting Li, William Smith, Byung-Joo Kim, Tianyou Guo, Ding Zhao, Xiaowu Zhang, Ziheng Pan, and Dr. Changsun Ahn for sharing enthusiastic discussions.

Finally, I would like to express my loving appreciation to my family. My wife, Na Young Park, and two sons, Luke Yoon and Sean Yoon. Their existence makes my life meaningful and their love sustained me during my doctoral study. My biggest debt is owed to my mother, Dongsuk Choi. Without her lifetime sacrifice and love, I could never have made it to where I am today.

## TABLE OF CONTENTS

ACKNOWLEDGEMENTS .....	ii
LIST OF FIGURES .....	v
LIST OF TABLES .....	x
NOMENCLATURE .....	xi
ABSTRACT.....	xv
CHAPTER 1 INTRODUCTION .....	1
1.1 Motivation.....	1
1.2 Literature Review .....	4
1.3 Problem Definition.....	12
1.4 Thesis Contributions .....	14
1.5 Thesis Organization .....	14
CHAPTER 2 GLOBAL POSITIONING SYSTEM (GPS) .....	16
2.1 Introduction.....	16
2.2 GPS: Potentials and Changing Circumstances.....	20
2.3 GPS: Velocity Measurements .....	22
2.4 Summary .....	25
CHAPTER 3 SENSOR FUSION THROUGH KALMAN FILTER.....	26
3.1 Kalman Filter .....	26
3.2 Stochastic Observability.....	30
3.3 Sensor Fusion through Kalman Filter .....	33
3.4 Summary .....	36
CHAPTER 4 SIDESLIP ANGLE ESTIMATION USING VELOCITY MEASUREMENTS FROM TWO GPS ANTENNAE .....	37
4.1 Introduction.....	37
4.2 Kinematic Approach .....	38
4.3 Singularity Analysis of the Kinematic Approach .....	39

4.4 Sensor Fusion through the Kalman Filter .....	45
4.5 Experimental Verification.....	57
4.6 Discussion .....	66
CHAPTER 5 MERGING GPS AND IMU WITH A MAGNETOMETER .....	69
5.1 Introduction.....	69
5.2 Heading Angles from a Magnetometer.....	70
5.3 Stochastic Filter to Reject Magnetic Field Disturbances .....	73
5.4 Sensor Fusion through the Kalman Filter .....	82
5.5 Observability Analysis .....	86
5.6 Simulations and Experimental Results.....	90
5.7 Discussions.....	104
CHAPTER 6 CONCLUSIONS AND FUTURE WORK.....	109
6.1 Conclusions .....	109
6.2 Future Work .....	110
APPENDICES .....	112
BIBLIOGRAPHY .....	130

## LIST OF FIGURES

Figure 1.1 Top view of a vehicle .....	2
Figure 1.2 Tire lateral force and sideslip angle.....	3
Figure 1.3 The bicycle model .....	5
Figure 1.4 The Heading( $\psi$ ), Course( $\gamma$ ), and Sideslip( $\beta$ ) angles.....	10
Figure 1.5 Schematic classification of the methods identified in the literature review .....	12
Figure 2.1 GPS Constellation <a href="http://quest.arc.nasa.gov/">http://quest.arc.nasa.gov/</a> .....	16
Figure 2.2 Principle of Differential GPS(DGPS).....	18
Figure 2.3 Principle of Carrier-Phase Differential GPS (CDGPS).....	18
Figure 2.4 CDGPS: heading angle measurement .....	19
Figure 2.5 Maximum horizontal position errors (HPE) in meters .....	21
Figure 2.6 The Allan Variance plot of the GPS velocity error (U-blox LEA 5).....	22
Figure 2.7 GPS performance vs. price; (a) velocity, (b) update rate, (c) position .....	24
Figure 3.1 Top view of the bivariate normal distribution.....	27
Figure 3.2 Discrete Kalman filter framework for delay handling .....	34
Figure 3.3 Schematic diagram of unsynchronized updates from two sensors. ....	35
Figure 4.1 Top view of a ground vehicle with two GPS receivers on the horizontal plane .....	38
Figure 4.2 Top view of two vehicles with different yaw angles when yaw rate is zero.....	40
Figure 4.3 Accuracy of (a) yaw angle and (b) sideslip angle measurement from two GPS velocities as a function of yaw rate and longitudinal velocity.....	42

Figure 4.4 Monte-Carlo simulation results: (a) yaw/sideslip angle estimation with the presence of Gaussian white noise in the GPS velocity measurement (b) standard deviation of estimation error as a function of yaw rate .....	44
Figure 4.5 Schematic diagram of the measurement .....	46
Figure 4.6 Delays in GPS velocity measurement .....	46
Figure 4.7 A typical velocity profile from two GPS receivers .....	47
Figure 4.8 Schematic diagram of the two-GPS method. Equations (4.1)-(4.4) and (4.11)-(4.13) are used. ....	49
Figure 4.9 $\alpha_o, \beta_o, \alpha_c,$ and $\beta_c$ of J-turn.....	52
Figure 4.10 The minimum eigen value ( $\alpha_o$ ) of $O(k, k - N)$ and its corresponding yaw rate of a J-turn maneuver .....	53
Figure 4.11 The minimum eigen value ( $\alpha_o$ ) of $O(k, k - N)$ and its corresponding yaw rate of a single lane change maneuver.....	54
Figure 4.12 The minimum eigen value ( $\alpha_o$ ) of $O(k, k - N)$ and its corresponding yaw rate of a double lane change maneuver.....	55
Figure 4.13 The minimum eigen value ( $\alpha_o$ ) of $O(k, k - N)$ and its corresponding yaw rate of a slalom maneuver.....	55
Figure 4.14 The vehicle sideslip angle estimation by a bicycle model with parameters of 25%~175% of nominal values. ....	56
Figure 4.15 Test Maneuver: steering angle and vehicle speed .....	58
Figure 4.16 The wet tile surface of the TRW proving ground (Locke Township, MI).....	58
Figure 4.17 Experimental result; (a) yaw angle estimation, (b) sideslip angle estimation, (c)  yaw rate .....	59
Figure 4.18 Sideslip estimation performance with single lane change on (a) asphalt and (c) wet tile surfaces. (b) and (d) are absolute values of corresponding yaw rates .....	62

Figure 4.19 Sideslip estimation performance with double lane change on (a) asphalt and (c) wet tile surfaces. (b) and (d) are absolute values of corresponding yaw rates .....	63
Figure 4.20 Sideslip estimation performance with slalom on (a) asphalt and (c) wet tile surfaces. (b) and (d) are absolute values of corresponding yaw rates .....	64
Figure 4.21 Sideslip estimation performance with J-turn on (a) asphalt and (c) wet tile surfaces. (b) and (d) are absolute values of corresponding yaw rates .....	65
Figure 4.22 Distribution of roll angles during slalom.....	66
Figure 4.23 Rear view of a vehicle on a banked road.....	67
Figure 5.1 The Earth's magnetic field .....	71
Figure 5.2 Top view of four coordinate frames .....	71
Figure 5.3 Two different attitudes with one given reference vector.....	73
Figure 5.4 Highway data. Magnetic fields are measured when vehicle runs straight. ....	74
Figure 5.5 A correlation plot between yaw angle error and deviation of magnetic field norm from unity. The yaw angle is calculated from magnetometer measurements only.....	75
Figure 5.6 Enlarged view of Figure 5.4 (b). $W$ is the heading angle error induced by magnetic disturbances.....	76
Figure 5.7 The uniform distribution to describe the heading angle errors induced by magnetic disturbances .....	76
Figure 5.8 Truncated normal distributions with three different standard deviations. The truncated normal distribution whose standard deviation is ten times larger than the bound greatly resembles the uniform distribution. ....	78
Figure 5.9 Schematic diagram of the dual Kalman filters .....	82
Figure 5.10 $\alpha_o$ , $\beta_o$ , $\alpha_c$ , and $\beta_c$ of the Heading Kalman filter.....	87
Figure 5.11 $\alpha_o$ and the absolute value of yaw rate .....	87



Figure 5.12	$\alpha_o, \beta_o, \alpha_c,$ and $\beta_c$ of the Sideslip Kalman filter .....	88
Figure 5.13	$\alpha_o, \beta_o, \alpha_c,$ and $\beta_c$ of the Sideslip Kalman filter after removing the longitudinal/lateral biases from the state .....	89
Figure 5.14	The layout of the simulating ‘test track’ .....	90
Figure 5.15	Simulation results; (a) deviation of magnetic field norm due to injected disturbances, (b) yaw angle estimation, and (c) roll angle estimation. ....	92
Figure 5.16	The sideslip angle estimation performance on different friction and road bank levels; (a) flat asphalt, (b) banked asphalt, (c) flat ice, and (d) banked ice. ....	93
Figure 5.17	The sideslip angle estimation performance with and without magnetic disturbance rejection logic. ....	94
Figure 5.18	Accelerometer bias estimation performance .....	95
Figure 5.19	The test vehicle (GM Silverado) with equipment. (Left) The GPS receivers is located on the roof of the vehicle, (Center) The Oxford RT2500 is installed in the vehicle, (Right) The magnetometer is installed on the rear of the vehicle. ....	96
Figure 5.20	The sideslip estimation performance of on-track experiments; (a) single lane change (SLC), (b) double lane change (DLC), (c) slalom (SLL), and (d) J-turn .....	98
Figure 5.21	The sideslip estimation performance of on-track experiments of single lane change (SLC), double lane change (DLC), slalom (SLL) and J-turn with and without magnetic disturbance rejection. Results from 20 runs with disturbance of [0.05,1] at 20%. ....	99
Figure 5.22	The roll angle estimation performance of on-track experiments; single lane change (SLC) and slalom (SLL) .....	100
Figure 5.23	Top view of the neighborhood area used for test (Kinross, Michigan) .....	101

Figure 5.24 An example of steering angle, yaw rate, and vehicle speed during neighborhood area experiments.....	101
Figure 5.25 The sideslip estimation performance in the neighborhood area experiments.....	102
Figure 5.26 A neighborhood experiment data showing error source.....	103
Figure 5.27 Comparison of road pitch angles and magnetic field noise. Red dots represent the neighborhood area and blue dots the on-track area. ....	104
Figure 5.28 Magnetic field disturbance detection/rejection performance comparison.....	107
Figure 5.29 Magnetic field disturbance detection/rejection performance comparison. 4 deg/sec bias is injected to yaw rate measurements from 120 sec to 145 sec.....	108
Figure A.1 Graphical procedures for Allan Variance plot: (a) Time-series data when a sensor is free-from excitation, (b) Clustering of time-series data, (c) Average calculation of each cluster.....	108
Figure A.2 Allan Variance for various error dynamics (Adapted from [1] ) .....	108
Figure A.3 Allan variance plots of three dimensional velocities from U-blox LEA 5: (a) X direction in ECEF, (b) Y-direction, and (c) Z-direction.....	108
Figure C.1 Top view of bivariate normal-uniform distribution.....	121
Figure D.1 Top view of the bivariate normal-truncated normal distribution .....	122
Figure E.1 Top view of linear combination of two random variables .....	126
Figure F.1 Norm of the magnetic field collected on a section of Michigan highway (I-75) .....	129

## LIST OF TABLES

Table 1.1 Literature review summary – sideslip angle estimation methods .....	11
Table 2.1 GPS positioning error sources .....	17
Table 4.1 The standard deviation of sideslip angle measurement error.....	43
Table 4.2 Comparison of GPS and IMU signals.....	45
Table 4.3 Test vehicle parameters (small size pickup truck - unloaded).....	57
Table 4.4 Test vehicle parameters used in the robustness test (a sports car) .....	61
Table 5.1 Stochastic properties of the joint normal-truncated normal distribution .....	79
Table 5.2 Simulation properties .....	91
Table 5.3 The performance with different disturbance levels .....	99
Table A.1 Summary of standard error sources and Allan variance slopes (Adapted from [1]).....	114
Table B.1 $\left  \frac{RT_{xx}}{LT_{xx}} \right $ as a function of yaw rate .....	119
Table F.1 Percentage of the ‘useful’ area .....	129

## NOMENCLATURE

Symbol	Meaning
$\alpha$	Tire sideslip angle
$\beta$	Vehicle sideslip angle at Center of Gravity (CG)
$\alpha_{of}, \alpha_{or}$	Tire sideslip angle of outside front and outside rear wheels
$\alpha_{if}, \alpha_{ir}$	Tire sideslip angle of inside front and inside rear wheels
$f_{yof}, f_{yor}$	Lateral tire force at outside front and outside rear wheels
$f_{yif}, f_{yir}$	Lateral tire force at inside front and inside rear wheels
$\delta$	Steer angle
$\gamma$	Vehicle course angle
$\psi$	Vehicle heading (yaw) angle
$\dot{\psi}$	Vehicle yaw rate
$C_f, C_r$	Cornering stiffness, Front & Rear
$U$	Vehicle longitudinal velocity
$V$	Vehicle lateral velocity
$D_f, D_r$	Distance from CG to front/rear axle
$F_{f,x}, F_{r,x}$	Longitudinal tire force, Front & Rear
$F_{f,y}, F_{r,y}$	Lateral tire force, Front & Rear
$m$	Vehicle mass
$I_z$	Vehicle moment of inertial with respect to Z axis

Symbol	Meaning
$a_{xm}, a_{ym}$	Measured longitudinal/lateral accelerations
$r_m$	Measured yaw rate
$V_{CG}$	Horizontal vehicle velocity at CG
$\lambda$	Wave length of GPS signal
$\sigma$	Standard deviation
$\mu$	Mean
$\rho$	Correlation coefficient of two random variables
$x_k$	True state at time step k
$\hat{x}_k^-$	State estimate before measurement correction at time step k
$\hat{x}_k^+$	State estimate after measurement correction at time step k
$e_k$	State estimate error ( $x_k - \hat{x}_k^+$ )
$u_k$	Input at time step k
$w_k$	plant noise at time step k
$z_k$	Measurement at time step k
$v_k$	Measurement noise at time step k
$\Phi_{k,k-1}$	State transition matrix from time step k-1 to k
$\Gamma_k, \Lambda_k$	Input matrix and plant error matrix at time step k
$H_k$	Measurement matrix at time step k
$P_k^-$	State error covariance matrix before measurement update
$P_k^+$	State error covariance matrix after measurement update
$Q_k$	Plant noise covariance matrix
$R_k$	Measurement noise covariance
$\sigma(A)$	Singular values of a matrix A

Symbol	Meaning
<i>BIBO</i>	Bounded Input Bounded Output
<i>H.O.T</i>	Higher Order Terms
$V_{fe}, V_{fn}$	Velocity measurement of the front GPS receiver, East & North
$V_{re}, V_{rn}$	Velocity measurement of the rear GPS receiver, East & North
$L_f, L_r$	Distance from CG to front/rear GPS
$L$	Distance from front to rear GPS, $(L_f + L_r)$
$b_x, b_y, b_r$	Biases in the IMU measurements (longitudinal/lateral acceleration and yaw rate)
$w_x, w_y, w_r$	Noise in the IMU measurements (longitudinal/lateral acceleration and yaw rate)
<i>SLC</i>	Single Lane Change
<i>DLC</i>	Double Lane Change
<i>SLL</i>	Slalom
<i>RMS</i>	Root-Mean-Square
<i>G-frame</i>	Geographic Earth-fixed frame. X points to the geographic North
<i>M-frame</i>	Magnetic Earth-fixed frame. X points to the magnetic North
<i>v-frame</i>	Vehicle-fixed moving frame.
<i>s-frame</i>	Sensor-fixed moving frame.
$m_x, m_y, m_z$	The Earth's magnetic field measured in the s-frame
$M_x, M_y, M_z$	The Earth's magnetic field in the M-frame
$\psi_m, \theta_m, \phi_m$	Yaw, pitch, and roll angles of the magnetometer with respect to the M-frame
$\psi_o, \theta_o, \phi_o$	Offsets in yaw, pitch, and roll angles needed to convert angles of a magnetometer in the M-frame to angles of a vehicle in the G-frame
$W$	Random variable for yaw error induced by magnetic disturbance

Symbol	Meaning
$\varepsilon(\cdot)$	Expected value of a random variable
$N(\mu, \sigma)$	Normal distribution with mean and standard deviation
$U(-b_o, b_o)$	Uniform distribution with bound of $\pm b_o$
$cov(x, y)$	Covariance of random variables x and y
$g$	Gravity acceleration
$V_N^{GPS}, V_W^{GPS}, V_U^{GPS}$	GPS velocities in the G-frame; North, West, and Upward
$U^{GPS}, V^{GPS}, V_v^{GPS}$	GPS velocities in the v-frame; Longitudinal, Lateral, and Vertical

## ABSTRACT

Electronic Stability Control (ESC) is an effective active safety system that has become standard equipment on modern passenger vehicles. When a vehicle path begins to deviate from the driver's steering intention, ESC applies differential braking to secure driver's control authority. ESC is known to save lives by preventing vehicle rollover accidents. The vehicle sideslip angle is defined by the angle formed between longitudinal and lateral velocities and it is critical information for the operation of ESC.

In spite of tremendous research efforts, a practical method guaranteeing accurate estimation of vehicle slip angle has not been fully developed yet. Vehicle dynamic model-based methods work for only small sideslip angles (4 degree or less). Estimation performance of the Inertial Measurement Unit (IMU) integration-based methods is drastically deteriorated by unknown sensor bias and drift. The Global Positioning System (GPS)-based methods struggle to provide a cost effective method that meets the performance requirements of ESC.

The author proposed two low-cost GPS-based methods; (1) a two-GPS method and (2) a GPS/magnetometer-based method. The two-GPS method utilizes the kinematic coupling of velocities of two GPS receivers to extract vehicle yaw angles. This yaw angle is combined with the course angle measured by GPS velocity to yield the vehicle sideslip angle. As low-cost GPS has low update rate, GPS measurements are merged with fast updating IMU signals through the Kalman filter. The significant latency in GPS measurement and the unsynchronized update of two GPS receivers are two technical challenges. They are addressed by the 'measurement shift' and the 'asynchronous' measurement update techniques. The stochastic observability analysis reveals that this method can observe the sideslip only when a vehicle turns; hence GPS measurements are discarded during straight driving. For design verification, a mid-size pickup truck was equipped with two GPS receivers along with an IMU and several J-turns were conducted on a wet-tile surface. For robustness verification purpose, four maneuvers of single lane



change, double lane change, slalom, and J-turn were run on high/mid/low frictional surfaces with a sports car.

The GPS/magnetometer-based method combines measurements of a magnetometer with GPS to estimate vehicle sideslip angles. The Earth's magnetic field measured by a magnetometer contains yaw, pitch and roll angles of a vehicle. Vehicle yaw and roll angles are extracted through an Extended Kalman Filter (EKF) which merges measurements of a magnetometer and IMU. Along with the obtained yaw/roll angles, GPS velocities are combined with acceleration measurements of the IMU to yield the vehicle sideslip estimation. A magnetometer is known to be susceptible to large disturbances. This concern is addressed by a new stochastic filter rejecting disturbances. This new filter is based on the bivariate normal-uniform distribution and is integrated on the Kalman filter frame work. Stochastic observability analysis reveals that that sideslip angle is observable only when a vehicle turns; hence a bicycle model is employed during straight driving. For design verification, a simulation study was conducted using Carsim<sup>TM</sup>. Four types of maneuvers were combined with two friction types and two road bank types. The sideslip estimation stayed close to the true value regardless of friction type and road bank angles. For robustness verification, experimental verifications were run in two ways. One method was to run pre-defined maneuvers on a test track, and the other was to drive the vehicle in a neighborhood area emulating daily driving. A fully equipped GM Silverado truck was used. On-track data showed an RMS error of  $1.3^{\circ}$  and neighborhood area data had an RMS of  $1.67^{\circ}$ . The performance was degraded from the simulation because the method did not fully account for road pitch angles and the magnetic field was noisy in general.

The vehicle sideslip estimation is challenging task because of the tight requirement necessary for ESC, specifically an RMS error no greater than  $1.5^{\circ}$ . The GPS/magnetometer-based method showed the potential to meet the requirement. The estimation accuracy improvement will be pursued as future work. The author still believes GPS has a promising future in meeting this tight requirement because its reliability and accuracy will be boosted with help from the GALILEO.

# CHAPTER 1

## INTRODUCTION

### 1.1 Motivation

Electronic Stability Control (ESC) is a highly effective active safety system for ground vehicles. A study from the National Highway Traffic Safety Administration (NHTSA) reports that ESC can save 5,300~9,600 lives and prevent 156,000~238,000 injuries annually by preventing 71% of the passenger car rollovers and 84% of the sports utility vehicle (SUV) rollovers. This document prompted a new federal motor vehicle safety standard (FMVSS) No. 126 to require ESC systems on passenger cars, multipurpose passenger vehicle, trucks, and buses with a gross vehicle weight rating of 10,000 pounds or less by 2012 [2]. Increased interest in fuel efficient ground vehicles is another driving force for active safety systems like ESC. In the United States, average fuel economy needs to increase to 35.5 miles per gallon (mpg) by 2016; while today's average fuel economy is 27.3 mpg [3]. This requirement is likely to reduce vehicle weight by 10~20%. However, vehicle weight reduction is known to increase injury and fatality risk [4]. Therefore active safety systems such as ESC will become more important in the near future.

ESC is a technology that improves the safety of a vehicle by detecting and regulating sideslip, yaw rate error, and sometimes roll motions. When ESC detects loss of stability, it applies differential braking to affect vehicle yaw and/or roll motions. One requirement of ESC from FMVSS No. 126 [2] is that “*ESC has a means to determine vehicle yaw rate and to estimate its sideslip or the time derivative of sideslip*”. The sideslip angle is defined as the angle between the longitudinal axis and the direction of travel at any given point of the vehicle [5].

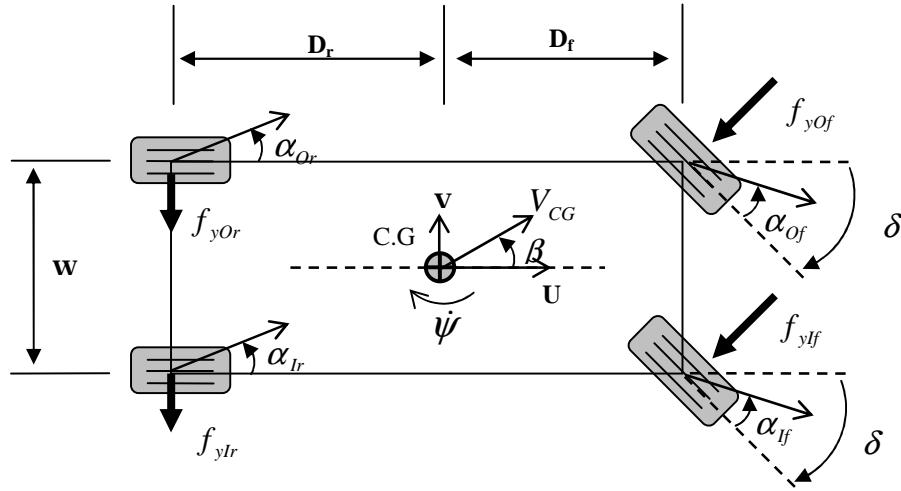


Figure 1.1 Top view of a vehicle

Figure 1.1 shows the top view of a ground vehicle. Five sideslip angles are displayed.  $\alpha_{of}, \alpha_{if}$  are the tire sideslip angles at the outside and inside front wheels, respectively.  $\alpha_{or}, \alpha_{ir}$  are the tire sideslip angles at the outside and inside rear wheels, respectively.  $\beta$  is the sideslip angle at the vehicle's center of gravity (CG). It is referred to as the vehicle sideslip angle. All of the tire sideslip angles are expressed as functions of  $\{\beta, \psi, V_{CG}, \delta\}$  as indicated below:

$$\alpha_{if} = \tan^{-1}\left(\frac{V_{CG} \sin \beta - D_f \dot{\psi}}{V_{CG} \cos \beta - \frac{W}{2} \dot{\psi}}\right) + \delta \quad (1.1)$$

$$\alpha_{ir} = \tan^{-1}\left(\frac{V_{CG} \sin \beta + D_r \dot{\psi}}{V_{CG} \cos \beta - \frac{W}{2} \dot{\psi}}\right) \quad (1.2)$$

$$\alpha_{of} = \tan^{-1}\left(\frac{V_{CG} \sin \beta - D_f \dot{\psi}}{V_{CG} \cos \beta + \frac{W}{2} \dot{\psi}}\right) + \delta \quad (1.3)$$

$$\alpha_{Or} = \tan^{-1} \left( \frac{V_{CG} \sin \beta + D_r \dot{\psi}}{V_{CG} \cos \beta + \frac{W}{2} \dot{\psi}} \right) \quad (1.4)$$

At each wheel, non-zero tire sideslip angle means a deformed tire contact patch over the ground. Along with the elasticity of a tire, this deformation produces a lateral force. Those tire lateral forces are denoted by  $\{f_{yOf}, f_{yIf}, f_{yOr}, f_{yIr}\}$  in Figure 1.1

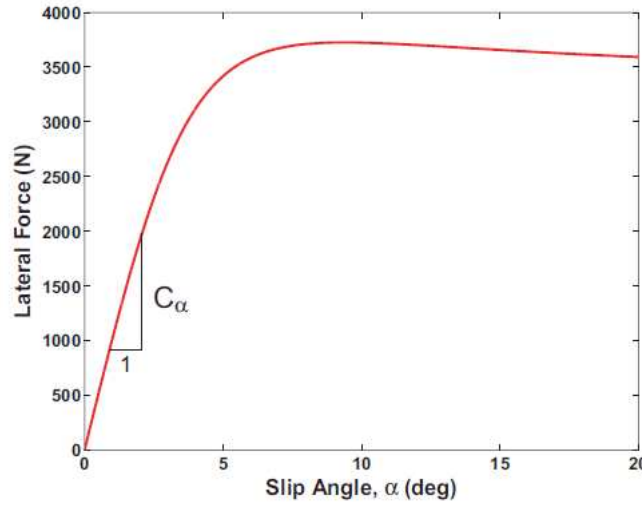


Figure 1.2 Tire lateral force and sideslip angle

Figure 1.2 shows a typical lateral force profile as a function of sideslip angle [5]. The graph in Figure 1.2 is henceforth referred to as ‘ $f_y$ -slip curve’. As can be seen, the relationship between the lateral force and the sideslip angle is nonlinear. However, at low slip angles (4 degrees or less) the relationship is quite linear. In this region the lateral force can be approximated by:

$$f_y = C_\alpha \alpha \quad (1.5)$$

where  $\alpha$  is the tire sideslip angle and  $f_y$  is the lateral tire force. The constant  $C_\alpha$  is known as the cornering stiffness. The cornering stiffness is dependent on many variables,

including tire size, wheel width, and tread pattern. When the sideslip angle is large, (1.5) is invalid. This area is called the nonlinear or saturated area.

When the vehicle sideslip angle ( $\beta$ ) is large, the tire sideslip angle at each wheel is large; hence the yaw moment and total lateral force become almost constant, regardless of steering angle. This significantly reduces the driver's authority in controlling the vehicle lateral/yaw motion. Therefore regulating and estimating vehicle sideslip angle is important.

Sideslip angle estimation is a challenging task in current ESC products. The standard ESC sensor set includes a steering angle sensor, wheel speed sensors, brake pressure sensor, and an inertial measurement unit (IMU). An IMU comprises longitudinal/lateral accelerometers and a yaw rate gyro. Although this sensor set has raised the performance of ESC in the current market to the safe-to-use level, sideslip estimation using this sensor set still contain a significant level of errors. The reasons for these errors will be explained in the next section. Uncertainties in sideslip angle estimation lead the ESC system to be conservatively calibrated in order to balance robustness concerns with performance. This inherently sacrifices some level of performance.

## **1.2 Literature Review**

Many approaches have been proposed to estimate the vehicle sideslip angle. These methodologies can be grouped into three categories; 'dynamic model-based', 'IMU-based', and 'GPS-based'. Detailed descriptions, advantages, and disadvantages of each methodology are presented in the following sub-sections.

### **1.2.1 Dynamic Model-based Methods**

Some researchers have developed methods to estimate the sideslip angle using vehicle dynamic models. Frequently a simple model such as the bicycle model is used. Figure 1.3 shows the bicycle model. This model assumes that no lateral load transfer takes place, hence reducing the vehicle to a single-track. For this model representation, the three 'degrees-of-freedom' are the motion variables;  $U$  (the longitudinal velocity),  $V$

(the lateral velocity) and  $\dot{\psi}$  (the yaw rate). The balance of forces in the longitudinal and lateral directions and the balance of yaw moments lead to (1.6)~(1.8), where ‘m’ is the vehicle mass and ‘ $I_z$ ’ is the yaw moment of inertia.  $D_f$  and  $D_r$  are the distances from the CG to the front/rear axles, respectively. With the assumption of small sideslip angles, the tire forces ( $F_{f,y}, F_{r,y}$ ) are related to slip angle via the cornering stiffness and the slip angle can be found in terms of U, V, and  $\dot{\psi}$  as (1.9) shows.

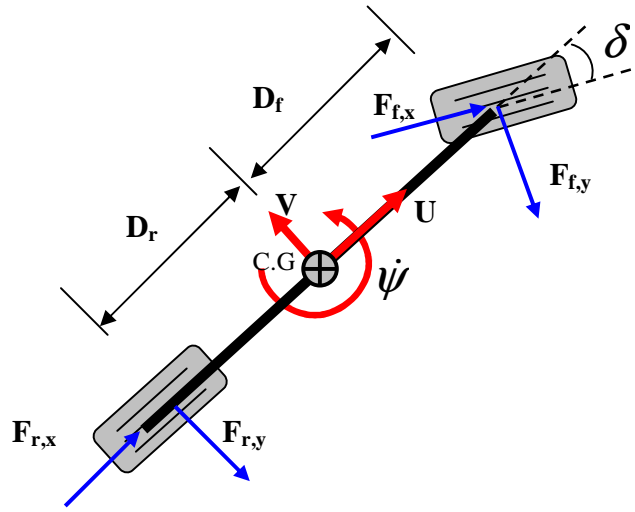


Figure 1.3 The bicycle model

$$F_{f,x} \cos \delta - F_{f,y} \sin \delta + F_{r,x} = m(\dot{U} - V\dot{\psi}) \quad (1.6)$$

$$F_{f,x} \sin \delta + F_{f,y} \cos \delta + F_{r,y} = m(\dot{V} + U\dot{\psi}) \quad (1.7)$$

$$F_{f,y} D_f \cos \delta + F_{f,x} D_f \sin \delta - F_{r,y} D_r = I_z \ddot{\psi} \quad (1.8)$$

$$F_{f,y} = C_f \left( \delta - \frac{V + D_f \dot{\psi}}{U} \right), \quad F_{r,y} = C_r \left( \frac{-V + D_r \dot{\psi}}{U} \right) \quad (1.9)$$

Substituting (1.9) into (1.6)~(1.8) leads to three nonlinear equations whose state vector is  $[U, V, \dot{\psi}]^T$ . This nonlinear equation set is useful for nonlinear observer design. Toward building a simpler dynamic model,  $F_{f,y}$ ,  $F_{r,y}$  in (1.7)~(1.8) are substituted with (1.9) and the longitudinal velocity (U) is assumed to be constant. Then a linearized equation is obtained:

$$\dot{x} = \begin{bmatrix} \frac{-C_f - C_r}{m} & \frac{-D_f C_f + D_r C_r - U}{mU} \\ \frac{-D_f C_f + D_r C_r}{I_z} & \frac{-D_f^2 C_f - D_r^2 C_r}{I_z U} \end{bmatrix} x + \begin{bmatrix} \frac{C_f}{m} \\ \frac{D_f C_f}{I_z} \end{bmatrix} \delta \quad (1.10)$$

Equation (1.10) ignores the longitudinal dynamics and the state vector is  $x = [V, \dot{\psi}]^T$ . This is used for the linear observer design. Farrelly [6] proposed a standard Luenberger observer of a linearized system with Kalman filter gains and Insensitive Observer gains. Kalman filter gains are selected for optimal noise rejection, and the Insensitive Observer gain is selected to enhance robustness against parameter uncertainties. Kiencke [7] showed the feasibility of a nonlinear observer. The nonlinear observer was found to outperform the linear observer in his work. Best [8] showed that simultaneous estimation of cornering stiffness enhanced sideslip angle estimation performance. Stephan [9] compared the estimation performance of four types of observers ( linear observer, extended Luenberger observer, extended Kalman filter, and sliding-mode observer) and concluded that nonlinear observers worked better than linear observers. Cherouat [10] also proposed a nonlinear observer. Unlike other methods, this observer did not require a yaw rate measurement. Yih [11] proposed to use steering torque information for sideslip angle estimation. This method would be useful for steer-by-wire systems. Gao [12] showed that a high-gain observer based on input-output linearization was useful. He validated the performance of his work with data of various maneuvers on high friction surfaces. Grip [13] proposed a nonlinear observer with friction adaptation. In his work, the friction model was parameterized with a single friction parameter and an update law was designed.

The aforementioned approaches, grouped as ‘dynamic model-based methods’, have demonstrated their capability to estimate sideslip angles. However, the dynamic model-based methods require accurate vehicle parameter information such as cornering stiffness, vehicle mass and moment of inertia [6, 14]. In the automotive industry, frequently only nominal parameter values are available. Since parameter variations exist due to aging, manufacturing variations, or various vehicle loads, it is usually hard to measure or estimate the true parameter values. This is why dynamic model-based methods are not always embraced by the automotive industry. Li [15] proposed a robust linear observer whose performance was not greatly affected by parameter variations. However, it assumed that accurate position measurements of front/rear axles were available. Another drawback of the dynamic model-based methods is that they work only for small sideslip angles (4 degree or less) [5]. This is due to the assumption of a linear relationship between lateral force and sideslip angle. Therefore when the sideslip angle becomes large, usability of the dynamic model-based methods dramatically reduces.

### 1.2.2 IMU-based Methods

Several other researchers have focused on processing IMU sensor measurements to calculate the sideslip angle. The longitudinal/lateral accelerations are kinematically coupled with  $\{U, V, \psi\}$  as shown below:

$$\dot{U} = a_x + V\dot{\psi} \quad (1.11)$$

$$\dot{V} = a_y - U\dot{\psi} \quad (1.12)$$

where  $a_x$  and  $a_y$  are the longitudinal and lateral accelerations. The basic idea is that longitudinal and lateral velocities can be obtained by integrating accelerometer measurements after  $V\dot{\psi}$  and  $U\dot{\psi}$  are removed. Farrelly was among the first groups using this method [6]. He showed that sideslip estimation was robust to cornering stiffness variations. It was also shown that this method worked for large sideslip angles, which is in the nonlinear area of the  $f_y$ -slip curve. Imsland [16] proposed a nonlinear observer



based on (1.11) ~ (1.12) and showed that the estimation performance was acceptable even at large sideslip angles. Ungoren [17] also confirmed the robustness of IMU-based method for various sideslip angle ranges.

The advantages of IMU-based methodology are (i) they do not require vehicle parameters such as cornering stiffness, mass, or moment of inertia, and (ii) they work well even for large sideslip angles. However, unknown bias in the sensor measurement can significantly deteriorate the estimation performance. Since the IMU-based methods heavily rely on integration of measurement, the effect of unknown bias deteriorates the performance significantly. Some researchers have combined the IMU-based methods with the dynamic model-based methods [14, 18-19]. The common idea of these hybrid methods is to use the dynamic model-based method when vehicle sideslip angle is small, and to use the sensor signal-based method for high vehicle sideslip angle. Although this combination attenuates the drawbacks of each method, the concern of parameter dependency and unknown bias still exist.

### 1.2.3 GPS-based Methods

Several researchers have used Global Positioning System (GPS) measurements for sideslip calculation. As GPS can measure vehicle speed via the Doppler Effect, the course angle (which is the angle of the moving direction) is easily obtained. Since the vehicle sideslip is calculated by subtracting the heading angle from the course angle, GPS-based methods are dedicated to accurate heading angle estimation

Bevly [20-23] developed a method of utilizing a single-antenna GPS receiver for sideslip angle estimation. His method essentially merged the velocity signal from a low-cost single-antenna GPS receiver with accelerations and yaw rate from an IMU. This method inherits concerns of inaccurate sensor bias estimation due to its dependence on IMU integration for heading angle calculation. Additionally this method does not account for a vehicle running on banked roads. Anderson [24] enhanced Bevly's work by merging the velocity of a single-antenna GPS receiver with a dynamic model. These methods are categorized as 'velocity-based single antenna GPS methods'.

Hrovat [25] and Farrell [26] focused on the accurate positioning capability of a GPS technology. Their methods are categorized as 'position-based multiple-antennae

GPS methods'. In their work, a vehicle was equipped with multiple-antennae GPS receivers. If the position of each GPS antenna within the vehicle is accurately known, the vehicle heading angle can be calculated from the relative position among multiple GPS receivers. Current differential GPS (DGPS) technology can provide accurate position information within the range of centimeters [26]. This level of position accuracy is possible because DGPS eliminates most of the error sources such as ephemeris, ionosphere, troposphere, and multipath errors. Details of DGPS are presented in Section 2.1. For accurate position measurement, DGPS requires a reference station. This, along with its high hardware cost, is a critical disadvantage of DGPS. However, the United States government is currently building a network of permanent GPS base stations to provide a continuously operating reference station (CORS) [27]. As of May 2010, the CORS network contains over 1,450 stations and the network continues to expand. Therefore DGPS technology deserves a second look in the near future.

Ryu [28-29] achieved significant success in sideslip angle estimation by using the carrier-phase differential GPS (CDGPS). CDGPS can directly measure the heading from the observed phase difference of carrier waves received at two antennas. Details of this technology are explained in Section 2.1. In Figure 1.4, the vehicle heading ( $\psi$ ), course ( $\gamma$ ) and sideslip ( $\beta$ ) angles are defined. Once the vehicle heading angle is obtained, the sideslip angle can be obtained from (1.13). The course angle ( $\gamma$ ) is calculated by using the velocity measurement from the GPS receiver.

$$\beta = \gamma - \psi \quad (1.13)$$

The above method is categorized as 'heading-based multiple antennae GPS method'. This method solves most of the previous concerns in the sense that (i) it does not require vehicle parameter information; (ii) it works for large and small sideslip angles; (iii) IMU measurement biases are estimated; (iv) a standing reference tower is not required.; and (v) sideslip can be estimated even when the vehicle is on banked roads. However, the dual-antennae CDGPS receivers is too expensive to be adopted by car makers today [14]. A market survey has revealed that the minimum retail price of this technology is around \$10,000 (USD). Additionally the dual-antennae CDGPS receivers require a clear view to

the satellite in order to maintain a constant lock with at least 4 satellites, while the normal GPS receivers do not need to [30-31] . Accordingly, in adverse conditions such as urban canyons, the signal reliability of CDGPS receivers is worse than the single antenna GPS receiver.

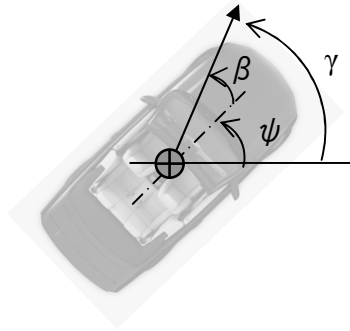


Figure 1.4 The Heading( $\psi$ ), Course( $\gamma$ ), and Sideslip( $\beta$ ) angles

Table 1.1 summarizes the literature review of sideslip angle estimation methods. The dynamic model-based, IMU-based, and velocity-based single-antenna GPS methods are grouped as ‘low-cost’ methods. They all have substantial flaws that prevent them from being adopted by car makers. On the contrary, the high cost of position/heading-based multiple-antennae GPS methods prevents them from being popular, in spite of their superior performance. Therefore, it can be stated that in terms of sideslip angle estimation, no method has been successfully adopted due to either (i) limited performance or (ii) high cost.

Table 1.1 Literature review summary – sideslip angle estimation methods

<b>Dynamic Model-based</b>		Distinction	<ul style="list-style-type: none"> <li>▪ Kinetics of vehicle dynamics</li> </ul>
		Pros.	<ul style="list-style-type: none"> <li>▪ Low-cost</li> </ul>
		Cons.	<ul style="list-style-type: none"> <li>▪ Sensitive to vehicle parameter accuracy</li> <li>▪ Works for small sideslip angle only</li> </ul>
		<b>IMU-based</b>	
		Distinction	<ul style="list-style-type: none"> <li>▪ IMU signal integration</li> <li>▪ Low-cost</li> </ul>
		Pros.	<ul style="list-style-type: none"> <li>▪ No vehicle parameters required</li> <li>▪ Works for large/small slip angles</li> </ul>
		Cons.	<ul style="list-style-type: none"> <li>▪ Vulnerable to unknown sensor bias</li> </ul>
		<b>GPS</b>	
	Velocity-based Single-antenna GPS	Distinction	<ul style="list-style-type: none"> <li>▪ Merge velocity from a single GPS receiver with IMU sensor signals</li> <li>▪ Low-cost</li> </ul>
		Pros.	<ul style="list-style-type: none"> <li>▪ No vehicle parameters required</li> <li>▪ Works for large/small slip angles</li> </ul>
		Cons.	<ul style="list-style-type: none"> <li>▪ Not robust (Sideslip is unobservable only with a single GPS receiver)</li> </ul>
	Position-based Multiple-antennae GPS	Distinction	<ul style="list-style-type: none"> <li>▪ Heading angle is calculated by the precise location information of multiple GPS receivers</li> <li>▪ Accurate and robust sideslip angle</li> </ul>
		Pros.	<ul style="list-style-type: none"> <li>▪ No vehicle parameters required</li> <li>▪ Works for large/small slip angles</li> </ul>
		Cons.	<ul style="list-style-type: none"> <li>▪ A reference tower is required</li> <li>▪ High cost</li> </ul>
	Heading-based Multiple-antennae GPS	Distinction	<ul style="list-style-type: none"> <li>▪ Heading angle is calculated by the carrier wave phase shift measurements between two GPS receivers</li> <li>▪ Same as position-based multiple receivers</li> </ul>
		Pros.	<ul style="list-style-type: none"> <li>▪ No need for a reference tower</li> <li>▪ Works on banked roads</li> </ul>
		Cons.	<ul style="list-style-type: none"> <li>▪ High cost</li> </ul>

### 1.3 Problem Definition

The objective of this research is to establish a low-cost and robust method to estimate the vehicle sideslip angle. Specific requirements are presented below:

- Low-cost requirement: total integration cost must be under \$ 500.
- Robustness requirement #1: the proposed method must work even when the vehicle parameters such as mass, moment of inertia, and tire cornering stiffness are different from nominal values.
- Robustness requirement #2: the proposed method must work with various maneuvers including single lane change, double lane change, slalom, and J-turn on different surface friction levels such as ice pads and asphalt roads.
- Robustness requirement #3: the proposed method must work even when a vehicle runs on banked roads.
- Target accuracy: Root-mean-square (RMS) error of the vehicle sideslip angle estimation must be less than or equal to  $1.5^\circ$  regardless of driving conditions.

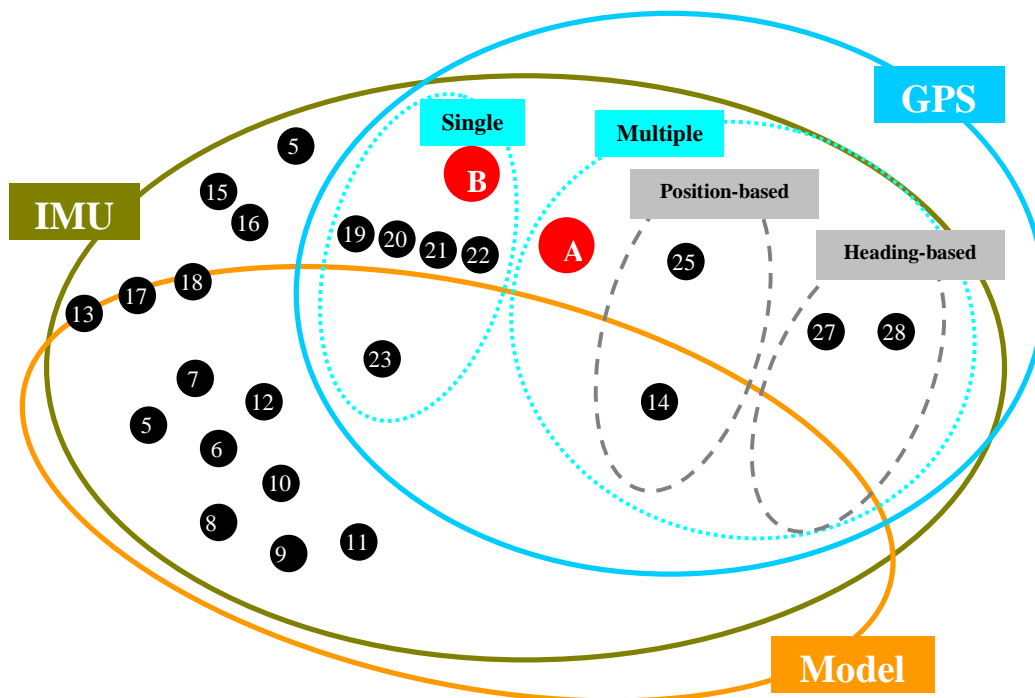


Figure 1.5 Schematic classification of the methods identified in the literature review

All the reviewed papers are grouped based on the employment of dynamic model, IMU, or GPS (Figure 1.5). In the figure, each filled dot represents a sideslip angle estimation paper introduced in Section 1.2. The number inside each dot represents the reference paper number. Dots encircled by multiple ellipses means that they utilize more than one methodology. For example, a filled dot inside the ellipse of ‘Model’ and ‘IMU’ indicates that the paper utilized the bicycle model and IMU measurement. Dots on the edge of ‘Model’ indicate papers using hybrid methods of dynamic model-/IMU-based methods. ‘GPS’ has two sub-categories of ‘Single’ and ‘Multiple’ based on the number of GPS receivers/antennas. ‘Multiple’ is subdivided into ‘Position-based’ and ‘Heading-based’.

The author believes that the GPS technology has high potential to achieve the research goal. Detailed justification is provided in the following chapter. Consequently, areas ‘A’ and ‘B’ in the GPS ellipse are explored during this study. As no vehicle dynamic model is explicitly used, areas ‘A’ and ‘B’ have advantages of (i) being robust against vehicle parameter variations and (ii) the capability to measure the sideslip angle regardless of its magnitude. However, all the current methods in area ‘A’ are cost prohibitive even though they outperform methods of other categories. For this reason, the author will pursue drastic cost reduction in ‘A’ while preserving the same level of performance. Methods in area ‘B’ do not have cost concerns but they have performance limitations; therefore, the author will do an in-depth investigation to remove performance limitations of selected methods in area ‘B’ without a significant cost increase. Bank angle estimation will also be sought as a means to improve sideslip estimation performance when a vehicle runs on a banked road. By enriching those two areas, this study aims to provide affordable sideslip estimating technology with the improved performance.

## 1.4 Thesis Contributions

The original contributions of this thesis include:

- Establishment and experimental verification of the method using velocities of two GPS receivers toward vehicle sideslip estimation. IMU measurements are combined with them through a Kalman filter. The observability analysis revealed that sideslip angles are observable only when a vehicle turns. Delays of GPS signals and unsynchronized updates of two GPS receivers were identified as challenging problems during integration and proper solutions were proposed and experimentally verified. As a result, the vehicle sideslip angle can be estimated at much cheaper cost (~\$ 500) than the current dual antennae GPS method (> \$10,000).
- Integration of a magnetometer with GPS and IMU to estimate the vehicle sideslip angle. A cascade Kalman filter was developed to combine all the sensor signals. Significant disturbances in the magnetometer signals were identified as the main challenge. A stochastic filter was designed to reject the disturbance and integrated on the Kalman filter framework. Extensive experiments on a track and in a neighborhood area verified the proposed method. As a result, the vehicle sideslip angle can be estimated regardless of surface friction levels and road bank angles with low cost (< \$500).

## 1.5 Thesis Organization

The rest of this thesis is organized as follows. CHAPTER 2 describes current GPS technology in general and explains rapidly changing circumstances of GPS. This chapter will emphasize three unique features of GPS velocity measurement which are important to achieve the research goal. CHAPTER 3 provides mathematical backgrounds for sensor fusion through the Kalman filter. Stochastic observability will be discussed. This chapter also explains techniques to handle two technical difficulties during sensor fusion; (i) delayed measurements and (ii) unsynchronized measurement updates. CHAPTER 4

shows how velocities of two GPS receivers are kinematically coupled. To extract the vehicle sideslip angle, a Kalman filter will be introduced as a framework combining GPS velocity measurements with IMU signals. The stochastic observability is discussed along with technical challenges and their solutions. Experimental results will be provided for the verification. In CHAPTER 5, measurements of a magnetometer are merged with GPS and IMU signals to estimate vehicle sideslip angles. Principles of a disturbance rejecting stochastic filter and its integration on the Kalman filter framework will be described. Implementation of a cascade Kalman filters will be shown and challenge/solution during integration will be discussed. Results of comprehensive simulations and in-vehicle experiments will be provided to verify the method. CHAPTER 6 will present concluding remarks and future works.



## CHAPTER 2

# GLOBAL POSITIONING SYSTEM (GPS)

### 2.1 Introduction

GPS is a space-based global navigation satellite system (GNSS). GPS was originally developed and implemented by the U.S. Department of Defense for a military navigation purpose. In the 1980s, it was opened to the public by removing the Selective Availability (SA). Since then, it provides accurate, continuous, world-wide, three-dimensional information of position and velocity. The satellite constellation consists of 24 satellites arranged in 6 orbital planes with 4 satellites per plane (Figure 2.1). The satellites broadcast ranging codes and navigation data on two frequencies, L1 (1,575.42 Hz) and L2 (1,227.6 Hz) [32]. GPS is the United State's version of GNSS. In our work, however, the term GPS is used interchangeably with GNSS because GPS is currently the biggest part of GNSS.



Figure 2.1 GPS Constellation <http://quest.arc.nasa.gov/>

The positioning capability of GPS gave rise to the commercial navigation system, which has become a fairly popular technology. A GPS receiver calculates its location as follows: (i) measuring the travel time of a signal by comparing the signal transmitted/received time, (ii) calculating the line-of-sight distance from the GPS satellites by multiplying the speed of light with the travel time, (iii) drawing a sphere around the satellite whose radius is the pseudorange (line-of-sight distance between the satellite and the receiver), and (iv) repeating (i)~(iii) for more than four satellites and identifying the overlapped area. Without any special apparatus, the position accuracy is around 10m [33]. The error sources are summarized in Table 2.1 [34].

Table 2.1 GPS positioning error sources

Error Source	Typical Error (meters, $1\sigma$ )	Brief Explanation
Ionosphere	7.0	Travel speed variation in ionosphere
Troposphere	0.7	Travel speed variation in troposphere
Ephemeris & Clock	3.6	Uncertainties in satellite position and time
Receiver Noise	1.5	General receiver noise
Multipath	1.2	Wave refraction by a wall
Total User Equivalent Range Error (UERE)	8.1	Square root of the sum of the squares of each terms above

Differential GPS (DGPS) is a technique that significantly improves the position accuracy. The DGPS requires high-quality GPS “reference receivers” at accurately known locations. There are two types of DGPS: code-phase DGPS and carrier-phase DGPS. By convention, code-phase DGPS is referred to as DGPS. Figure 2.2 schematically shows how code-phase DGPS (henceforth referred to as DGPS) reduces these errors. Only one satellite is displayed for succinctness. A moving vehicle and the standing tower share the same satellite signal (black arrows). The position errors of the standing tower and a moving vehicle are the same when the vehicle runs in the vicinity of the tower. If the location of the standing tower is exactly known, the position error due to GPS signal corruption can be accurately calculated. This calculated error is broadcasted

(red arrow) and the moving vehicle corrects its position by using this broadcasted error. DGPS enables positioning accuracy of about a meter.

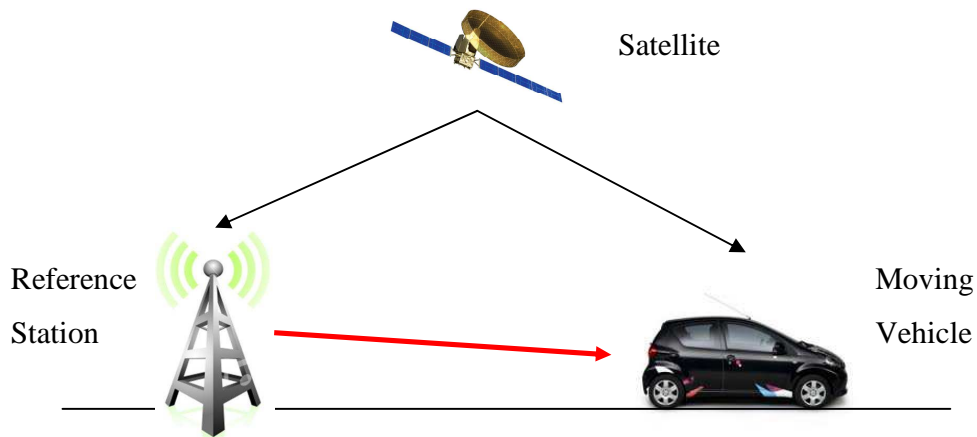


Figure 2.2 Principle of Differential GPS(DGPS)

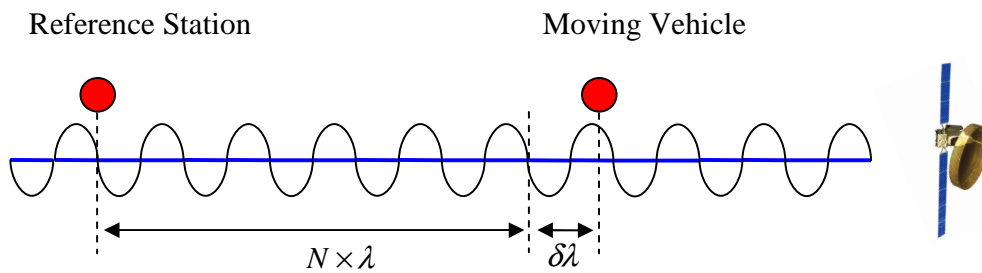


Figure 2.3 Principle of Carrier-Phase Differential GPS (CDGPS)

The carrier-phase differential GPS (CDGPS) provides the highest level of positioning accuracy. Figure 2.3 displays the simplified schematics of the reference tower and a vehicle to explain the operation of CDGPS. The distance between the reference station and a moving vehicle is  $N \times \lambda + \delta\lambda$ , where  $N$  is maximum integer number containing complete wavelengths in the distance and  $\delta\lambda$  is the remaining phase difference.  $\delta\lambda$  is directly measured by CDGPS receivers. Determining  $N$  is a challenging problem and frequently referred to as *carrier-cycle integer ambiguity*. There are several

algorithms to solve this problem [32]. Resolving *carrier-cycle integer ambiguity* requires at least 4 satellites to be constantly locked. If the number of locked satellites momentarily drops below 4, the “cycle slip” occurs and the integer ambiguity must be recalculated. If the “cycle slip” repeatedly occur then the correct ambiguities may not be resolved [30-31]. Therefore CDGPS requires the clearer sky than the GPS.

Once the integer N is determined, the distance between the reference station and a moving vehicle is obtained. If more than four satellites are involved, position of the moving vehicle with respect to the reference station is calculated. If the location of the reference station is exactly known, the position of the moving vehicle can be accurately known [32]. The position error by CDGPS can thus be reduced to a few centimeters.

One significant advantage of CDGPS over DGPS is that it can determine the vehicle heading angle without the aid of a reference station. Figure 2.4 shows the simplified schematic diagram of a two-antennae CDGPS receiver for heading angle determination. Upon measurement of the carrier-phase shift ( $\delta\lambda$ ), the distance (D) is calculated after resolving the *carrier-cycle integer ambiguity* problem. Then the heading angle can be calculated using the distance between the two CDGPS antennas (L). This method offers tremendous advantages because errors caused by (i) satellite signal phase, (ii) ephemerides, (iii) ionosphere, and (iv) troposphere are cancelled. Multipath is the only major error source. The heading angle error is less than  $0.1^\circ$  for baseline of 10 m [35]. A reference station is not required for heading angle calculation because it is based on the relative position vector.

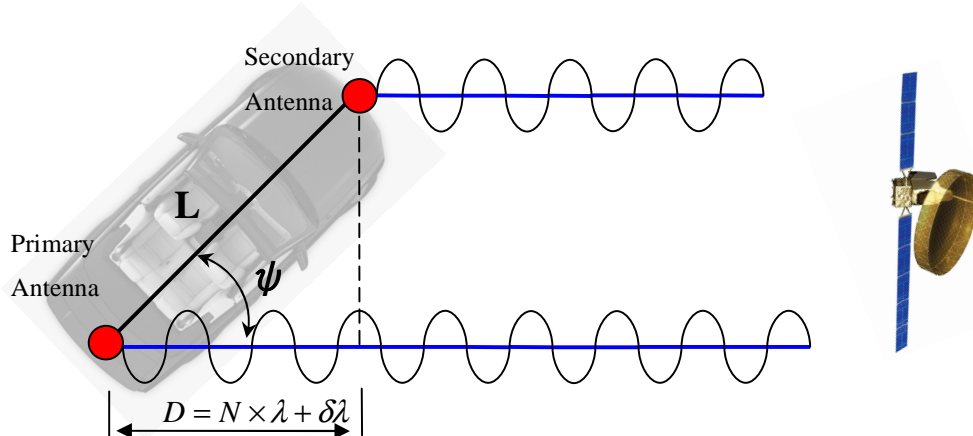


Figure 2.4 CDGPS: heading angle measurement

## 2.2 GPS: Potentials and Changing Circumstances

To achieve the research goal, the author will explore GPS-based methods instead of dynamic model-based or IMU-based methods. Historically utilization of GPS for active safety systems has attracted criticism due to signal reliability and cost concerns. This section will describe why the author choose GPS-based methodology by explaining potential of GPS and rapidly changing circumstances around GPS technology.

First, the method using GPS technology has outperformed other methods in terms of sideslip angle estimation. As seen in the literature review, the method employing a dual-antennae CDGPS could provide accurate vehicle sideslip angle estimation without requesting vehicle parameter information. That method is also valid for a wide range of sideslip angles including the saturated area of  $f_y$  -slip curve [23, 28-29]. This is a significant advantage over the dynamic model-based methods. Additionally, it outperforms the IMU-based method because accumulated errors due to the integration are periodically corrected by virtue of GPS signals.

Second, the reliability and accuracy of global navigation satellite system (GNSS) including GPS will be drastically improved. Historically, the reliability of GPS signal was of concern such that car makers hesitated to use it for active safety systems. However, the launch of the GALILEO will dramatically improve the reliability of GNSS. GALILEO is the name of the European global navigational satellite system. Its development began in the early 1990s and the target completion year is 2013. GALILEO will have 30 Medium Earth Orbiting (MEO, 23000 km orbital radius) satellites in 3 equally spaced orbital planes with an inclination of 54 degrees. The GALILEO system will transmit a variety of signals in support of open, commercial, safety of life, and public regulated services. Under an agreement with the U.S., the open GALILEO signal operates at the same frequency as the GPS L1. This will facilitate the design and manufacturing of user equipment to process signals from GPS and GALILEO. Several researchers have investigated the impact of GALILEO and have clearly observed that the combination of GPS/GALILEO improves the signal reliability and accuracy [36-40].

Figure 2.5 shows a result of O’Keefe’s work [38]. Three cases of global maximum horizontal position errors (HPE) distributions – GPS only, GALILEO only, and GPS+GALILEO – are presented. O’Keefe used HPE as a measure of reliability and accuracy. A blue color (small HPE number) means more reliable signal coverage than a red color (large HPE number). As can be seen, the (GALILEO+GPS) combination enables global blue coverage, which means reliability and accuracy improvement. In addition to the GALILEO, the advancement of BeiDou (Chinese GPS, in progress), modernization of GLONASS (Russian GPS), and modernization of GPS (United States) are expected to boost the signal reliability and accuracy further.

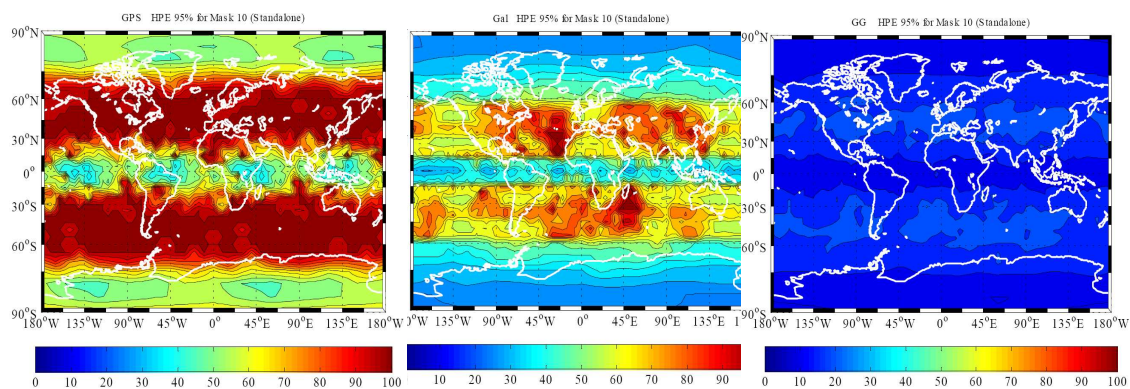


Figure 2.5 Maximum horizontal position errors (HPE) in meters  
(Left) GPS only, (Middle) GALILEO only, (Right) GPS+GALILEO

Third, the price of GPS applications has shown a continuous trend of dropping. A Consumer Behavior Report [41] showed the declining trend of GPS product prices. In the current market, an integrated GPS development kit is sold, in retail, for around \$200 and the price of the core chip module is around \$100. The cost is not a hindrance for GPS to be widely used in the automotive application any more. In fact, GPS-based navigation systems are available in almost all passenger cars as an option.

## 2.3 GPS: Velocity Measurements

The velocity measurement is standard information provided by a GPS receiver. It has several unique features adopted by my research. These features are discussed below.

GPS velocity information is accurate regardless of its positioning accuracy because velocity is calculated by using the Doppler shifts of GPS carrier waves instead of differentiating position information [33]. The Doppler Effect refers to the phenomenon that a receiver experiences a different frequency than what a transmitter generates when a receiver has a relative velocity with respect to a transmitter. The frequency difference is called the Doppler shift. There are various ways to convert the Doppler shift into the velocity of a receiver. The typical accuracy is 3 cm/s ( $1\sigma$ ) for horizontal velocity and 6 cm/s ( $1\sigma$ ) for vertical velocity [33].

GPS velocity measurements contain unbiased white noise only [20]. This is a significant benefit in terms of sensor error modeling because no bias estimation is required.

Figure 2.6 is the Allan Variance plot of the velocity measurement error of the GPS receiver which is used for this study (U-blox LEA 5). Velocity measurements were collected while the receiver was stationary for 1.5 hours. This plot shows apparent linearity with a slope of  $-1/2$ . This is a typical trait suggesting that only white noise exists in the measurement error [1]. Details of this analysis are presented in Appendix A.

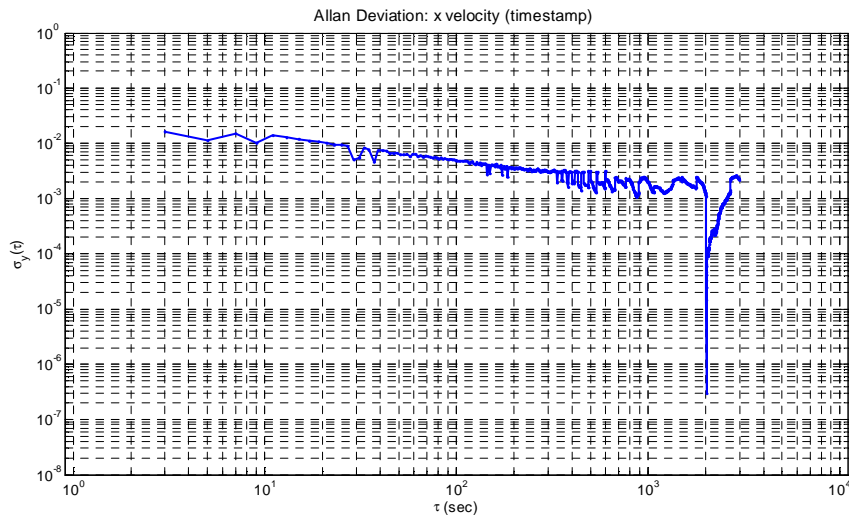


Figure 2.6 The Allan Variance plot of the GPS velocity error (U-blox LEA 5)

Velocity measuring performance of GPS stays almost constant through products ranging widely in price. Figure 2.7 shows the GPS performance specifications as functions of price. Several GPS receiver makers (including Novatel, San Jose Tech, Nav Sync, U-blox, Dewetron, and VBOX) were contacted for price and performance specifications. For fair comparison, the integrated development kits of each manufacturer were compared. As can be seen in Figure 2.7, the velocity measuring performance specification has little correlation with the price, whereas the update rate shows strong correlation. This means that (i) a low-cost GPS receiver can provide a velocity accuracy level similar to the high-cost GPS receivers, and (ii) a low-cost GPS receiver will have low update rate. The relationship between position accuracy and price looks somewhat random in Figure 2.7. It is clear that even the accuracy of the best performing unit (1.5 m,  $1\sigma$ ) is not precise enough to be employed for this research. This is why GPS position measurements are not used in this study.



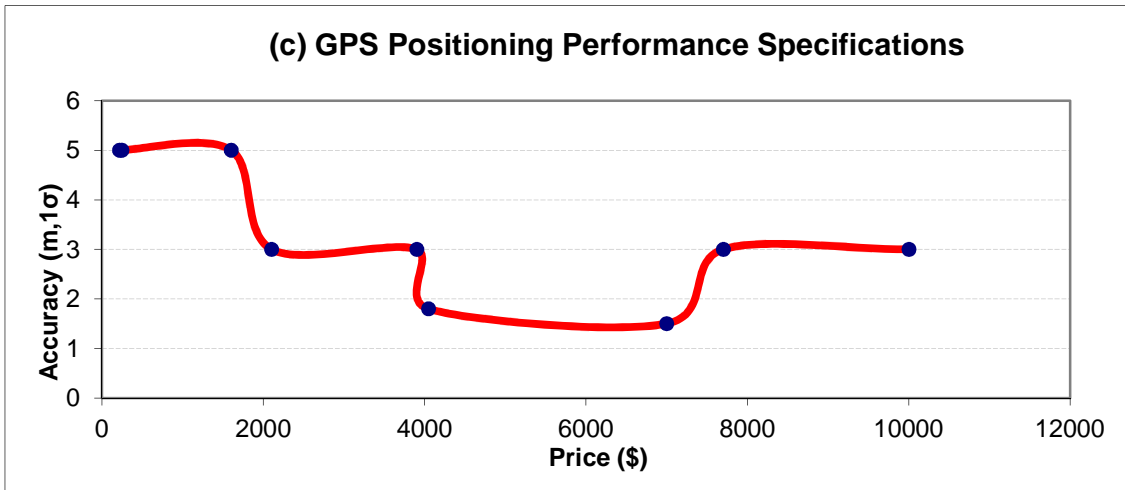
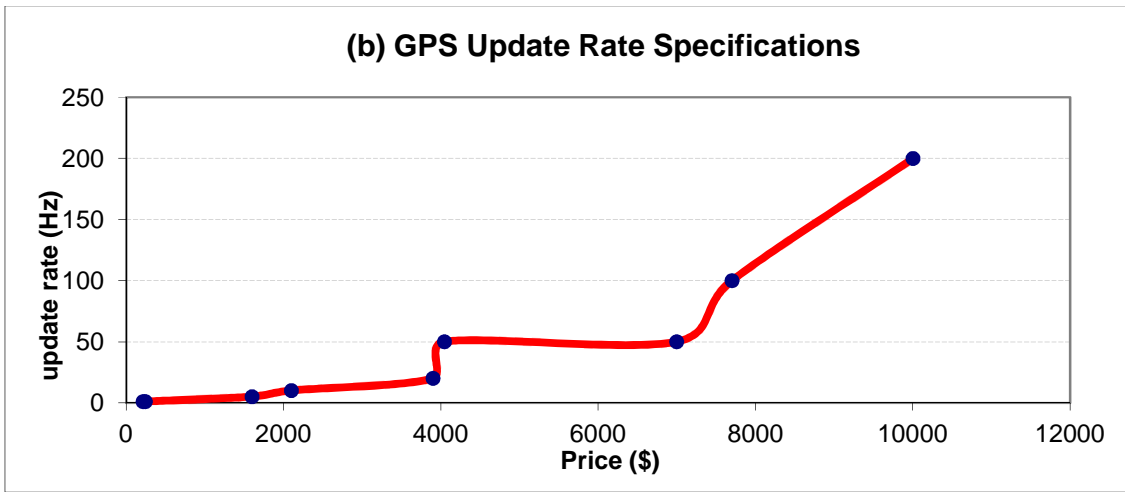
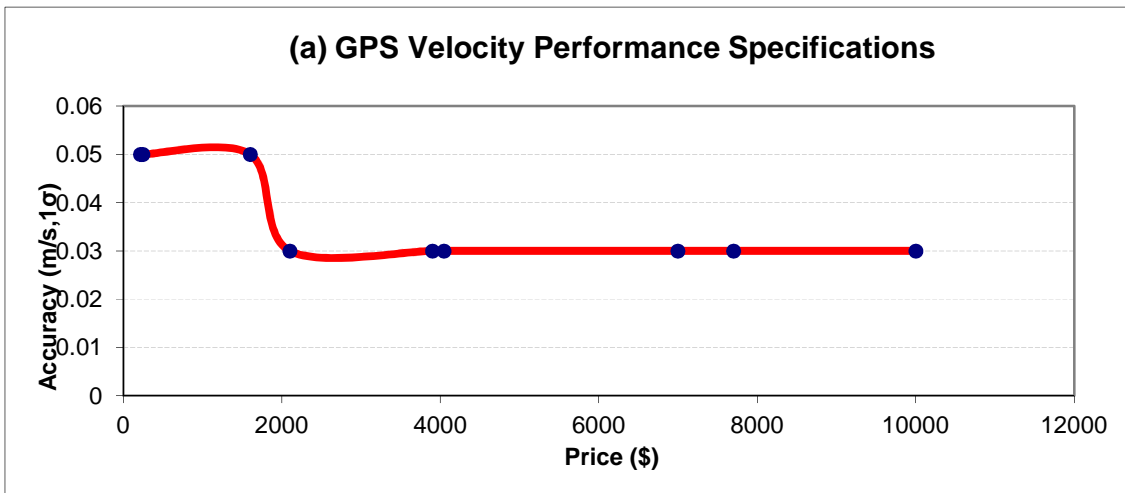


Figure 2.7 GPS performance vs. price; (a) velocity, (b) update rate, (c) position

## 2.4 Summary

GPS is a space-based global navigation satellite system and it has gained popularity as a ground-vehicle navigational system due to its positioning capability. GPS technology has a significant potential to enhance vehicle active safety. Methods using dual antennas CDGPS have shown by far the best accuracy in sideslip angle estimations. Historically, the low reliability and high cost have hindered GPS technology from being popular in vehicle active safety systems. However, the GALILEO system (European GPS, plan to be completed by 2013) will enhance GPS signal reliability drastically. In addition, the development of BeiDou (Chinese GPS, in progress) and modernization of GLONASS (Russian GPS) would make the future GPS signal reliability even more promising. The price of GPS hardware has dropped continuously, and now it is in a feasible range to be adopted by car makers. The GPS velocity measurement has three distinctive features: (i) it can be accurate regardless of positioning accuracy, (ii) it can be accurate even for low-cost systems, and (iii) it contains only unbiased white noise in its velocity measurement.

## CHAPTER 3

### SENSOR FUSION THROUGH KALMAN FILTER

#### 3.1 Kalman Filter

The Kalman filter is a very successful mathematic tool in engineering applications. Since R.E. Kalman invented it in the early 1960's, it has been adapted in various applications such as manufacturing processes, aircrafts, ships and spacecrafts. It provides a means for inferring the missing state information from noisy measurements. It is a recursive filter to yield optimal estimates by taking into account statistics of system dynamics and measurement noises.

Let two random variables  $x$  and  $z$  be related via a joint PDF  $f_{X,Z}(x, z)$ . For any given measurement ( $z$ ), the optimal estimation of  $x$  minimizing  $\varepsilon[(x - \hat{x})^2]$  is

$$\hat{x} = \varepsilon(x | z) = \int x \frac{f_{X,Z}(x, z)}{f_Z(z)} dx \quad (3.1)$$

where  $\varepsilon(\cdot)$  is an expected value

This is known as the minimum mean square error (MMSE) estimation.

If the two random variables  $x$  and  $z$  are related via the bivariate normal distribution, the joint probability density function (PDF) and the MMSE estimation are given by (3.2) and (3.3), respectively.

$$f_{XZ}(x, z) = C \exp \left[ \left( \frac{x - \mu_x}{\sigma_x} \right)^2 - 2\rho \left( \frac{x - \mu_x}{\sigma_x} \right) \left( \frac{z - \mu_z}{\sigma_z} \right) + \left( \frac{z - \mu_z}{\sigma_z} \right)^2 \right] \quad (3.2)$$

$$\hat{x} = \mu_x + \rho \frac{\sigma_x}{\sigma_z} (z - \mu_z) \quad (3.3)$$

$$\text{where } C = \frac{1}{2\pi\sigma_x\sigma_z\sqrt{1-\rho^2}}$$

$\sigma_x, \sigma_z$  standard deviation of x and z

$\mu_x, \mu_z$  mean of x and z

$$\rho = \frac{\sigma_{xz}}{\sigma_x\sigma_z} \quad \text{correlation coefficient}$$

Optimal state estimation has a linear relationship with a measurement if the state and measurement have a bivariate normal distribution. Figure 3.1 is a top view of a bivariate normal distribution. The dashed line represents the optimal estimation path.

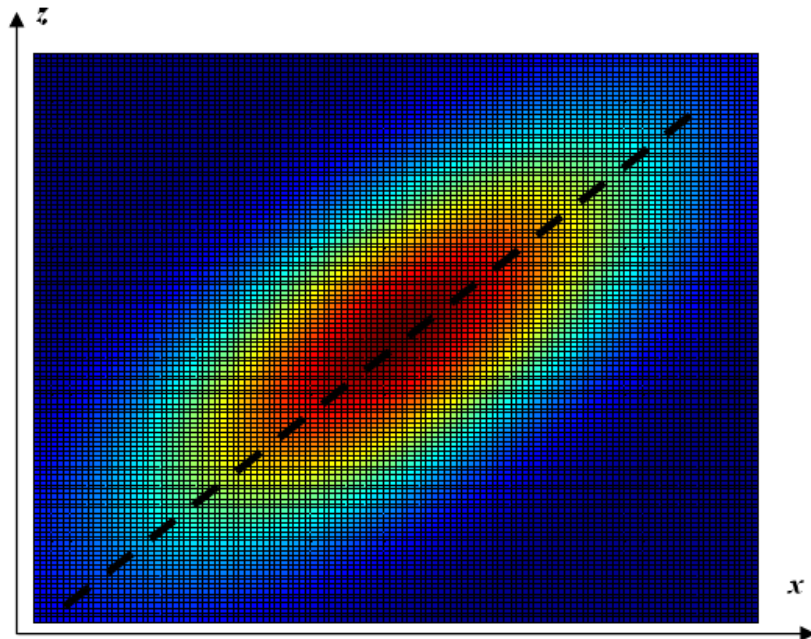


Figure 3.1 Top view of the bivariate normal distribution

The same concept is expanded to vector cases. Equations (3.4) and (3.5) are standard discrete system equations.

$$x_k = \Phi_{k,k-1}x_{k-1} + \Gamma_{k-1}u_{k-1} + \Lambda_{k-1}w_{k-1} \quad (3.4)$$

$$z_k = H_k x_k + v_k \quad (3.5)$$

Where state  $x_k \in R^{n \times 1}$ , input  $u_{k-1} \in R^{l_u \times 1}$ , plant noise  $w_{k-1} \in R^{l_w \times 1}$ , measurement  $z_k \in R^{m \times 1}$ , measurement noise  $v_k \in R^{m \times 1}$ , system transition matrix  $\Phi_{k,k-1} \in R^{n \times n}$ ,  $\Gamma_{k-1} \in R^{n \times l_u}$ ,  $\Lambda_{k-1} \in R^{n \times l_w}$ , and  $H_k \in R^{m \times n}$ .

If all the components of  $w_{k-1}$  and  $v_k$  are described by normal distributions (a multivariable normal distribution in this case), the optimal state estimation and its corresponding covariance are obtained through [42]:

$$\text{State estimate extrapolation} \quad \hat{x}_k^- = \Phi_{k,k-1}\hat{x}_{k-1}^+ + \Gamma_{k-1}u_{k-1} \quad (3.6)$$

$$\text{Covariance estimate extrapolation} \quad P_k^- = \Phi_{k,k-1}P_{k-1}^+\Phi_{k,k-1}^T + \Lambda_{k-1}Q_{k-1}\Lambda_{k-1}^T \quad (3.7)$$

$$\text{Kalman gain computation} \quad K_k = P_k^-H_k^T [H_kP_k^-H_k^T + R_k]^{-1} \quad (3.8)$$

$$\text{State estimate correction} \quad \hat{x}_k^+ = \hat{x}_k^- + K_k [z_k - H_k\hat{x}_k^-] \quad (3.9)$$

$$\text{Covariance estimate update} \quad P_k^+ = [I - K_kH_k]P_k^- \quad (3.10)$$

where

$\hat{x}_k^-$ : state estimate extrapolated from step k-1 using system dynamics

$\hat{x}_k^+$ : state estimate after measurement correction at step k

$u_k, w_k$ : input and plant noise

$z_k$ : measurement

$v_k$ : measurement noise

$P_k^- = \mathcal{E}\{(x_k - \hat{x}_k^-)(x_k - \hat{x}_k^-)^T\}$ : state covariance estimate from system dynamics

$P_k^+ = \mathcal{E}\{(x_k - \hat{x}_k^+)(x_k - \hat{x}_k^+)^T\}$ : updated covariance estimate by measurement

$Q_k = \mathcal{E}\{w_k w_k^T\}$ : plant noise covariance matrix

$R_k = \mathcal{E}\{v_k v_k^T\}$ : measurement noise covariance matrix

Equations (3.6) and (3.7) are referred as ‘time update’ while (3.9) and (3.10) are referred as ‘measurement update’. Equation (3.6) is frequently called as ‘plant’. The term  $(z_k - H_k \hat{x}_k^-)$  in (3.9) is called as ‘innovation’ and  $(H_k P_k^- H_k^T + R_k)$  in (3.8) is the covariance matrix of the innovation.

Sometimes system equations of (3.4) and (3.5) are nonlinear in which case the state equations will have the following form

$$x_k = f(x_{k-1}, u_{k-1}) + \Lambda_{k-1} w_{k-1} \quad (3.11)$$

$$z_k = g(x_k) + v_k \quad (3.12)$$

where  $f \in R^{n \times 1}$  and  $g \in R^{m \times 1}$

In this case, the Jacobian of (3.11) and (3.12) replace  $\Phi_{k,k-1}$  and  $H_k$  of the Kalman filter process where

$$\Phi_{k,k-1} = \left[ \begin{array}{cccc} \frac{\partial f_1}{\partial x_1} & \frac{\partial f_1}{\partial x_2} & \dots & \frac{\partial f_1}{\partial x_n} \\ \frac{\partial f_2}{\partial x_1} & \frac{\partial f_2}{\partial x_2} & \dots & \frac{\partial f_2}{\partial x_n} \\ \vdots & \vdots & \ddots & \vdots \\ \frac{\partial f_n}{\partial x_1} & \frac{\partial f_n}{\partial x_2} & \dots & \frac{\partial f_n}{\partial x_n} \end{array} \right] @ \hat{x}_{k-1}^+, u_{k-1} \quad (3.13)$$

$$H_k = \begin{bmatrix} \frac{\partial g_1}{\partial x_1} & \frac{\partial g_1}{\partial x_2} & \dots & \frac{\partial g_1}{\partial x_n} \\ \frac{\partial g_2}{\partial x_1} & \frac{\partial g_2}{\partial x_2} & \dots & \frac{\partial g_2}{\partial x_n} \\ \vdots & \vdots & \ddots & \vdots \\ \frac{\partial g_m}{\partial x_1} & \frac{\partial g_m}{\partial x_2} & \dots & \frac{\partial g_m}{\partial x_n} \end{bmatrix} @ \hat{x}_k^- \quad (3.14)$$

Additionally (3.6) and (3.9) are changed to

$$\hat{x}_k^- = f(\hat{x}_{k-1}^+, u_{k-1}) \quad (3.15)$$

$$\hat{x}_k^+ = \hat{x}_k^- + K_k [z_k - g(\hat{x}_k^-)] \quad (3.16)$$

This whole process is known as the Extended Kalman Filter (EKF). Unlike its linear counterpart, the EKF in general is not an optimal estimator. However it provides a working solution with manageable computational expense.

### 3.2 Stochastic Observability

Given a Kalman filter, there is one critical question: how do we know if the state can be fully determined from measurements? This observability problem has drawn several researchers' attention [43-48]. For linear time invariant (LTI) systems, the necessary and sufficient condition for the observability has a clear form [42]. However, the necessary and sufficient condition for time-varying or nonlinear systems is not fully developed. A set of sufficient conditions were developed by Dyest, Price and Sorenson. They are summarized in Jazwinski's book [49]. This section presents several principles of the book to provide mathematic backgrounds for stochastic observability analysis of the Kalman filter utilized in this study. The term 'stochastic observability' is used here to be distinguished from the standard definition of the observability of the Luenberger observer.

Recall that (3.4) and (3.5) represent a linear time-varying (LTV) system. One way to define the stochastic observability was suggested by Bageshwar[43]: the system represented by (3.4) and (3.5) is stochastically observable if there exists a positive integer  $N$  and positive constant  $\gamma$  such that

$$\sigma_{\max}(P_k^+) < \gamma \quad k \geq N \quad (3.17)$$

where  $\sigma_{\max}(\cdot)$  is the largest singular value of the matrix. This definition is valid in the sense that  $P_k^+$  representing state estimation errors after measurement updates is upper limited. However, Jazwinski went further to provide complete (but tighter) conditions for the observability as follows.

The system is uniformly completely observable if there exist a positive integer  $N_o$  and positive constants  $\alpha_o, \beta_o$  such that

$$\begin{aligned} 0 < \alpha_o I \leq O(k, k - N_o) \leq \beta_o I \quad \forall k \geq N_o \\ \text{where} \\ O(k, k - N_o) \equiv \sum_{i=k-N_o}^k \Phi_{i,k}^T H_i^T R_i^{-1} H_i \Phi_{i,k} \end{aligned} \quad (3.18)$$

The system is uniformly completely controllable if there exist a positive integer  $N_c$  and positive constants  $\alpha_c, \beta_c$  such that

$$\begin{aligned} 0 < \alpha_c I \leq C(k, k - N_c) \leq \beta_c I \quad \forall k \geq N_c \\ \text{where} \\ C(k, k - N_c) \equiv \sum_{i=k-N_c}^{k-1} \Phi_{k,i+1} \Gamma_i Q_i \Gamma_i^T \Phi_{k,i+1}^T \end{aligned} \quad (3.19)$$

If the system (represented by (3.4) and (3.5)) is uniformly completely observable, uniformly completely controllable and  $P_0$  is positive definite, then  $P_k^+$  is uniformly bounded from above and below as seen



$$0 < \left[ O(k, k-N) + C^{-1}(k, k-N) \right]^{-1} \leq P_k^+ \leq O^{-1}(k, k-N) + C(k, k-N) \quad (3.20)$$

$$\forall k \geq N \equiv \max(N_o, N_c)$$

The proof of (3.20) assumes that  $P_k^+$  decreases as  $k$  increases. To verify that assumption, the Lyapunov theory is employed. State estimation error (after measurement update) has a recursive form of (3.21) and (3.22) is the Lyapunov function [49].

$$e_k = [I - K_k H_k] \Phi_{k,k-1} e_{k-1} + K_k v_k$$

where

$$e_k = x_k - \hat{x}_k^+$$

$$v_k = y_k - H_k \hat{x}_k^+ \quad (3.21)$$

$$V(e_k, k) = e_k^T (P_k^+)^{-1} e_k \quad (3.22)$$

If the system is uniformly completely observable, uniformly completely controllable and  $P_0$  is positive definite, the homogeneous part of (3.21) is proven to be uniformly asymptotically stable by using (3.22) and upper/lower bounds of (3.20). If (3.21) is uniformly asymptotically stable, bounded measurement errors ( $v_k$ ) produce bounded state error ( $e_k$ ). Therefore, (3.23) is a sufficient condition of stochastic observability because  $P_k^+$  is upper-bounded and state estimation error is BIBO stable.

- The system is uniformly completely observable
  - The system is uniformly completely controllable
  - $P_0$  is positive definite
- $$(3.23)$$

### 3.3 Sensor Fusion through Kalman Filter

When several sensors measure the same state, one question arises: what is the optimal state estimate from those measurements? The process toward finding the optimal state estimate is called ‘sensor fusion’ and the Kalman filter has been a popular technique for it [8, 20, 22-23, 28-29, 50]. If measurements of a sensor are expressed by differential equations of the state, those differential equations will provide the plant equation of (3.4). Other sensors must provide measurement equations of (3.5). Once the Kalman filter equations are set, the optimal state estimate is calculated according to noise levels of the plant and measurements. In this study, the author has encountered two technical difficulties: (1) significantly delayed measurement and (2) unsynchronized measurement updates.

#### 3.3.1 Measurement Delay Handling

Certain measurements may have significant delays. The delay must be properly addressed during the sensor fusion to achieve the highest performance. Several methods have been proposed which can be grouped into two categories; hardware-based and software-based methods. The hardware-based methodology needs measurement update timing information in a reference clock such as one Pulse-Per-Second signal (PPS) of a GPS. As update timings are accurately known, measurement of several sensors can be aligned [51-55]. Even though this methodology can facilitate tight coupling among sensors, it requires direct access to the sensor module hardware. If direct access to the hardware is not allowed, software-based methods may be considered. Skog proposed a software-based method using the Taylor’s expansion [56-57]. It applies the Taylor’s expansion to express a measurement in a linear form of time delay and augments the state vector with the unknown delay. Equation (3.24) shows an example with GPS velocity measurement.

$$V_{(t)}^{GPS} = V_{(t-T)}^{real} = V_{(t)}^{real} - \frac{dV_{(t)}^{real}}{dt}T + H.O.T \quad (3.24)$$

If  $\frac{dV_{(t)}^{real}}{dt}$  is known and the higher order terms (H.O.T) are negligible, Skog's method is applicable. However, the higher order terms of (3.24) are not negligible for high dynamic maneuvers such as a double lane change or slalom on high frictional surfaces. Instead, the idea of Larsen [58] is adopted in this dissertation. Figure 3.2 is a discrete Kalman filter framework. From time stamps of  $s$  to  $k-1$ , state and its covariance evolve through the time update because no measurement is updated (black solid line). At the time stamp of  $k$ , a measurement is available ( $z_k$ ) but it represents a value of time  $s$ . Accordingly  $z_k$  is shifted back to the time  $s$  and merged with state estimation of  $\hat{x}_s$  to yield the measurement updated state of  $\hat{x}_s^{new}$  (red solid line). Then the new state at  $k$  ( $\hat{x}_k^{new}$ ) is obtained through time update from  $\hat{x}_s^{new}$  (red dashed line). Unlike the hardware method, this is a proactive method that extrapolates states from  $s$  to  $k$  through a time update.

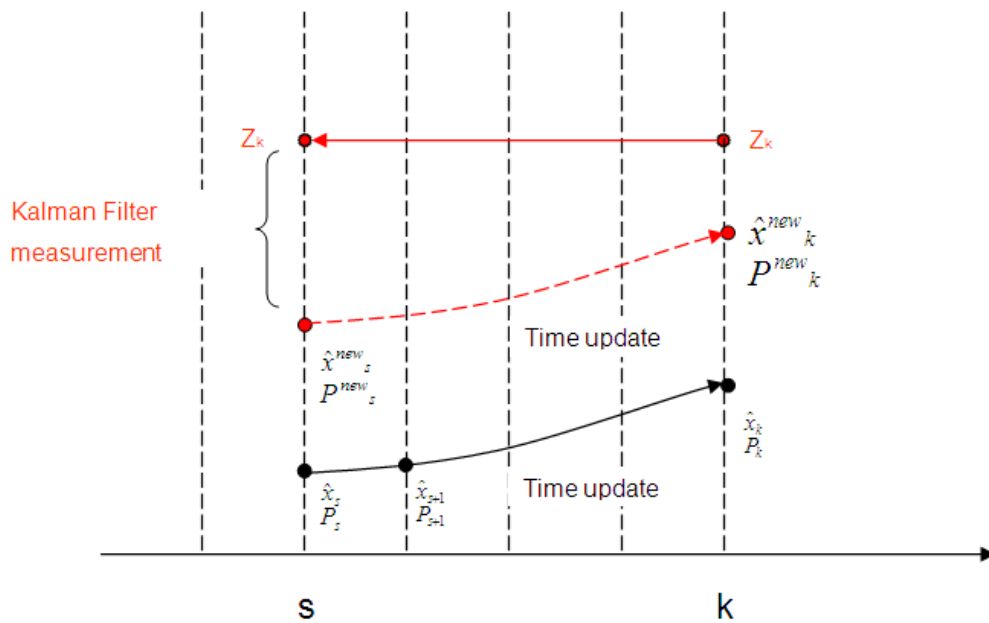


Figure 3.2 Discrete Kalman filter framework for delay handling

### 3.3.2 Unsynchronized Measurement Updates Handling

Let two sensors be used for measurement and assume the two measurement equations are

$$\begin{aligned} z_{1,k} &= g_1(x_{1,k}, \dots, x_{n,k}) + v_{1,k} \\ z_{2,k} &= g_2(x_{1,k}, \dots, x_{n,k}) + v_{2,k} \end{aligned} \quad (3.25)$$

Assume that the state  $(x_{1,k} \dots x_{n,k})$  is completely determined only when both of  $z_{1,k}$  and  $z_{2,k}$  are available. Then one question arises: what if the two measurements are updated at different timing as seen in Figure 3.3?

Originally the author used a measurement extrapolation. When  $z_2$  is updated at  $t_2$ ,  $z_1$  of  $t_1$  is extrapolated by a quadratic function to provide a pseudo-measurement at  $t_2$  (black dashed arrow). Three latest data points are used to build the quadratic function. Accordingly both values from  $z_1$  and  $z_2$  are employed for the measurement update. However, when a vehicle movement is highly dynamic such as in a slalom test on an asphalt road, the measurement extrapolation is not accurate enough. Consequently, the state estimation performance is degraded.

‘Asynchronous update’ is an effective technique to solve this problem[59]. The idea is simple. The Kalman filter measurement update is executed only for the updated sensor, even though the updated sensor contains only partial information. Accordingly at  $t_1$ , only  $z_1$  is used for measurement update and only  $z_2$  is employed at  $t_2$ . Legitimately, concerns about the observability arise with this method. Results of the observability analysis are presented in the next chapter.

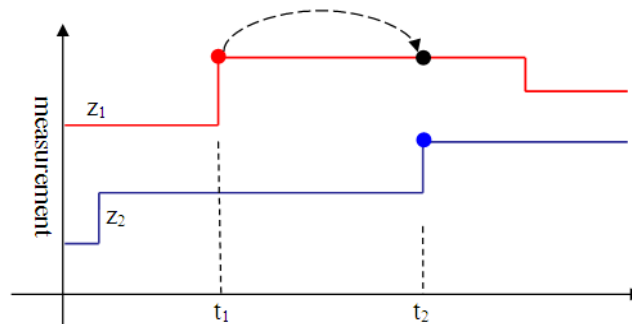


Figure 3.3 Schematic diagram of unsynchronized updates from two sensors.

### 3.4 Summary

This chapter provides the mathematic backgrounds employed in this study. The Kalman filter is the mathematic tool to calculate the optimal state estimation from noisy measurements. For linear systems, the optimality of the estimated state is proven if all the noises have the normal distributions. The Extended Kalman Filter (EKF) is a modified version of the Kalman filter to cover nonlinear systems, but optimality of the EKF is not guaranteed.

For stochastic filters including the Kalman filter, optimality does not imply stability. In other words, estimation errors from the Kalman filter may diverge. For linear systems, sufficient conditions which guarantee the estimation stability were discovered while the sufficient and necessary was identified for linear time invariant (LTI) systems. Since the sufficient conditions of linear systems limit state error covariance matrix from above, the author calls it as the stochastic observability.

If a state is measured by more than one sensor, the optimal estimation of the state can be obtained by the sensor fusion technique. The Kalman filter is a popular tool for the sensor fusion. Two technical challenges arise during sensor fusion through the Kalman filter. One is “delayed measurement” and the other is “unsynchronized measurements”. The delayed measurement is addressed by measurement shifting in the Kalman filter framework and the unsynchronized update issue is resolved by the asynchronous update technique.

## CHAPTER 4

# **SIDESLIP ANGLE ESTIMATION USING VELOCITY MEASUREMENTS FROM TWO GPS ANTENNAE**

### **4.1 Introduction**

When a ground vehicle moves on a curved path, the direction it moves (course angle) is generally different from where it heads (heading angle). The difference between the course angle and the heading angle is the vehicle sideslip angle. Since GPS can provide the course angle by measuring vehicle velocity, the core of GPS-based sideslip angle estimation methodology is accurate heading angle estimation.

Bevly proposed to use a single-antenna GPS receiver [20-23]. In his method, the vehicle yaw angle was calculated by integrating the yaw rate measurement from IMU. Due to the integration, the yaw angle estimation error would grow with time when the yaw rate sensor bias is inaccurately known. Even when the bias is precisely known, the standard deviation of the yaw angle estimation error grows proportional to the square root of past time due to white noise [20]. Hrovat [25] and Farrell [26] proposed to use multiple GPS receivers. In their method, the vehicle heading angle is calculated by using accurate position measurements of each GPS. However, only CDGPS can meet the required position accuracy of the method. As CDGPS needs a reference station and its price is very high, their method is not practical today. Ryu [28-29] took a different approach in using multiple GPS receivers. CDGPS can directly measure the vehicle heading angle without a reference station. This is possible by measuring the phase shift of the carrier wave arriving at two different GPS antennas. As the course and heading angles are provided, the sideslip angle is easily calculated. However, this technology is too expensive to be adopted by car makers today.

In short, the GPS-based sideslip angle estimation methods proposed so far have either performance limitations or cost concerns. A practical method

- must be low-cost
- should not require a reference station
- should not solely rely on measurement integration

To meet these conditions, the author proposes to use the kinematic relationship of two GPS receivers.

## 4.2 Kinematic Approach

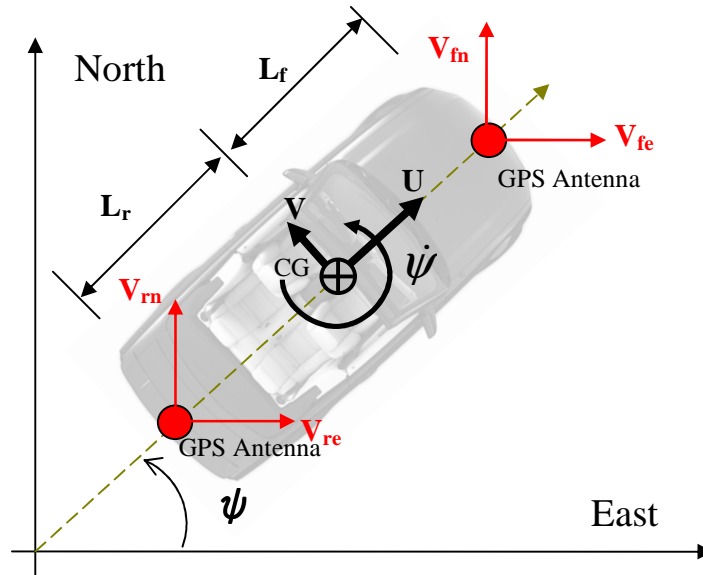


Figure 4.1 Top view of a ground vehicle with two GPS receivers on the horizontal plane

Figure 4.1 shows the top view of a ground vehicle with two single antenna GPS receivers installed at the front and rear ends of the vehicle.  $V_{fe}$  and  $V_{fn}$  are eastbound and northbound velocities of the GPS receiver at the front.  $V_{re}$  and  $V_{rn}$  are eastbound and northbound velocities of the GPS receiver at rear.  $U$  and  $V$  are longitudinal and lateral velocities of the vehicle at center of gravity and  $\dot{\psi}$  is the yaw rate.  $L_f$  and  $L_r$  are the distances from CG to front and rear end, respectively. The variables above are kinematically related as

$$V_{fe} = U \cos \psi - (V + L_f \dot{\psi}) \sin \psi \quad (4.1)$$

$$V_{fn} = U \sin \psi + (V + L_f \dot{\psi}) \cos \psi \quad (4.2)$$

$$V_{re} = U \cos \psi - (V - L_r \dot{\psi}) \sin \psi \quad (4.3)$$

$$V_{rn} = U \sin \psi + (V - L_r \dot{\psi}) \cos \psi \quad (4.4)$$

Equations (4.1)-(4.4) show that velocities measured by the two GPS receivers are nonlinear functions of longitudinal/lateral velocities, the yaw angle, and the yaw rate ( $U, V, \psi, \dot{\psi}$ ). Since the number of equations matches the number of unknowns, it may be a critically determinant system. If so, U and V can be expressed as functions of ( $V_{fe}, V_{fn}, V_{re}, V_{rn}$ ) by solving the above equations. In other words, the vehicle sideslip angle can be estimated by measuring the horizontal velocities of two single antenna GPS receivers. Since this method utilizes only velocity information, (i) it can be low-cost, (ii) it does not need a reference station, and (iii) no measurement integration is needed. Consequently, this method meets all the requirements listed in Section 4.1.

### 4.3 Singularity Analysis of the Kinematic Approach

#### 4.3.1 Singularity Analysis

Even though the number of equations matches the number of unknowns, (4.1)-(4.4) may have singular conditions where ( $U, V, \psi, \dot{\psi}$ ) cannot be expressed as function of ( $V_{fe}, V_{fn}, V_{re}, V_{rn}$ ). To find the singular point(s), the Multivariable Taylor's Theorem [60] is applied to yield (4.5).

$$\begin{bmatrix} \delta V_{fe} \\ \delta V_{fn} \\ \delta V_{re} \\ \delta V_{rn} \end{bmatrix} = \begin{bmatrix} \cos \psi & -\sin \psi & -U \sin \psi - (V + L_f \dot{\psi}) \cos \psi & -L_f \sin \psi \\ \sin \psi & \cos \psi & U \cos \psi - (V + L_f \dot{\psi}) \sin \psi & L_f \cos \psi \\ \cos \psi & -\sin \psi & -U \sin \psi - (V - L_r \dot{\psi}) \cos \psi & L_r \sin \psi \\ \sin \psi & \cos \psi & U \cos \psi - (V - L_r \dot{\psi}) \sin \psi & -L_r \cos \psi \end{bmatrix} \begin{bmatrix} \delta U \\ \delta V \\ \delta \psi \\ \delta \dot{\psi} \end{bmatrix} + H.O.T \quad (4.5)$$



where  $\delta$  means deviation from the current state. The 4-by-4 matrix in (4.5) is a Jacobian of (4.1)-(4.4), and it expresses the relationship between infinitesimal change of  $(U, V, \psi, \dot{\psi})$  and  $(V_{fe}, V_{fn}, V_{re}, V_{rn})$  with the higher order terms removed. If the Jacobian is not full rank, change in  $(U, V, \psi, \dot{\psi})$  may not be manifested by measuring  $(V_{fe}, V_{fn}, V_{re}, V_{rn})$ . This condition is considered as singularity. Since the determinant of Jacobian has a simple form of (4.6), (4.5) is singular if and only if the vehicle yaw rate is zero.

$$\det(J) = L^2 \dot{\psi} \quad (4.6)$$

Figure 4.2 gives an intuitive explanation why zero yaw rate corresponds to the singular condition. When the vehicle yaw rate is zero, velocities of the two GPS receivers will be identical for two distinct cases of A and B. Therefore it is impossible to calculate the vehicle yaw angle when the yaw rate is zero. In other words, velocities of the two GPS receivers need to be coupled with the yaw angle through a non-zero yaw rate.

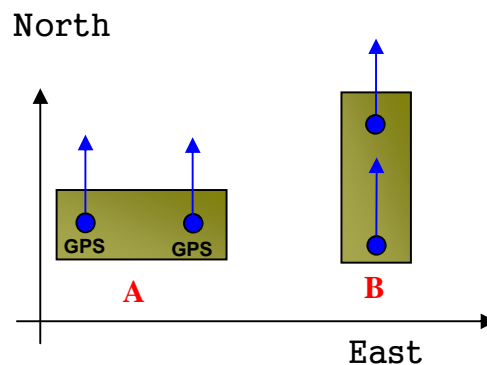


Figure 4.2 Top view of two vehicles with different yaw angles when yaw rate is zero

#### 4.3.2 Resolution Analysis

As shown in Section 2.3, the GPS velocity measurement contains only white noise. The impact of the white noise in GPS velocity measurements on the accuracy of  $(U, V, \psi, \dot{\psi})$  calculation is analyzed here. Equation (4.5) couples the measurement error of

$(V_{fe}, V_{fn}, V_{re}, V_{rn})$  and the estimation error of  $(U, V, \psi, \dot{\psi})$ . By assuming negligible higher order terms, deviation of the four states  $(U, V, \psi, \dot{\psi})$  can be obtained by inverting the Jacobian matrix as shown in (4.7) when the yaw rate is not zero (non-singular). Justification of ignoring the higher order terms is provided in Appendix B.

$$\begin{bmatrix} \delta U \\ \delta V \\ \delta \psi \\ \delta \dot{\psi} \end{bmatrix} = J^{-1} \begin{bmatrix} \delta V_{fe} \\ \delta V_{fn} \\ \delta V_{re} \\ \delta V_{rn} \end{bmatrix} \quad (4.7)$$

Standard deviation of a linear combination of two signals is computed from

$$\sigma^2(aX + bY) = a^2\sigma^2(X) + b^2\sigma^2(Y) + 2abCov(X, Y) \quad (4.8)$$

By applying (4.8) to (4.7) and by assuming the standard deviation of the GPS horizontal velocities are identical, (4.9) and (4.10) are obtained. Detailed derivations are provided in Appendix B.

$$\frac{\sqrt{2\sigma^2(\delta V_{gps}) - 2|Cov(\delta V_n, \delta V_e)|}}{|L\dot{\psi}|} \leq \sigma(\delta \psi) \leq \frac{\sqrt{2\sigma^2(\delta V_{gps}) + 2|Cov(\delta V_n, \delta V_e)|}}{|L\dot{\psi}|} \quad (4.9)$$

$$\left| \sigma^2(\delta \beta) - \frac{(2U^2 + (L_f^2 + L_r^2)\dot{\psi}^2)\sigma^2(\delta V_{gps})}{(LU\dot{\psi})^2} \right| \leq \frac{(2U^2 + (L_f^2 + L_r^2)\dot{\psi}^2)|Cov(\delta V_n, \delta V_e)|}{(LU\dot{\psi})^2} \quad (4.10)$$

where  $\sigma(\delta V_{GPS})$  is the standard deviation of the GPS velocity measurement error and  $Cov(\delta V_n, \delta V_e)$  is the covariance of north-/east-bound GPS velocities.  $\beta$  is defined as

$\tan^{-1}(V/U)$ . Figure 4.3 shows the graphs of (4.9) and (4.10). In the graphs,  $Cov(\delta V_n, \delta V_e)$  is assumed to be zero for the succinctness. Since a lower standard deviation means a more accurate measurement, it is apparent that the higher the vehicle yaw rate is, the more accurate yaw/sideslip angle calculations will become. When the yaw rate is zero, standard deviation reaches infinity. This agrees with what we found from the singularity analysis.

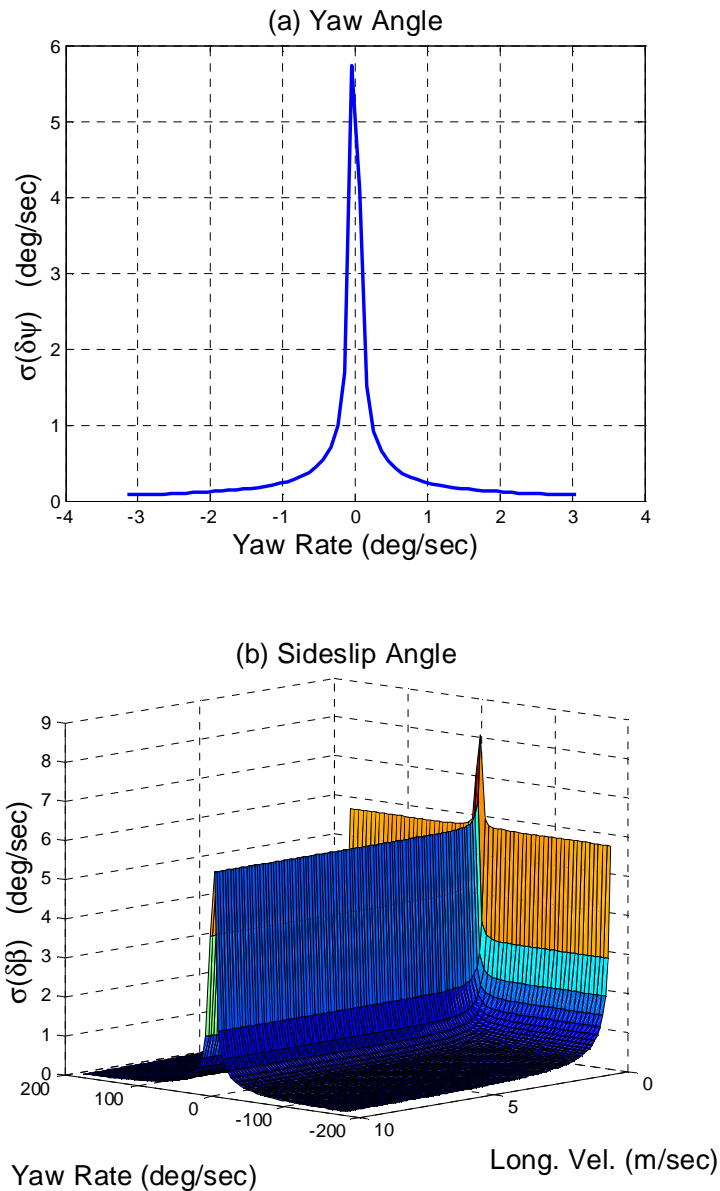


Figure 4.3 Accuracy of (a) yaw angle and (b) sideslip angle measurement from two GPS velocities as a function of yaw rate and longitudinal velocity.

Table 4.1 presents the upper/lower bounds of the standard deviation of sideslip errors for selected yaw rate values. This table uses  $L = 4.8$  m,  $U = 10$  m/s, and  $\sigma(\delta V_{GPS}) = 0.01$  m/s,  $Cov(\delta V_n, \delta V_e) = -3 \times 10^{-5}$ .  $L$  of 4.8 m is from the test vehicle used for the experimental validation.  $\sigma(\delta V_{GPS})$  and  $Cov(\delta V_n, \delta V_e)$  are measured from the GPS receiver used for the experiment. The official ‘Sine with Dwell’ maneuver from FMVSS126 can excite the vehicle yaw rate up to 50 °/sec [61-62]. Therefore the yaw rate magnitude selection of Table 4.1 is reasonable.

Table 4.1 The standard deviation of sideslip angle measurement error

Yaw rate (deg/sec)		10	15	30
$\sigma(\beta)$	Upper bound	<b>1.1</b>	<b>0.73</b>	<b>0.37</b>
	Lower bound	<b>0.8</b>	<b>0.54</b>	<b>0.27</b>

A Monte-Carlo simulation study was conducted to validate the accuracy analysis above. A Gaussian white noise (mean: 0 m/s, standard deviation: 0.01 m/s) was injected in each GPS velocity simulation.  $L$  was set to 4.8m, longitudinal velocity was fixed at 10 m/s, the yaw rate was varied from 0 to 45°/sec, and a total of 200 simulations were run. Figure 4.4 (a) shows the estimation of sideslip/yaw angle as a function of yaw rate when the GPS velocity is contaminated by Gaussian white noise. The red line is true value and blue dots are estimations by the proposed method. It is clearly seen that when the yaw rate is small, the estimation has a large error. Figure 4.4 (b) shows the standard deviation of the estimation error. The Monte-Carlo simulation confirms that yaw/sideslip angle estimation accuracy is dependent on the yaw rate.

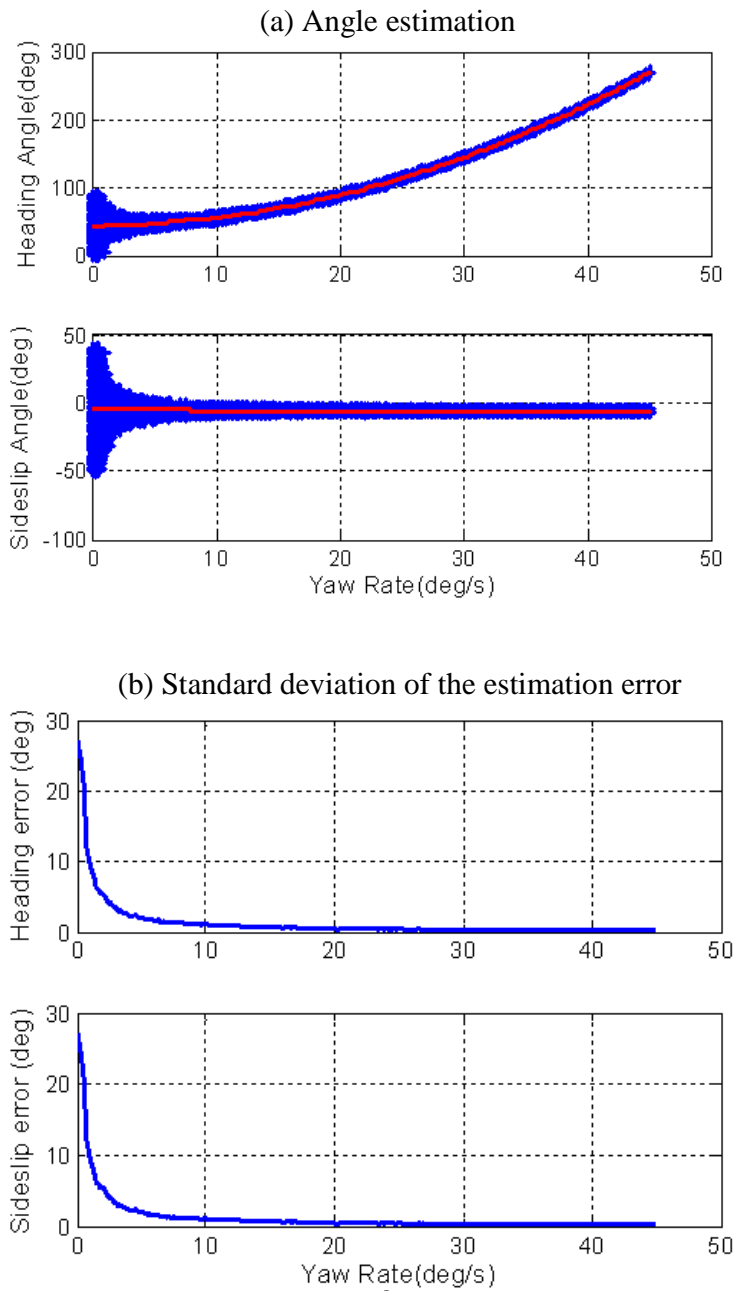


Figure 4.4 Monte-Carlo simulation results: (a) yaw/sideslip angle estimation with the presence of Gaussian white noise in the GPS velocity measurement (b) standard deviation of estimation error as a function of yaw rate

## 4.4 Sensor Fusion through the Kalman Filter

### 4.4.1 Sensors

One IMU and two GPS receivers are utilized in this study. The IMU provides yaw rate, longitudinal acceleration, and lateral accelerations. The two GPS receivers provide velocity measurements of two positions on the vehicle. The GPS receiver used for this research (U-blox EVK-5H) has an update rate of 2.5 Hz. By the way, the update rate of 10 Hz or above is required because the vehicle dynamic modes span in the 1-4 Hz range [20]. Consequently, the GPS of 2.5 Hz update rate cannot be the only sensor for sideslip estimation. As an alternative, the GPS signals are merged with an IMU measurement to take advantage of the high update rate of IMU measurements (in the range of 100 Hz). In fact, MEMS-based IMUs (lower-cost) are known to have biases where a GPS velocity measurement has only unbiased white noise. These complementary properties of GPS and IMU signals make them an ideal pair for fusion (Table 4.2).

Table 4.2 Comparison of GPS and IMU signals

GPS	IMU
<ul style="list-style-type: none"><li>• Unbiased noise</li><li>• Low update rate</li></ul>	<ul style="list-style-type: none"><li>• Biased noise</li><li>• High update rate</li></ul>

#### 4.4.1.1 Delays in GPS Signal

GPS measurements have time delays. The GPS receivers used in this research estimate its velocity by interpreting the change in carrier phase between successive samples. This way is known to have an inherent latency equal to one half of the sampling time in delivering velocity measurements [33]. Accordingly, the update frequency of 2.5 Hz would have on average a 200 ms latency solely due to this. Moreover, the internal data processing time (<300 ms according to the product specification) of the GPS module and other communication time add to the total delay. Figure 4.5 shows a schematic diagram of the measurement system. The delays are highlighted in red fonts. Since the

IMU signals have 6 ms delay at most, they are considered as real-time measurements. A blue dashed box represents an enclosed unit, hence no direct access is allowed.

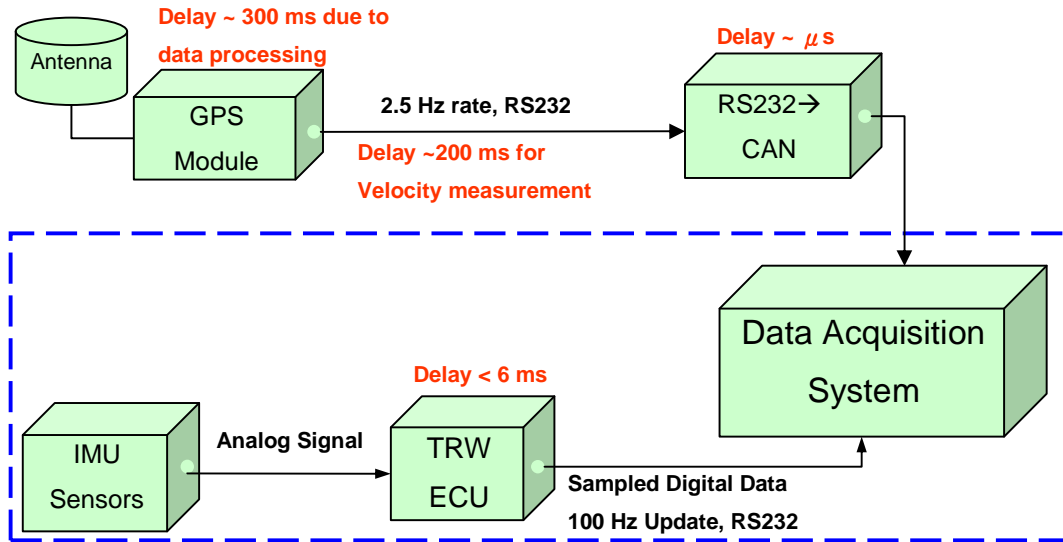


Figure 4.5 Schematic diagram of the measurement

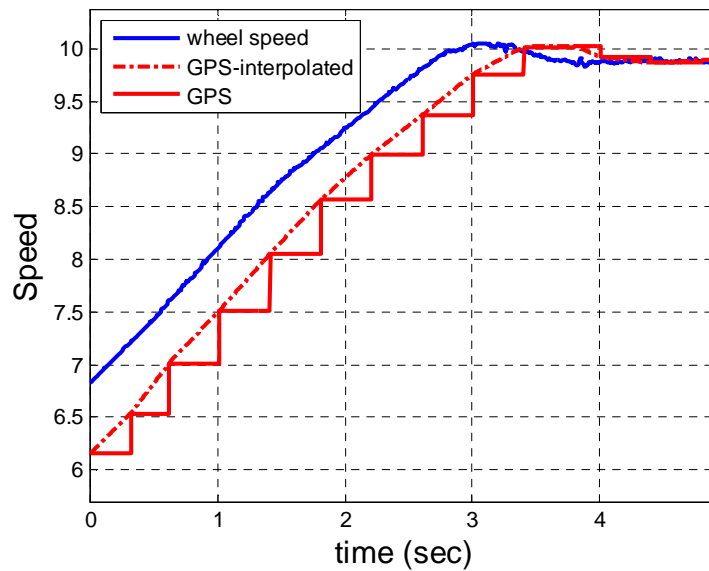


Figure 4.6 Delays in GPS velocity measurement

Figure 4.6 shows a set of vehicle test data on a high frictional surface. The blue line is the vehicle speed from the wheel speed sensor and the red solid line is a GPS velocity measurement. The GPS velocity measurement has a staircase shape due to the low update rate. The red dashed line is the interpolated signal. The time gap between the blue and red dashed line confirms the existence of delay in the GPS measurements. The ‘measurement shift’ technique introduced in 3.3.1 is employed to address the delay. The amount of delay is calculated by comparing GPS velocity with the velocity from wheel speed sensors when the vehicle accelerates smoothly. Therefore the time delay is treated as a known value in this study.

#### 4.4.1.2 Unsynchronized GPS Updates

The author mounts two GPS receivers on a vehicle and collects data independently. As those receivers do not communicate, measurement update triggers of those receivers are not synchronized.

Figure 4.7 shows a typical velocity profile from two individual single antenna GPS receivers. Both lines represent eastbound velocities. The red line is from the receiver located at the front end of a vehicle and the blue line is from the receiver at the rear end. Apparently, updates of the two receivers are not synchronized. ‘Asynchronous update’ technique introduced in 3.3.2 is used to address the accuracy degradation due to the unsynchronized outputs.

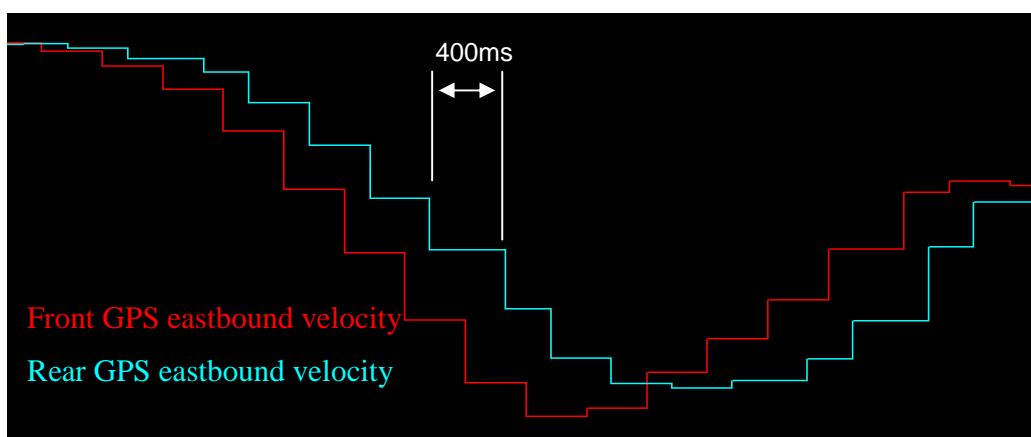


Figure 4.7 A typical velocity profile from two GPS receivers



#### 4.4.2 The Kalman Filter Implementation

##### 4.4.2.1 Plant and Measurement Update Equations

Equations (4.11)-(4.13) are kinematics in IMU measurements.

$$a_{xm} = \dot{U} - V\dot{\psi} + b_x + w_x \quad (4.11)$$

$$a_{ym} = \dot{V} + U\dot{\psi} + b_y + w_y \quad (4.12)$$

$$r_m = \dot{\psi} + b_r + w_r \quad (4.13)$$

where  $a_{xm}$  and  $a_{ym}$  are longitudinal and lateral acceleration measurements.  $U$  and  $V$  are longitudinal and lateral velocities.  $\psi$  is the vehicle yaw angle.  $r_m$  is yaw rate measurements.  $b_x$ ,  $b_y$  and  $b_r$  are constant biases in  $a_{xm}$ ,  $a_{ym}$  and  $r_m$ , respectively.  $w_x$ ,  $w_y$  and  $w_r$  are Gaussian white noises. These equations are rearranged to form a differential equation and they are used as ‘time update’ equations. The bias in yaw rate ( $b_r$ ) can be estimated accurately during vehicle standstill. Biases in accelerometers ( $b_x$ ,  $b_y$ ) are calculated by averaging raw signals when vehicle is driven straight. To remove road grade/bank influence, the averaging occurs over an extended period of up to an hour.

$$\begin{bmatrix} \dot{U} \\ \dot{V} \\ \dot{\psi} \end{bmatrix} = \begin{bmatrix} 0 & \dot{\psi} & 0 \\ -\dot{\psi} & 0 & 0 \\ 0 & 0 & 0 \end{bmatrix} \begin{bmatrix} U \\ V \\ \psi \end{bmatrix} + \begin{bmatrix} 1 & 0 & 0 \\ 0 & 1 & 0 \\ 0 & 0 & 1 \end{bmatrix} \begin{bmatrix} a_{xm} - b_x \\ a_{ym} - b_y \\ r_m - b_r \end{bmatrix} + \begin{bmatrix} 1 & 0 & 0 \\ 0 & 1 & 0 \\ 0 & 0 & 1 \end{bmatrix} \begin{bmatrix} w_x \\ w_y \\ w_r \end{bmatrix} \quad (4.14)$$

GPS velocity measurements of (4.1)-(4.4) are used for the ‘measurement update’. As these equations are nonlinear, the Extended Kalman Filter (EKF) technique is employed. The asynchronous update technique discussed in Section 3.3.2 is applied here. So, when the front GPS measurement is updated, (4.1)-(4.2) are employed as the measurement update equation. The measurement matrix ( $H_k$  of (3.8)) is

$$H_k = \begin{bmatrix} \cos \psi_k & -\sin \psi_k & -U_k \sin \psi_k - (V_k - L_f \dot{\psi}_k) \cos \psi_k \\ \sin \psi_k & \cos \psi_k & U_k \cos \psi_k - (V_k + L_f \dot{\psi}_k) \sin \psi_k \end{bmatrix} \quad (4.15)$$

When the rear GPS measurement is updated, (4.3)-(4.4) are used and the corresponding  $H_k$  is

$$H_k = \begin{bmatrix} \cos \psi_k & -\sin \psi_k & -U_k \sin \psi_k - (V_k + L_r \dot{\psi}_k) \cos \psi_k \\ \sin \psi_k & \cos \psi_k & U_k \cos \psi_k - (V_k - L_r \dot{\psi}_k) \sin \psi_k \end{bmatrix} \quad (4.16)$$

$H_k$  is set to zero matrix if measurements are not updated. Once  $U$  and  $V$  are estimated, the vehicle sideslip angle is calculated from  $\tan^{-1}(V/U)$ . The analysis in Section 4.3.2 reveals that the accuracy of the vehicle sideslip angle measurement by two GPS receivers is dependent on the vehicle yaw rate. To reflect this fact, GPS measurements are registered as valid only when the absolute value of yaw rate is greater than a threshold. In this study, 10 °/s is set as the threshold. The schematic diagram is presented in Figure 4.8.

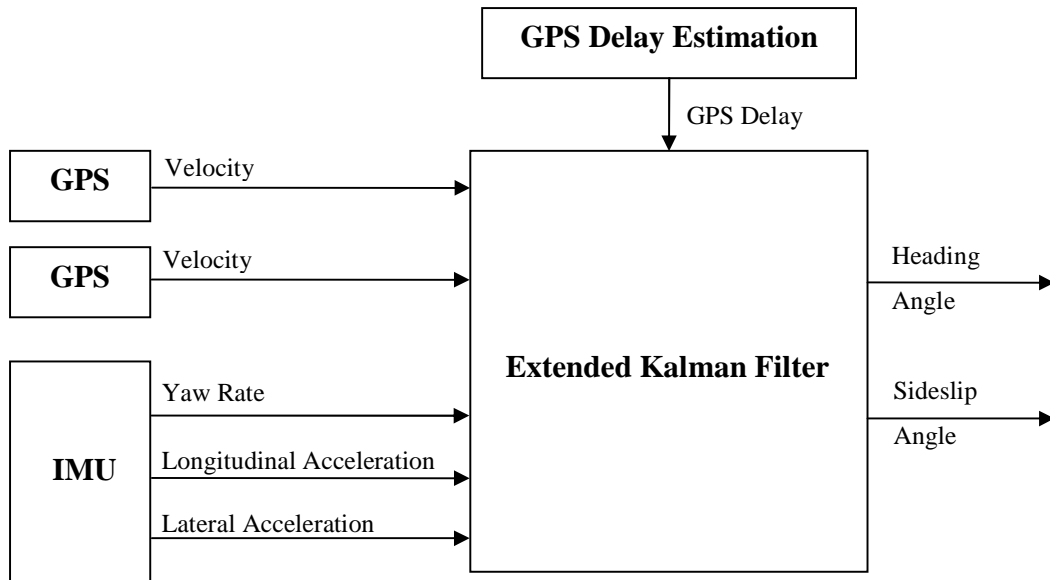


Figure 4.8 Schematic diagram of the two-GPS method. Equations (4.1)-(4.4) and (4.11)-(4.13) are used.

#### 4.4.2.2 Discretization

To realize the Kalman filter on a computer, (4.14) is digitized. Equation (4.14) is symbolized as (4.17), where  $x(t)$  is a state,  $u(t)$  is an input and  $w(t)$  is a noise. Integration of (4.14) from  $t_{k-1}$  to  $t_k$  yields (4.18) [42].

$$\dot{x}(t) = F(t)x(t) + Gu(t) + Lw(t) \quad (4.17)$$

$$x(t_k) = \Phi(t_k, t_{k-1})x(t_{k-1}) + \int_{t_{k-1}}^{t_k} \Phi(t_k, \tau)[Gu(\tau) + Lw(\tau)]d\tau \quad (4.18)$$

If  $\Delta T (\equiv t_k - t_{k-1})$  is small enough,  $F(t)$  can be considered as a constant matrix inside the time step of  $[t_{k-1}, t_k)$ . The constant matrix  $F$  would be  $F(t_{k-1})$ . In that case,  $\Phi(t_k, t_{k-1})$  is equal to  $e^{F\Delta T}$ . Therefore (4.18) is changed to

$$x(t_k) = e^{F\Delta T}x(t_{k-1}) + \int_{t_{k-1}}^{t_k} e^{F(t_k-\tau)}Gu(\tau)d\tau + \int_{t_{k-1}}^{t_k} e^{F(t_k-\tau)}Lw(\tau)d\tau \quad (4.19)$$

$\Delta T$  in this study is 6 ms. The input  $u(\tau)$  is the measurement of an IMU. Since the frequency content of the input (1-4 Hz, [20]) is much slower than the sampling rate (166 Hz),  $u(\tau)$  in (4.19) can be considered as a constant ( $u(t_{k-1})$ ). This yields (4.20) where  $x_k$  is  $x(t_k)$  and  $u_{k-1}$  is  $u(t_{k-1})$ .

$$x_k = e^{F\Delta T}x_{k-1} + [e^{F\Delta T} - I]F^{-1}Gu_{k-1} + \int_{t_{k-1}}^{t_k} e^{F(t_k-\tau)}Lw(\tau)d\tau \quad (4.20)$$

$$\hat{x}_k = e^{F\Delta T}\hat{x}_{k-1} + [e^{F\Delta T} - I]F^{-1}Gu_{k-1} \quad (4.21)$$

As state estimation follows (4.21), the expected value of the state covariance ( $P_k$ ) is

$$\begin{aligned}
P_k &\equiv \mathcal{E}\{(x_k - \hat{x}_k)(x_k - \hat{x}_k)^T\} \\
&= e^{F\Delta T} P_{k-1} (e^{F\Delta T})^T + \mathcal{E}\left\{\left[\int_{t_{k-1}}^{t_k} e^{F(t_k-\tau)} L w(\tau) d\tau\right] \left[\int_{t_{k-1}}^{t_k} e^{F(t_k-\tau)} L w(\tau) d\tau\right]^T\right\} \\
&= e^{F\Delta T} P_{k-1} (e^{F\Delta T})^T + \int_{t_{k-1}}^{t_k} \int_{t_{k-1}}^{t_k} e^{F(t_k-\tau)} L \mathcal{E}\{w(\tau) w^T(\alpha)\} L^T (e^{F(t_k-\alpha)})^T d\alpha d\tau
\end{aligned} \tag{4.22}$$

Given  $\mathcal{E}\{w(t)w^T(\tau)\} = Q_c' \delta(t-\tau)$  where  $Q_c'$  is the power spectral density matrix and  $\delta(t-\tau)$  is the Dirac delta function, (4.22) is rewritten as

$$P_k = \Phi_{k-1} P_{k-1} \Phi_{k-1}^T + \int_0^{\Delta T} e^{F\tau} L Q_c' L^T (e^{F\tau})^T d\tau \tag{4.23}$$

Where  $\Phi_{k-1}$  stands for  $e^{F\Delta T}$ . If  $\Delta T$  is very short compared to the system time constants,  $e^{F\Delta T} \approx I + F\Delta T$  and  $e^{F\tau} \approx I$ . Then (4.21) and (4.23) become

$$\hat{x}_k = \Phi_{k-1} \hat{x}_{k-1} + G\Delta T u_{k-1} \tag{4.24}$$

$$P_k = \Phi_{k-1} P_{k-1} \Phi_{k-1}^T + \Lambda Q_c' \Lambda^T \tag{4.25}$$

where  $\Lambda = L\Delta T$  and  $Q_c' = \frac{Q_c}{\Delta T}$ . Equations (4.24)-(4.25) are derived from a continuous system and they are the ‘time update’ of the Kalman filter.

#### 4.4.3 Observability Analysis

Theories presented in Section 3.2 are applied to (4.14)-(4.16) to analyze the stochastic observability. Since this is a linear time-varying system, the observability is dependent on trajectories of the state. Therefore the author followed procedures below.

- Choose a maneuver
- Choose an integer  $N$  of (3.20)
- Build  $O(k, k-N)$  and  $C(k, k-N)$  of (3.18) and (3.19)

- Evaluate  $\alpha_o, \beta_o, \alpha_c,$  and  $\beta_c$  of (3.18) and (3.19)

Since  $P_0$  is set to be positive definite, this system is stochastically observable as long as all of  $\alpha_o, \beta_o, \alpha_c,$  and  $\beta_c$  are positive according to (3.23).

Test maneuvers include single lane changes (SLC), double lane changes (DLC), slaloms (SLL), and J-turns. The data collected on high friction surface is used.  $N$  of 1, 2, and 3 are tried. The stochastic observability is governed by system matrices (i.e.  $\Phi_{k,k-1}, \Gamma_{k-1}$  and  $H_k$  of (3.4) and (3.5)). In other words, it scrutinizes if the system matrices are properly structured to be observable or not. Since the measurement delay does not influence system matrices, the delay is not considered during this analysis. On the other hand, the unsynchronized measurement updates of two GPS receivers change the system matrices compared to the synchronized update. If both GPS receivers update at the same time,  $H_k$  would be  $4 \times 3$  by combining (4.15) and (4.16). If not,  $H_k$  would be either (4.15) or (4.16) according to the updated GPS. Both synchronized/unsynchronized GPS update cases are analyzed.

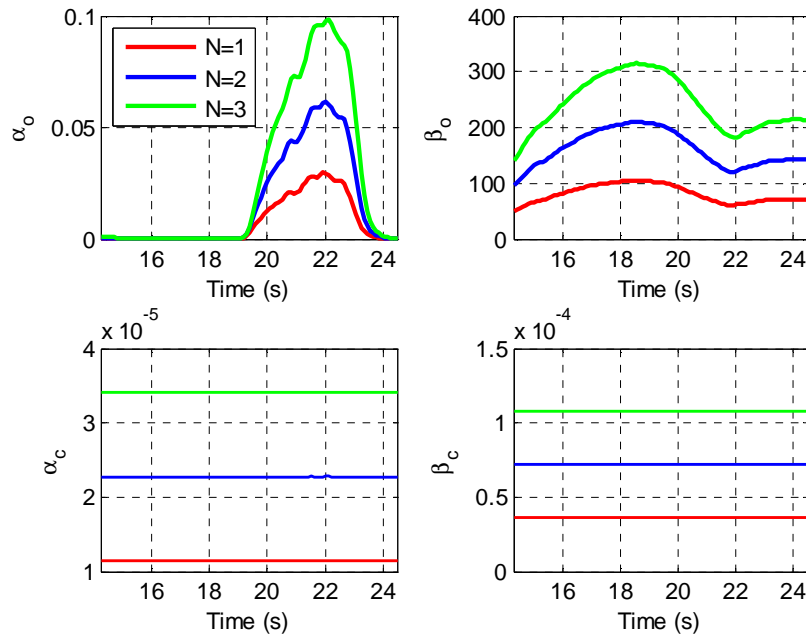


Figure 4.9  $\alpha_o, \beta_o, \alpha_c,$  and  $\beta_c$  of J-turn

Figure 4.9 shows  $\alpha_o$ ,  $\beta_o$ ,  $\alpha_c$ , and  $\beta_c$  of a J-turn with synchronized GPS updates. Three different colors stand for different levels of  $N$ . In the figure,  $\beta_o$ ,  $\alpha_c$ , and  $\beta_c$  are positive all the time and only  $\alpha_o$  is the limiting factor from the observability perspective. In fact, this trend is observed through all the processed data. Therefore  $\alpha_o$  is investigated further.

Figure 4.10 shows the minimum eigen value ( $\alpha_o$ ) of  $O(k, k-N)$  and its corresponding yaw rate of a J-turn maneuver. Solid lines represent the synchronized GPS update case and dotted lines are for the unsynchronized case.

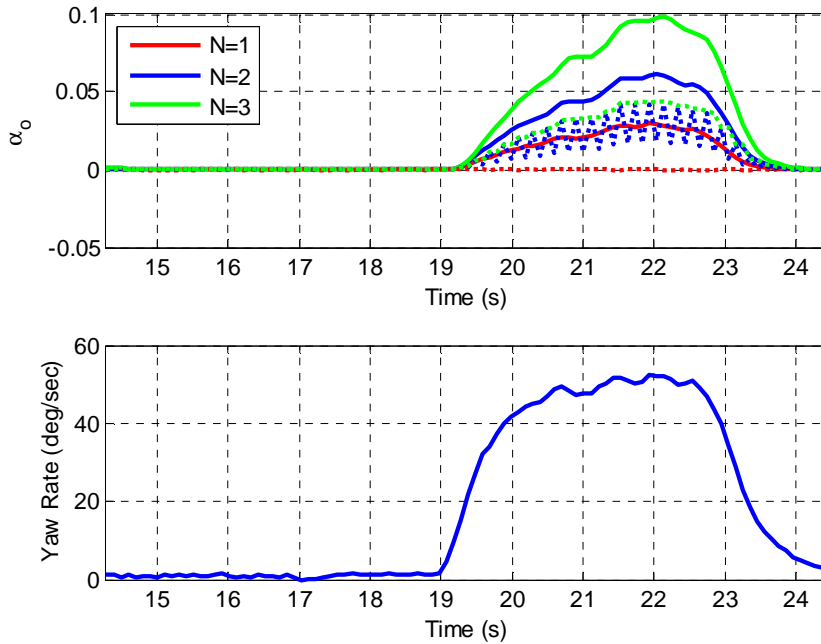


Figure 4.10 The minimum eigen value ( $\alpha_o$ ) of  $O(k, k-N)$  and its corresponding yaw rate of a J-turn maneuver

In the figure, the dependency of  $\alpha_o$  on the yaw rate is clearly visible. When the yaw rate is around zero,  $\alpha_o$ 's of all the  $N$ 's are also zero. On the other hand, when the yaw rate is substantial (within the time window 15 sec~20 sec),  $\alpha_o$ 's are all positive regardless of  $N$  for the synchronized measurement update case. Consequently the stochastic observability

is guaranteed only when the yaw rate is substantial. It is worth recognizing that this result is consistent with the outcome of accuracy analysis in Section 4.3.

The influence of unsynchronized measurement updates is also demonstrated in the figure. Dotted lines are lower than solid lines of same color. This implies that the observability of the unsynchronized update case is weaker than the synchronized case. Since the dotted lines of  $N=2$  or  $3$  are positive during vehicle turning, this Kaman Filter is stochastically observable even with the unsynchronized measurement update as long as the vehicle yaw rate is significant. Figure 4.11-Figure 4.13 present of  $\alpha_o$ 's other maneuvers (SLC, DLC and SLL). The same conclusions about yaw rate dependency and unsynchronized update influence are drawn.

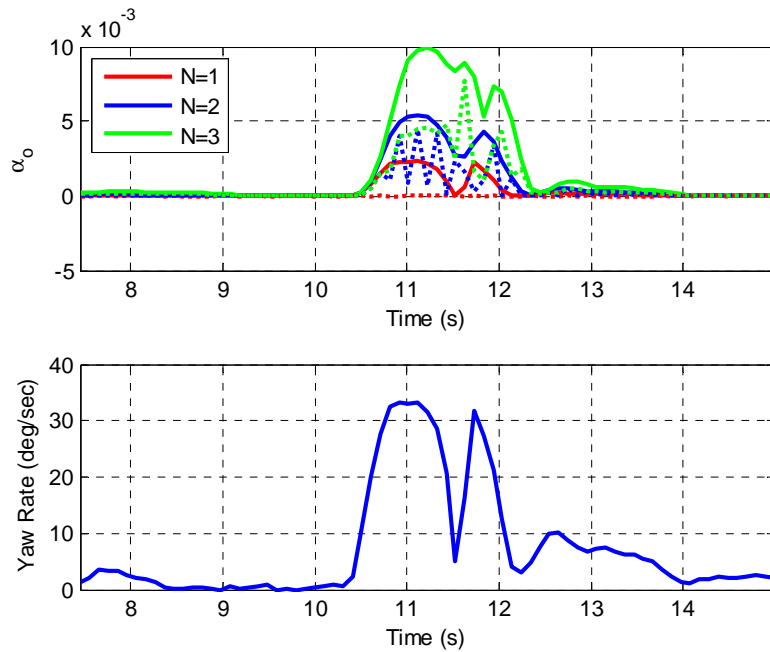


Figure 4.11 The minimum eigen value ( $\alpha_o$ ) of  $O(k, k - N)$  and its corresponding yaw rate of a single lane change maneuver

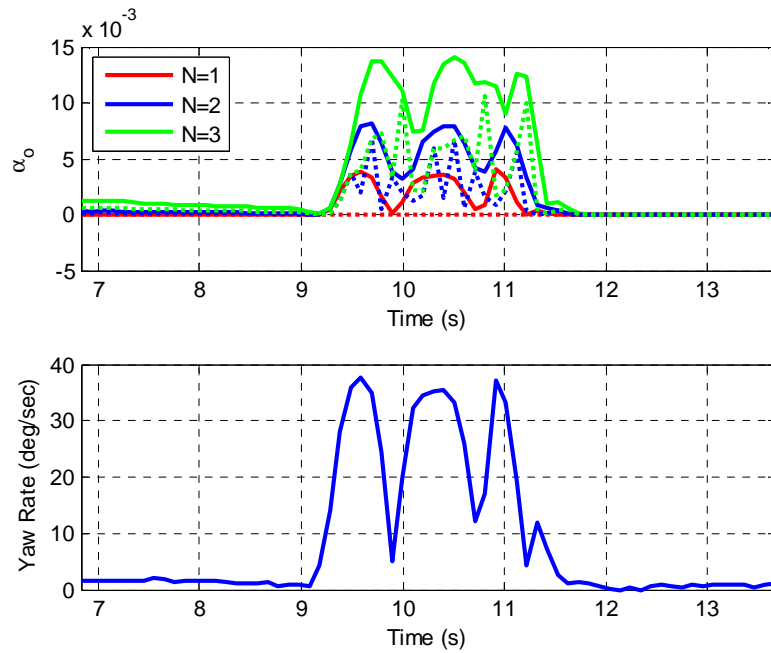


Figure 4.12 The minimum eigen value ( $\alpha_o$ ) of  $O(k, k - N)$  and its corresponding yaw rate of a double lane change maneuver

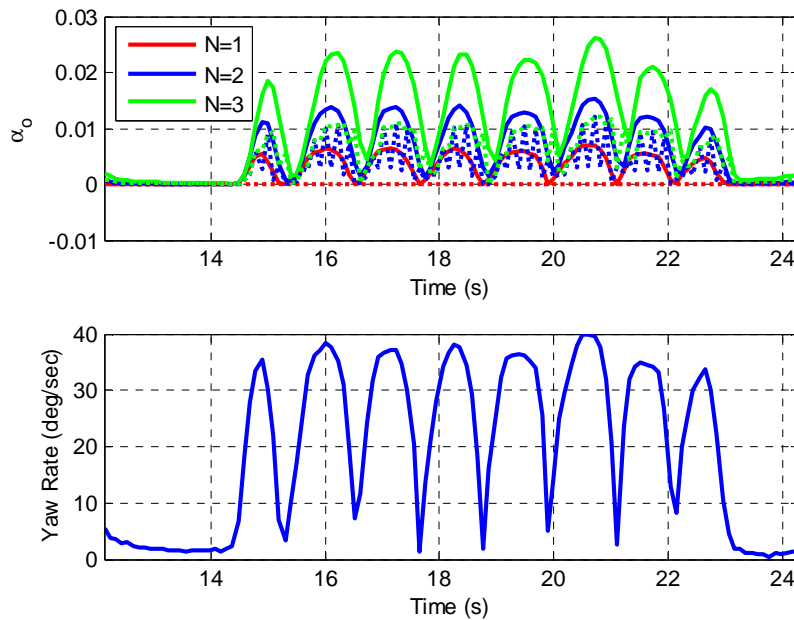


Figure 4.13 The minimum eigen value ( $\alpha_o$ ) of  $O(k, k - N)$  and its corresponding yaw rate of a slalom maneuver



#### 4.4.4 Bicycle Model

Results of the singularity analysis in Section 4.3.1 and the observability analysis in Section 4.4.3 reveal that the proposed method is incapable of estimating the vehicle sideslip when a vehicle is driving straight.

To address this issue, a bicycle model is incorporated. As described in Section 1.2.1, the bicycle model is a kinetic equation which combines the steering angle with the vehicle sideslip angle through vehicle parameters such as tire cornering stiffness as seen in (1.10). Figure 4.14 shows the performance of the bicycle model for a lane change maneuver on a snow covered surface. Vehicle parameters  $C_f, C_r, m$ , and  $I_z$  are manipulated to vary from 25% to 175% of the nominal values. The red line is the true sideslip angle and the blue lines represent estimations by the bicycle model with various vehicle parameters. As seen in the figure, the sideslip estimation is inaccurate during the lane change maneuver. Recall that the bicycle model requires accurate vehicle parameters and is reliable only for the linear range of the sideslip-lateral force relationship.

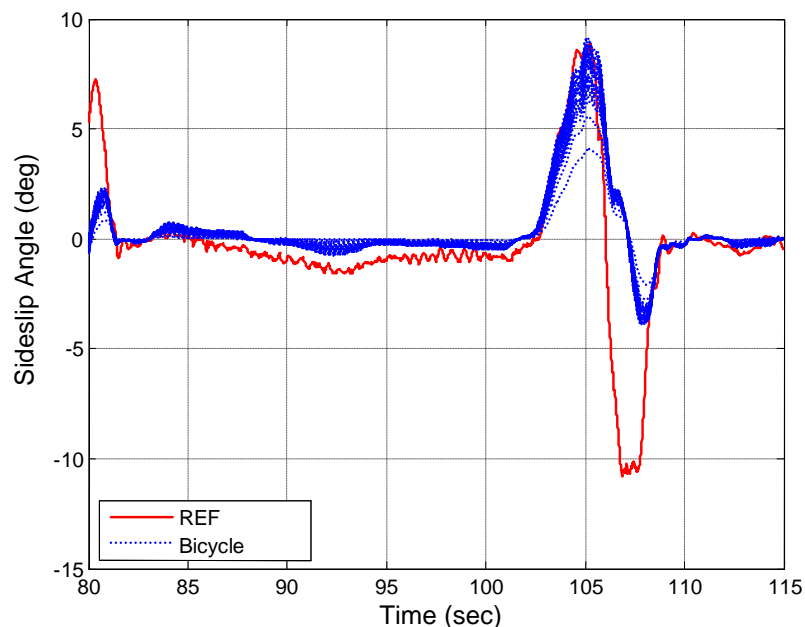


Figure 4.14 The vehicle sideslip angle estimation by a bicycle model with parameters of 25%~175% of nominal values.

However, it is worth noticing that the vehicle sideslip angle is accurately estimated during straight driving regardless of the parameter accuracy. In other words, the bicycle model can provide accurate sideslip estimation during straight driving even with inaccurate vehicle parameters. Therefore when a vehicle moves straight, the bicycle model is solely employed for the vehicle sideslip estimation.

## 4.5 Experimental Verification

### 4.5.1 Design Verification Test

#### 4.5.1.1 Test Purpose and Setup

A pilot test of J-turn on a wet tile (low friction) surface was conducted to verify the algorithm. This maneuver was chosen to generate large sideslip angles. Figure 4.15 shows the test maneuver. A vehicle was driven straight first and was steered abruptly right before entering into the wet tile. The steering angle was kept high while the vehicle was on the wet tile surface. A midsize pick-up truck was used on the TRW proving ground (Figure 4.16). Key parameters of the vehicle are shown in Table 4.3. The test vehicle was equipped with a production IMU, whose update rate is above 166 Hz. Sensor noise levels ( $1\sigma$ ) are  $0.02 \text{ m/s}^2$  for the accelerometer and  $0.08^\circ/\text{sec}$  for the yaw rate gyros. Two units of the U-blox EVK-5H GPS evaluation kit (\$200/each) were utilized. One GPS receiver was installed at the front end of the vehicle, the other at the rear. It provides 2.5 Hz velocity measurement with a noise level ( $1\sigma$ ) of 0.01 m/s. For the reference signal, an RT2500-250 unit from Oxford Technical Solutions was employed. According to its specification document, the error levels ( $1\sigma$ ) are  $0.3^\circ$  for the yaw angle and  $0.4^\circ$  for the sideslip angle.

Table 4.3 Test vehicle parameters (small size pickup truck - unloaded)

Wheel base (L)	4.8m
Front to CG Length ( $L_f$ )	1.91 m
Rear to CG Length ( $L_r$ )	2.89 m
CG Height	0.7 m
Vehicle Mass	1990 kg

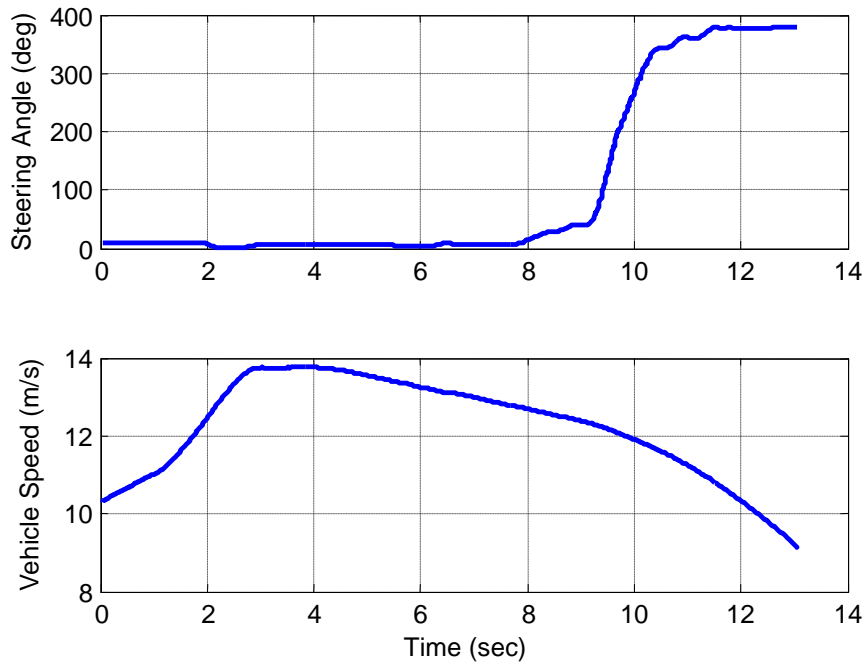


Figure 4.15 Test Maneuver: steering angle and vehicle speed



Figure 4.16 The wet tile surface of the TRW proving ground (Locke Township, MI)

#### 4.5.1.2 Estimation Performance

Figure 4.17 shows a result from the experiment. In subplots (a) and (b) of the figure, blue dotted lines represent estimations of the proposed method. Red solid lines are the reference signals from RT2500-250, which are considered as the true yaw/sideslip angles. The author also presents sideslip angle estimations from the IMU integration method (the dashed green lines) to demonstrate benefits of the proposed method over the IMU integration method.

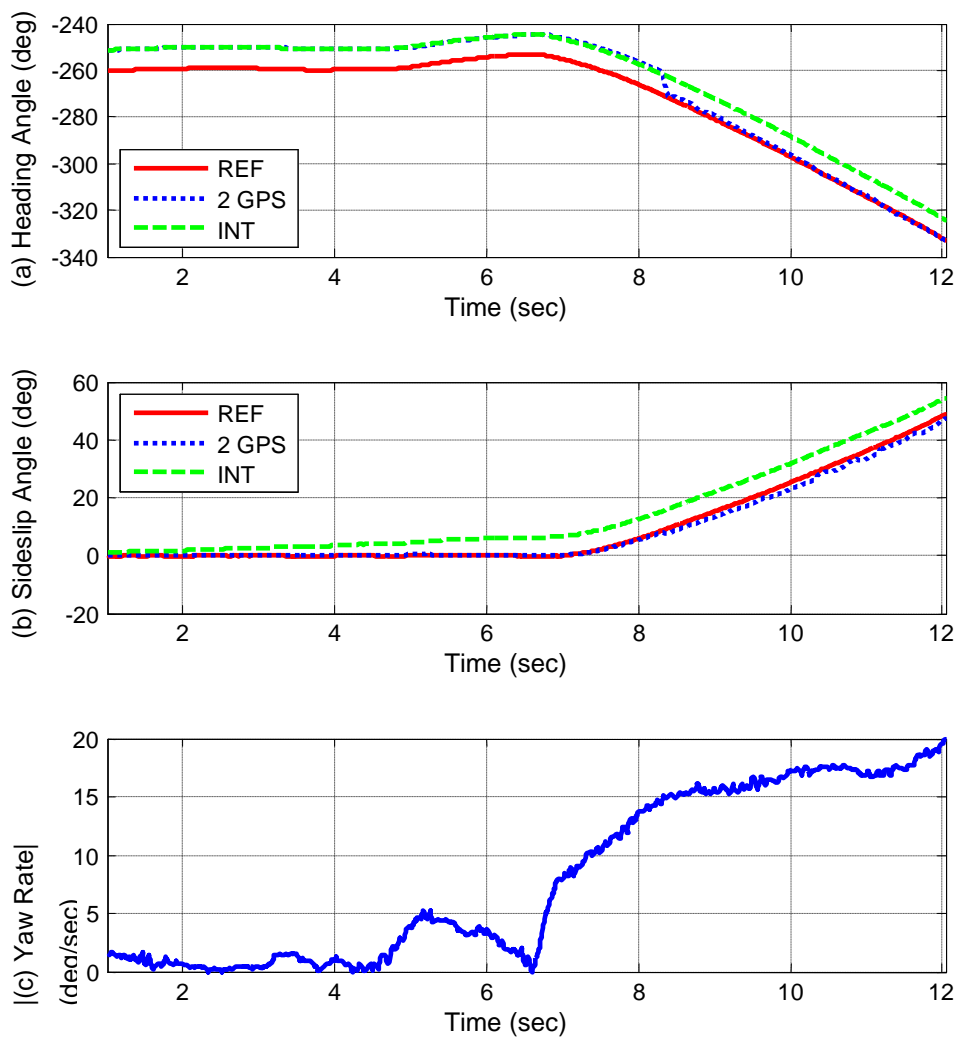


Figure 4.17 Experimental result; (a) yaw angle estimation, (b) sideslip angle estimation, (c) |yaw rate|

The test vehicle begins to generate considerable yaw rates from around the 8 second mark. Before that time mark, the GPS signals do not contribute to yaw/sideslip angle estimation. Hence the initial yaw error is not corrected. However, the sideslip estimation stays accurate because a bicycle model is employed during the time. From the 8 second mark, the yaw angle converges to the reference value and sideslip estimation stays accurate thanks to the update from the GPS measurements. The yaw rate threshold for intervention from GPS is  $10^\circ$ . The sideslip estimation from IMU integration (the green dashed line) diverges as time progresses while the sideslip error of the proposed method stays bounded (the blue dotted line). This shows the advantage of the proposed method over the IMU-based method.

A total of 18 valid data sets under J-turn maneuvers were collected and all of them show similar performances. The Root Mean Square (RMS) of the yaw and the sideslip error were calculated from the 18 data set. The yaw and sideslip errors are counted only when the absolute value of yaw rate exceeds the threshold ( $10^\circ/\text{s}$ ). The sideslip RMS error is  $2.8^\circ$ . This is degraded from the predicted performance in Section 4.3.2 (sideslip RMS upper bound of  $1.1^\circ$ ). This degradation may be due to errors in delay calculation and asynchronous GPS updates.

#### 4.5.2 Robustness Test

##### 4.5.2.1 Test Purpose and Setup

Robustness of the method was intensively tested. This test aims to evaluate the estimation performance with wider set of maneuvers at different road frictions. At this time, a sports car was used (Table 4.4). Various maneuvers including single lane changes (SLC), double lane changes (DLC), slaloms (SLL), and J-turns were executed on high-/mid-/low-frictional surfaces (asphalt/wet jennite/wet tile, respectively). The TRW proving ground at Locke township in Michigan was utilized again. Each test scenario has 9 repetitions. Therefore, a total of 108 ( $= 3 \text{ surfaces} \times 4 \text{ maneuvers} \times 9 \text{ repetitions}$ ) data sets were collected.

Table 4.4 Test vehicle parameters used in the robustness test (a sports car)

Wheel base (L)	4.45 m
Front to CG Length ( $L_f$ )	1.9 m
Rear to CG Length ( $L_r$ )	2.55 m
CG Height	0.5 m
Vehicle Mass	1765 kg

#### 4.5.2.2 Estimation Performance

Figure 4.18-Figure 4.21 show the sideslip estimation performances of single lane changes, double lane changes, slaloms, and J-turns. The red lines are the reference values from RT2500 and the blue dashed lines are estimations from the proposed method. The cyan blue envelops show the 95% confidence range calculated from the state error covariance matrices. In the figures, subplots (a) are from maneuvers on asphalt while subplots (c) are from wet tiles. Subplots (b) and (d) show absolute yaw rates of the corresponding data. The estimation error is tallied only when the magnitude of the vehicle yaw rate is greater than  $10^\circ/\text{s}$ .

The overall RMS error from 108 data set is  $2.6^\circ$ . The RMS error on a high friction surface ( $2.16^\circ$ ) is better than that on a low frictional surface ( $3.35^\circ$ ). This is because a higher yaw rate is generated on the high friction surface. According to the resolution analysis, the estimation becomes more accurate as the yaw rate magnitude increases.

Slalom on the asphalt (Figure 4.20 (a)) shows the worst performance. This is most likely because considerable roll angles were generated. Figure 4.22 shows the occurrence rate of vehicle roll angles during the slalom maneuver. On the asphalt, roll angles span  $\pm 4^\circ$  where on the wet tile the range is  $\pm 1^\circ$ . If a vehicle rolls, a portion of the gravity is exerted on the lateral accelerometer. However, (4.12) does not contain the term to consider the gravitational effect of the vehicle roll. With  $4^\circ$  of roll angles,  $0.68 \text{ m/s}^2$  is exerted by the gravity and this value works as an unknown bias in the proposed method. Therefore the estimation accuracy degrades severely. By virtue of corrections from two GPS measurements, the estimation error stays bounded rather than diverging.

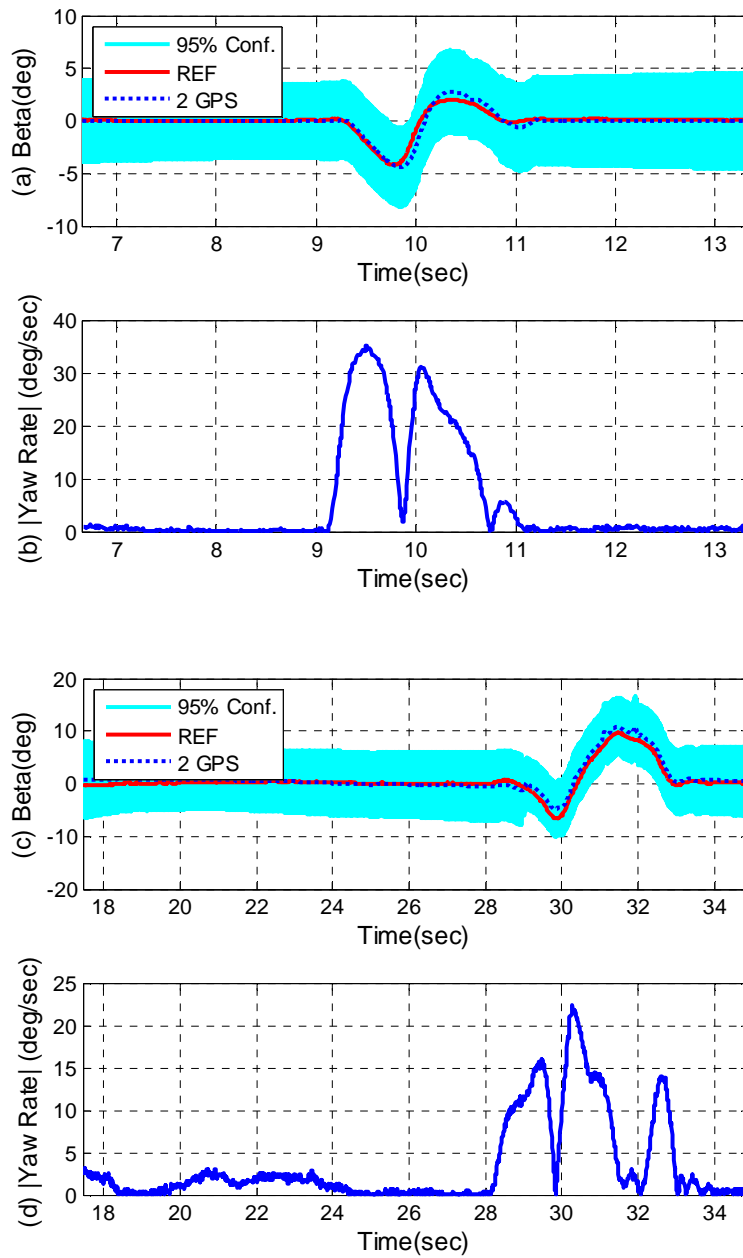


Figure 4.18 Sideslip estimation performance with single lane change on (a) asphalt and (c) wet tile surfaces. (b) and (d) are absolute values of corresponding yaw rates

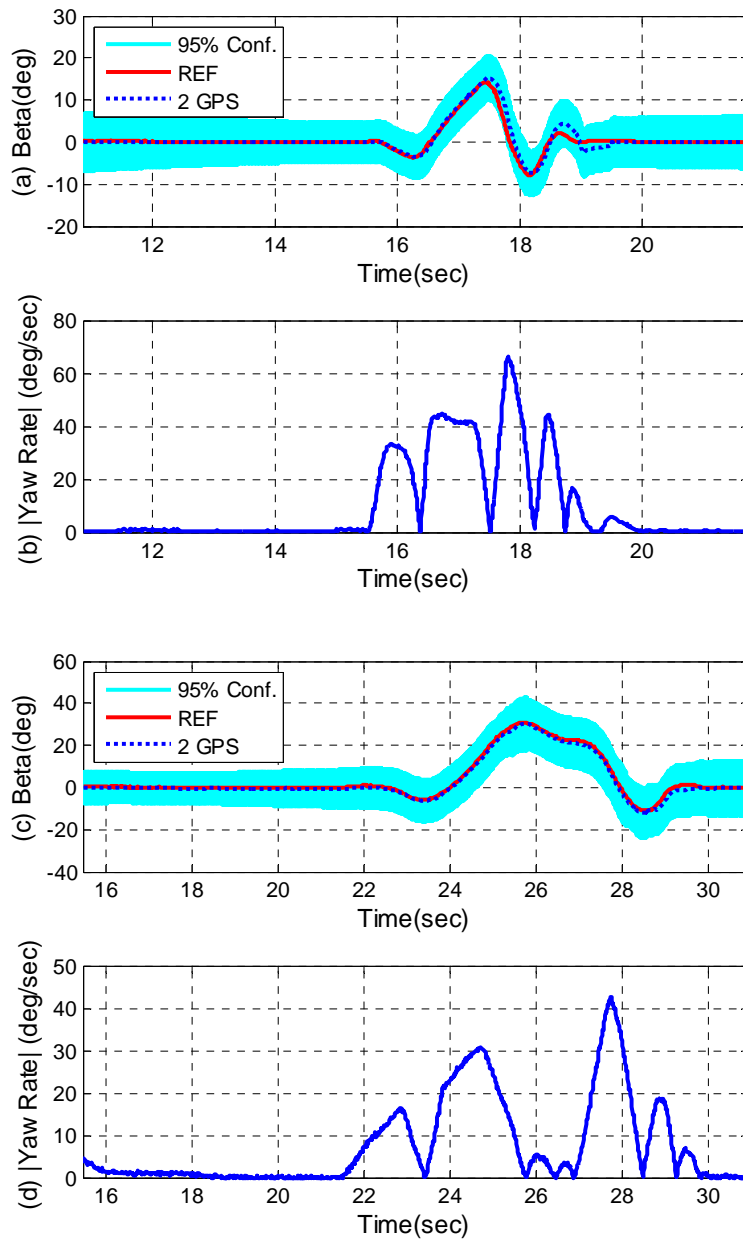


Figure 4.19 Sideslip estimation performance with double lane change on (a) asphalt and (c) wet tile surfaces. (b) and (d) are absolute values of corresponding yaw rates



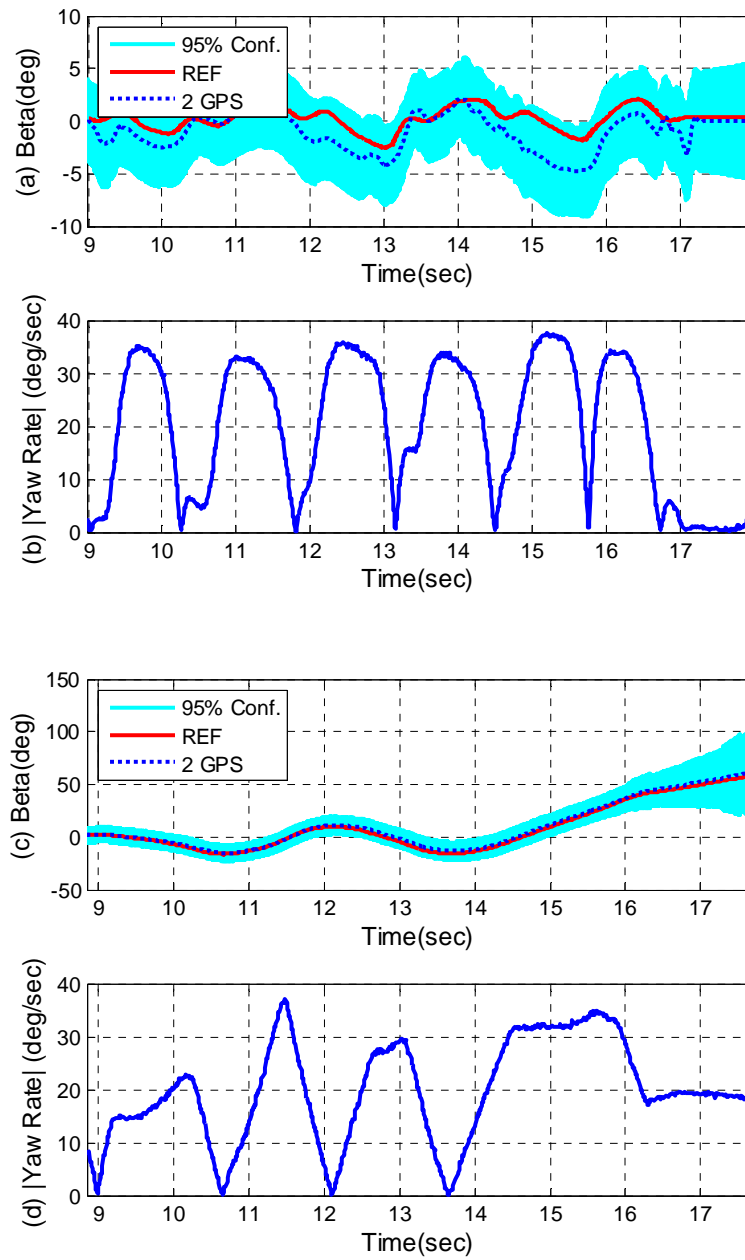


Figure 4.20 Sideslip estimation performance with slalom on (a) asphalt and (c) wet tile surfaces. (b) and (d) are absolute values of corresponding yaw rates

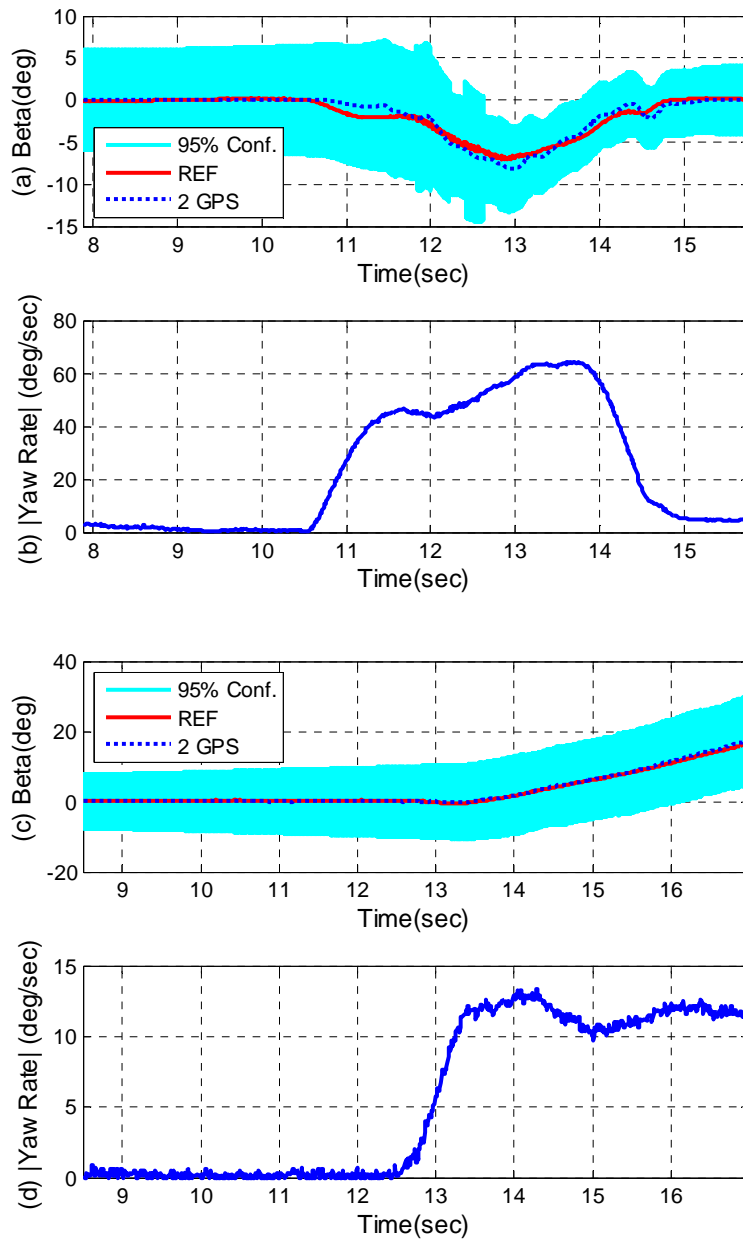


Figure 4.21 Sideslip estimation performance with J-turn on (a) asphalt and (c) wet tile surfaces. (b) and (d) are absolute values of corresponding yaw rates

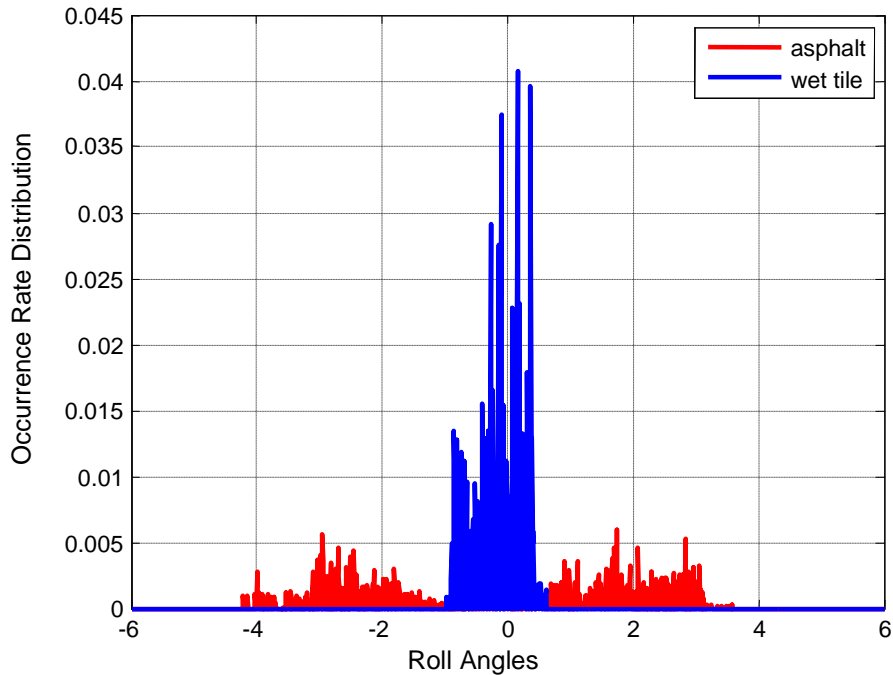


Figure 4.22 Distribution of roll angles during slalom

#### 4.6 Discussion

Horizontal velocities from two GPS receivers were processed to calculate vehicle yaw angles and sideslip angles. Those measurements were merged with IMU signals including longitudinal/lateral acceleration and yaw rate to compensate for the low update rate of the GPS. The Kalman filter technique was used for sensor fusion. Two challenges arise during sensor fusion; (1) delay in GPS signals and (2) unsynchronized updates between the two GPS receivers. Delays in GPS signals are handled through the ‘measurement shift’ technique and unsynchronized GPS updates are addressed by ‘asynchronous update’ technique. The observability analysis reveals that the vehicle sideslip angle is observable only when the vehicle yaw rate is adequately large. If the vehicle yaw rate is not large enough, the bicycle model is employed for the sideslip angle estimation. Several J-turn maneuvers on low frictional surface were conducted as a pilot test and proved the feasibility of the proposed method. To assess the performance in general, experiments were extended to include maneuvers of single lane changes, double

lane changes, slaloms, and J-turns. Three different surface friction levels were employed and the RMS error is  $2.6^\circ$ .

This method is assessed against the requirements stated in Section 1.3. Two GPS receivers used in this study cost \$400 (\$200 each). The exact price information of the IMU sensor is not available because it is embedded in a production ESC system. However, by considering general market price of ESC systems the IMU price should be in \$10 range. Therefore total integration cost is lower than \$450 which satisfies the low-cost requirement. The price information of the GPS receiver (\$200) was for the enclosed development kit. If just GPS receiver and a core chip are used, the price will be lower.

Vehicle parameters such as tire cornering stiffness, mass, and moment of inertia do not influence the estimation performance of the method. It is because the proposed method basically relies on kinematics of GPS velocity and IMU measurement. Even though the bicycle model which requires the vehicle parameters was employed during straight driving, it was shown that the bicycle model does not need accurate vehicle parameters during straight driving. Therefore robustness requirement #1 is satisfied. The robustness requirement #2 is also met in the sense that the sideslip angle estimation errors stay bounded with four different maneuvers on two difference frictional surfaces. However, this method fails to meet the accuracy requirement (RMS error of  $1.5^\circ$ ). This is partly due to significant delays in GPS signals, but mainly due to the incapacity of the method to compensate for the gravity component introduced by vehicle roll motions.

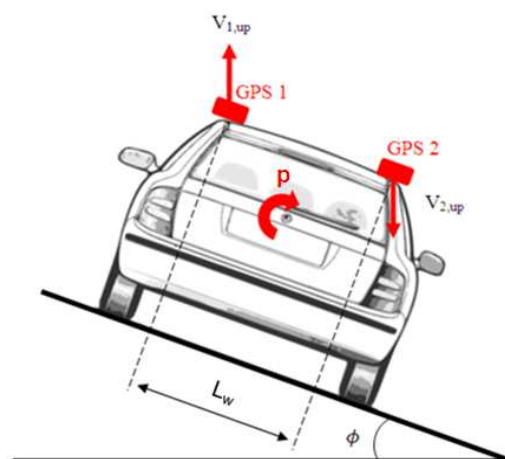


Figure 4.23 Rear view of a vehicle on a banked road

To meet the robustness requirement #3, vertical velocities of two GPS receivers were investigated for vehicle roll angle estimation. Figure 4.23 shows a rear view of a vehicle on a banked road whose banked angle is  $\phi$ . Two GPS receivers are horizontally aligned with distance of  $L_w$  apart. If the vehicle has roll rate ( $p$ ), vertical velocities of two GPS receivers are related with the bank angle as

$$V_{1,up} - V_{2,up} = L_w p \cos \phi \quad (4.26)$$

Equation (4.26) states that the roll angle can be calculated by using vertical velocity measurements as long as the vehicle keeps rolling. This is a highly unrealistic condition. Therefore the proposed method cannot measure vehicle roll angles; hence the sideslip estimation will be inaccurate when a vehicle runs on banked surfaces. Consequently the robustness requirement #3 is not satisfied by the proposed method.

## CHAPTER 5

# MERGING GPS AND IMU WITH A MAGNETOMETER

### 5.1 Introduction

Most current sideslip angle estimation methods including the method presented in CHAPTER 4 assume planar vehicle motions [6-22, 24, 50, 63-67]. Consequently the estimation accuracy is degraded if a vehicle runs on banked roads.

Several bank angle estimation methods have been proposed. In 2001 Tseng [68] proposed a novel method which could estimate a road bank angle during a dynamic maneuver. He identified that the main challenge lay in differentiating the road bank angle effect from the derivative of the lateral velocity. By introducing a dynamic factor that is an indicator of lateral velocity derivative, he devised a method for bank angle estimation. However, biases in lateral accelerometer were not considered. Hahn [69-70] utilized GPS for real-time bank angle estimation. He designed a disturbance observer based on the bicycle model. In his work, the sideslip angle was the key measurement. A position-based multiple-antennae GPS method was employed for sideslip angle measurement in his work. Ryu [71] used GPS to estimate the road bank angle and vehicle roll separately. His work was based on the bicycle model and a disturbance observer that was designed by state augmentation. In his work, the sideslip angle measurement was required and he used the heading-based multiple-antennae GPS method to estimate it. All the aforementioned methods inherit the drawbacks of dynamic model-based methods because they are based on the bicycle model. Additionally, the methods which employ position-/heading-based multiple-antennae GPS methods are cost prohibitive.

The author proposes to combine measurements of GPS and IMU with a magnetometer as a solution. A magnetometer is a sensor that measures the local magnetic field. The outputs of the magnetometer are three-dimensional components of the local magnetic field. If the Earth's magnetic field is dominant around the sensor, the

magnetometer measurement contains angles between the longitudinal axis of the vehicle and the magnetic North. Gebre-Egziabher showed the feasibility of using a magnetometer in yaw angle calculation. With fine sensor calibration, he could achieve about 3 deg accuracy [1]. Crassidis used a magnetometer to solve the carrier-cycle integer ambiguity problem of the Carrier-phase Differential GPS (CDGPS) described in Section 2.1[72]. Borges utilized a magnetometer to determine the yaw, pitch, and roll angles [73]. However his method assumed that gravity is the predominant force exerted on the accelerometer. Therefore this method is not applicable to ground vehicle applications because severe inertial forces are applied to the accelerometer.

None of the works described above has addressed the disturbance concern of a magnetometer. The Earth's magnetic field is only about 0.3~0.6 Gauss. This field is weak enough to be disturbed by a passing vehicle[74]. For the same reason, Abbott questioned the usefulness of the magnetometer for ground vehicle applications [75]. Therefore, proper handling of the magnetic disturbance is the key to success when using a magnetometer.

This chapter will discuss how to robustly extract vehicle heading information from magnetometer measurements by effectively rejecting disturbances. To achieve that, a new stochastic filter is introduced. Then measurements from GPS, IMU and a magnetometer are merged on the Kalman filter framework to estimate the vehicle sideslip angle. Simulation and experimental results are provided to verify the performance of the proposed method.

## **5.2 Heading Angles from a Magnetometer**

The Earth's magnetic field originates from the inner core of the Earth and envelopes the Earth as seen in the Figure 5.1. The Earth has a crust, a mantle, and a metallic core. While most of the core is liquid, the inner part is solid. Complex processes are associated with the increase of the inner core together with the Earth's rotation drive, which is believed to cause the Earth's magnetic field [76]. The magnetic North wanders slow enough that a compass is useful for navigation.

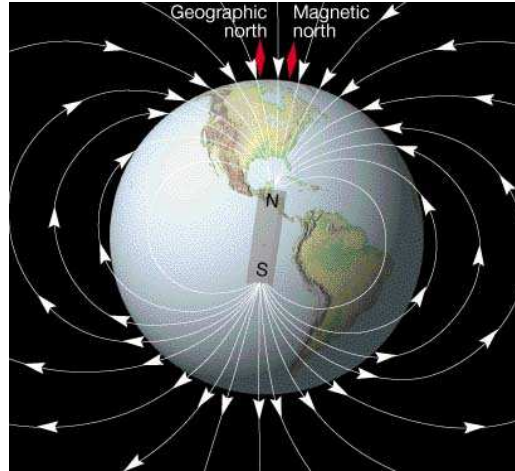


Figure 5.1 The Earth's magnetic field

Figure 5.2 shows four coordinate frames employed in this study. The frame with the subscript 'G' represents the geographic Earth-fixed frame (G-frame).  $X_G$  and  $Y_G$  point to the geographic North and West, respectively. The frame of a subscript 'M' is another Earth-fixed frame (M-frame), whose X-axis ( $X_M$ ) points to the magnetic North. The frame with the subscript of 'v' is a moving frame attached to the vehicle (v-frame) and the frame of the subscript 's' is for a moving frame attached to the magnetometer (s-frame). Each frame is related to another through yaw-pitch-roll angles. In the figure, roll and pitch angles are omitted for succinctness.

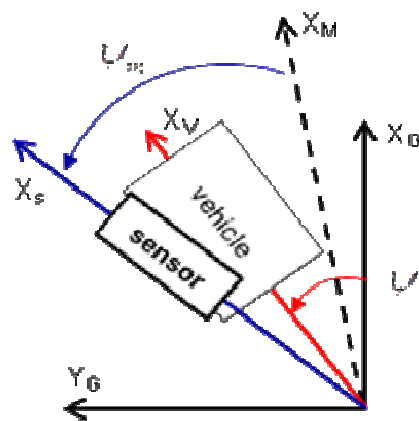


Figure 5.2 Top view of four coordinate frames



At a given spot on the Earth, the Earth's magnetic field would have X and Z components in the M-frame. As a magnetometer measures the Earth's magnetic field in the s-frame, the magnetometer measurement can be expressed as (5.1). The ZYX Euler angle definition is used.  $(\psi_m, \theta_m, \phi_m)$  are Euler angles of the magnetometer with respect to the M-frame.

To obtain the vehicle Euler angles  $(\psi, \theta, \phi)$  with respect to the G-frame,  $(\psi_m, \theta_m, \phi_m)$  are replaced with  $(\psi + \psi_o, \theta + \theta_o, \phi + \phi_o)$ . Subscript 'o' means constant offsets. For the yaw angle, the offset is a combination of a magnetometer mounting error and tilt of the magnetic North pole. For pitch and roll angles, offsets are purely from magnetometer mounting errors. These offsets values are known through calibration.

$$\begin{bmatrix} m_x \\ m_y \\ m_z \end{bmatrix} = \begin{bmatrix} \cos \psi_m \cos \theta_m & \sin \psi_m \cos \theta_m & -\sin \theta_m \\ -\sin \psi_m \cos \phi_m & \cos \psi_m \cos \phi_m & \cos \theta_m \sin \phi_m \\ +\cos \psi_m \sin \theta_m \sin \phi_m & +\sin \psi_m \sin \theta_m \sin \phi_m & \\ \sin \psi_m \sin \phi_m & -\cos \psi_m \sin \phi_m & \cos \theta_m \cos \phi_m \\ +\cos \psi_m \sin \theta_m \cos \phi_m & +\sin \psi_m \sin \theta_m \cos \phi_m & \end{bmatrix} \begin{bmatrix} M_x \\ M_y \\ M_z \end{bmatrix} \quad (5.1)$$

where

- $[m_x \ m_y \ m_z]^T$  The Earth's magnetic field measured in the s-frame
- $[M_x \ M_y \ M_z]^T$  The Earth's magnetic field measured in the M-frame
- $[\psi_m \ \theta_m \ \phi_m]$  Yaw, pitch, and roll angles of the magnetometer with respect to the M-frame

To determine the Euler angles  $(\psi, \theta, \phi)$  of a three-dimensional object, at least two independent directional vectors are required. This is explained in Figure 5.3. Given only one directional vector, infinite numbers of different attitudes are possible. Figure 5.3 shows only two of them. For the same reason, solving (5.1) would produce numerous redundant combinations of  $(\psi_m, \theta_m, \phi_m)$ .

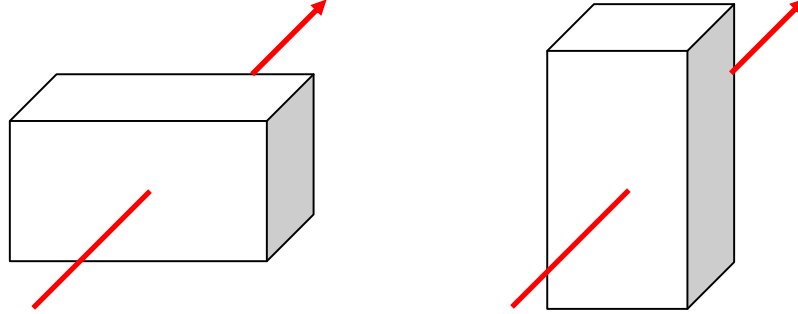


Figure 5.3 Two different attitudes with one given reference vector

To resolve this redundancy, the vehicle pitch angle is assumed to be negligible. Since ground vehicles are our research interest, this assumption is sensible. Consequently, (5.1) is converted to (5.2). The pitch offset ( $\theta_o$ ) is still in the equation to correct the sensor mounting error.  $M_y$  is not present because it is zero.

$$\begin{bmatrix} m_x \\ m_y \\ m_z \end{bmatrix} = \begin{bmatrix} M_x \cos \psi_m - M_z \theta_o \\ -M_x \sin \psi_m \cos \phi_m + M_x \theta_o \cos \psi_m \sin \phi_m + M_z \sin \phi_m \\ M_x \sin \psi_m \sin \phi_m + M_x \theta_o \cos \psi_m \cos \phi_m + M_z \cos \phi_m \end{bmatrix} \quad (5.2)$$

### 5.3 Stochastic Filter to Reject Magnetic Field Disturbances

As Abbott warned, the Earth's magnetic field is so weak that its measurement can be easily disturbed [75]. Accordingly, disturbance rejection is the key to the success of using the magnetometer. In this section, disturbance rejection is discussed from two aspects: (1) how to detect disturbances and (2) how to estimate states with disturbed measurements.

#### 5.3.1 Magnetic Disturbance Detection

Several magnetometer data profiles were collected on a highway (I-96 Michigan), while a vehicle was driven straight. By using (5.2), the vehicle yaw angle was calculated

from magnetometer measurements and those are seen in Figure 5.4 (red lines). The vehicle was driven fairly straight. Therefore significant yaw angle deviations in the figure were caused by magnetic disturbances which were induced by passing-by vehicles. The blue lines of Figure 5.4 are the norm of the magnetic field measurements ( $= \sqrt{m_x^2 + m_y^2 + m_z^2}$ ). When the magnetic disturbance occurs, the norm of the magnetic field also deviates from unity.

To confirm the correlation, all the highway data are processed to yield Figure 5.5. This figure is a correlation graph between the absolute value of yaw angle errors and deviations of the magnetic norm from unity. The correlation coefficient is 0.9, which suggests a strong correlation. Therefore, it can be stated that disturbances in the magnetometer measurements can be detected by monitoring the magnetic field norm deviation.

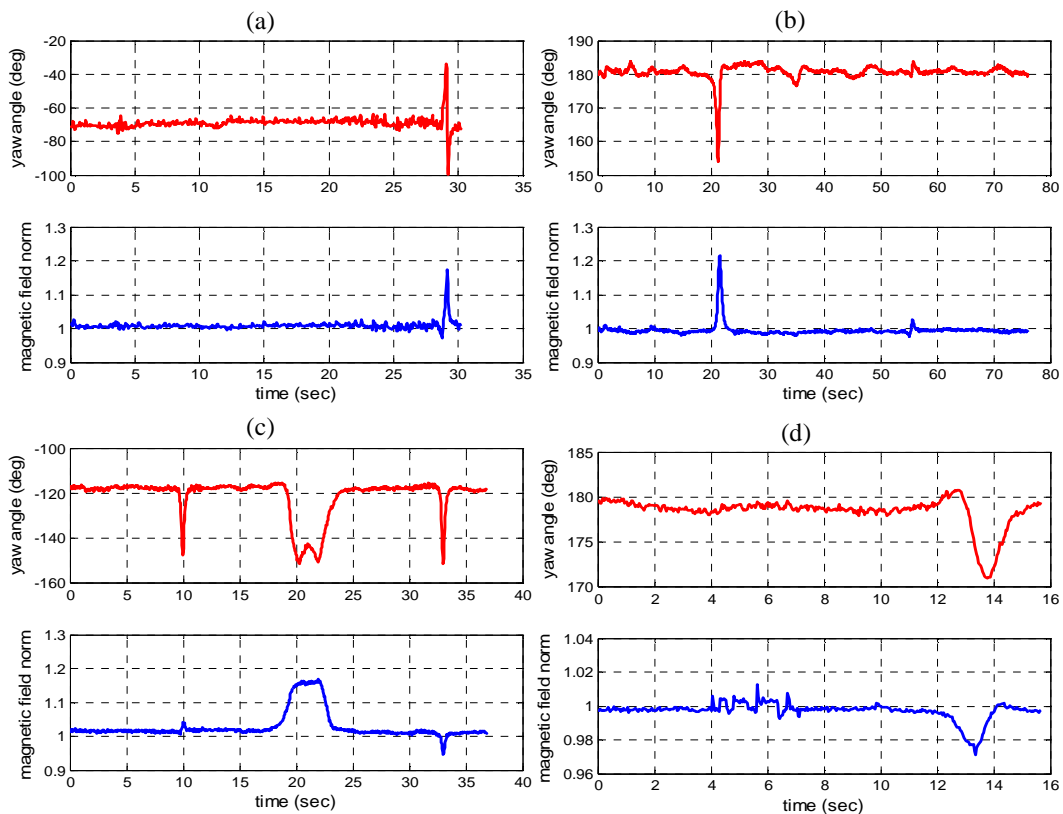


Figure 5.4 Highway data. Magnetic fields are measured when vehicle runs straight. A magnetometer provides the magnetic field measurements in normalized unit.

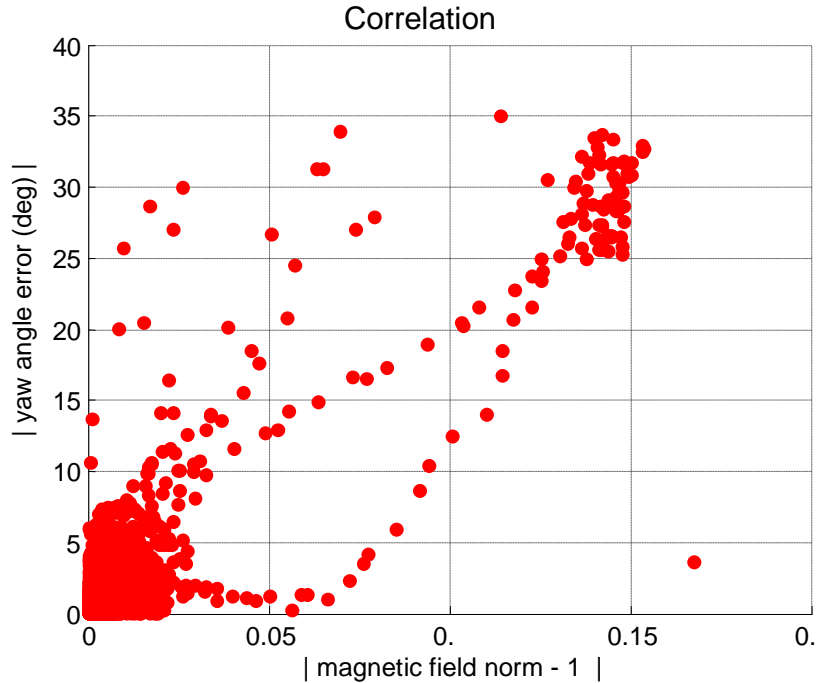


Figure 5.5 A correlation plot between yaw angle error and deviation of magnetic field norm from unity. The yaw angle is calculated from magnetometer measurements only.

### 5.3.2 State Estimation with Disturbed Measurements

#### 5.3.2.1 Stochastic Characterization of Magnetic Disturbance

Figure 5.6 is the enlarged view of Figure 5.4 (b). The area in gray represents when the magnetic field is disturbed. Random variable  $W$  represents the amount of heading error due to the disturbance. The absolute value of  $W$  is upper limited by a selected value  $b_0$ .  $W$  depends on the magnetic strength of a disturbance source and the distance between the magnetometer and the source. However, when the presence of the disturbance is detected, prior knowledge of  $W$  may not be easily available. Therefore, it is reasonable to assume that the random variable  $W$  is described by the uniform probability density function (PDF) as seen in Figure 5.7. Barmish justified the use of the uniform distribution when statistical information about the uncertain disturbance is unavailable [77]. Other researchers have adopted the same approach to handle disturbances [78-79].

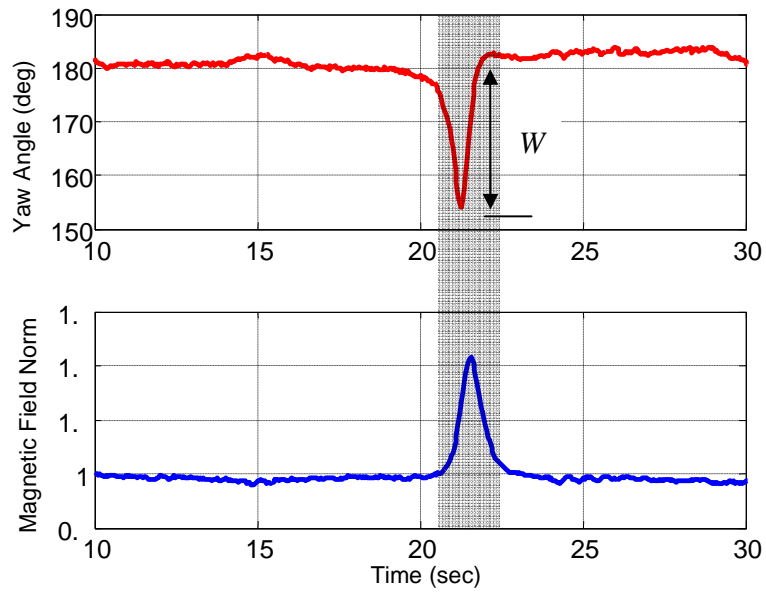


Figure 5.6 Enlarged view of Figure 5.4 (b).  $W$  is the heading angle error induced by magnetic disturbances.

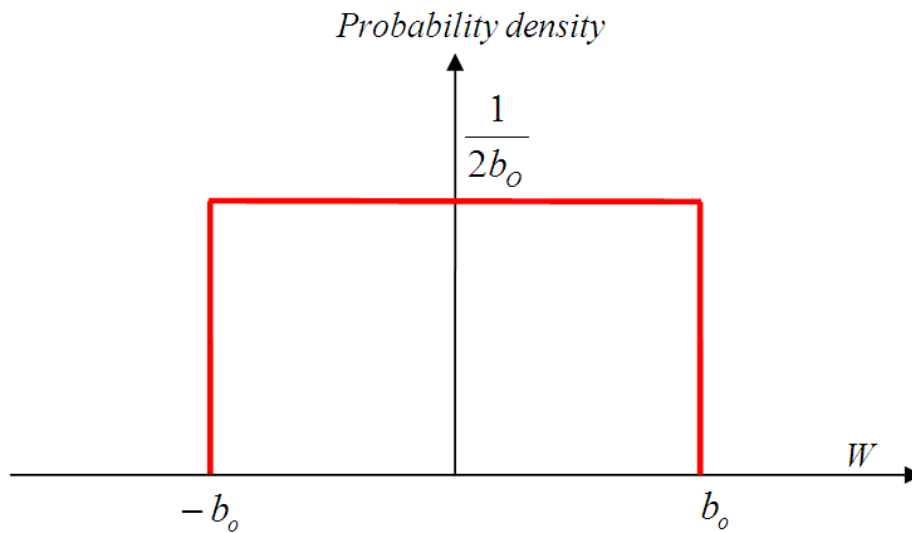


Figure 5.7 The uniform distribution to describe the heading angle errors induced by magnetic disturbances

### 5.3.2.2 Optimal State Estimation under Disturbance: Scalar Case

Let two random variables  $x$  and  $z$  be related via a joint probability density function  $f_{x,z}(x,z)$ . For any given measurement ( $z$ ), the optimal estimation of  $x$  minimizing  $\varepsilon[(x - \hat{x})^2]$  is

$$\hat{x} = \mathcal{E}(x|z) = \int_{-\infty}^{\infty} x \frac{f_{x,z}(x,z)}{f_z(z)} dx \quad (5.3)$$

This is known as the minimum mean square error (MMSE) estimation. If the two random variables  $x$  and  $z$  have the normal distributions, the optimal estimation ( $\hat{x}$ ) is a linear function of the measurement ( $z$ ). However, for our case, the disturbed measurement ( $z$ ) is assumed to be described by a uniform distribution, whereas the state ( $x$ ) is described by a normal distribution:

$$\begin{aligned} x &= N(\mu_x, \sigma) \\ z &= cx + U(-b_o, b_o) \end{aligned} \quad (5.4)$$

where  $N$  and  $U$  represent the normal and uniform distributions respectively and  $\mu_x, \sigma, c$  and  $b_o$  are constants characterizing the probability density functions. Then the MMSE estimation is

$$\hat{x} = \int_{(z-b_o)/c}^{(z+b_o)/c} \left[ \frac{x e^{\left(-\frac{1}{2} \left(\frac{x-\mu_x}{\sigma}\right)^2\right)}}{\int_{(z-b_o)/c}^{(z+b_o)/c} e^{\left(-\frac{1}{2} \left(\frac{s-\mu_x}{\sigma}\right)^2\right)} ds} \right] dx \quad (5.5)$$

For detailed derivation, the reader is referred to Appendix C of this thesis. According to (5.5), the optimal state estimation would have a nonlinear relationship with the measurement when the measurement is contaminated by disturbances. Since nonlinearity is hard to handle, the author applied a simple technique.

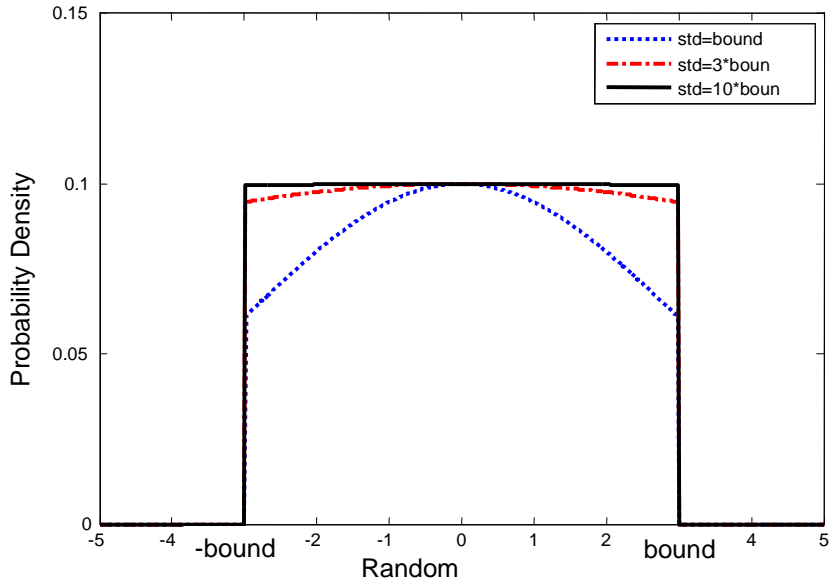


Figure 5.8 Truncated normal distributions with three different standard deviations. The truncated normal distribution whose standard deviation is ten times larger than the bound greatly resembles the uniform distribution.

Figure 5.8 shows the truncated normal distributions with three different standard deviations. As can be seen, if the standard deviation is large enough compared to the truncated bound, the truncated normal distribution would have the similar shape as the uniform distribution. Hence, the author replaced the uniform distribution of (5.4) with the truncated normal distribution and the bivariate model is changed to

$$\begin{aligned}
 x &= N(\mu_x, \sigma_x) \\
 z &= \begin{cases} \frac{\sigma_z}{\rho\sigma_x} x + N(0, \sigma_z) & \text{if } \left| z - \frac{\sigma_z}{\rho\sigma_x} x \right| \leq z_b \\ 0 & \text{otherwise} \end{cases} \quad (5.6)
 \end{aligned}$$

where  $\sigma_x$  and  $\sigma_z$  are standard deviations of the random variable  $x$  and  $z$ , and  $\rho (= \frac{\sigma_{xz}}{\sigma_x\sigma_z})$  is the correlation coefficient.  $z_b$  is the truncated bound of random variable  $z$ .

Without loss of generality, the mean value of the random variable  $x$  ( $= \mu_x$ ) can be shifted to the origin. Then the joint PDF, MMSE estimation and the variance of the joint distribution are presented in Table 5.1. Detailed derivations are presented in Appendix D.

It is worth emphasizing that (5.8) and (5.9) are identical to those of the bivariate normal distribution except for the modification factor ( $m$ ) in (5.9) where  $m$  is always positive. In other words, if a bivariate normal distribution has standard deviations of  $\sigma_x\sqrt{m}$  and  $\sigma_z\sqrt{m}$  respectively, its MMSE estimation and corresponding variance would be the same as (5.8) and (5.9). As mean and variance are enough to define a bivariate normal distribution [49], this suggests that the bivariate normal-truncated normal distribution can be replaced by the bivariate normal distribution with modified standard deviations.

**Table 5.1 Stochastic properties of the joint normal-truncated normal distribution**

---

**PDF**  $f_{X,Z}(x, z) =$

$$\begin{cases} A \exp\left(-\frac{1}{2(1-\rho^2)}\left[\left(\frac{x}{\sigma_x}\right)^2 - 2\rho\left(\frac{x}{\sigma_x}\right)\left(\frac{z}{\sigma_z}\right) + \left(\frac{z}{\sigma_z}\right)^2\right]\right) & \text{if } \left|z - \frac{\sigma_z}{\rho\sigma_x}x\right| \leq z_b \\ 0 & \text{otherwise} \end{cases} \quad (5.7)$$

where  $A = \frac{1}{2\pi\sigma_x\sigma_z\sqrt{1-\rho^2}}\left[\Phi\left(\frac{x_b}{\sigma_x\sqrt{1-\rho^2}}\right) - \Phi\left(\frac{-x_b}{\sigma_x\sqrt{1-\rho^2}}\right)\right]$

$\Phi(x) = \int_{-\infty}^x \frac{1}{\sqrt{2\pi}} e^{-\frac{t^2}{2}} dt$ ,  $x_b = \rho \frac{\sigma_x}{\sigma_z} z_b$ ,

---

**MMSE**  $\hat{x} = \varepsilon(x|z) =$

$$\rho \frac{\sigma_x}{\sigma_z} z \quad (5.8)$$

---

**Variance**  $\iint_{-\infty}^{\infty} (z - \hat{z})^2 f_{X,Z}(x, z) dx dz =$

$$\sigma_z^2 (1 - \rho^2) m \quad (5.9)$$

where



$$m = \left( \frac{1}{\Phi\left(\frac{z_b}{\sigma_z\sqrt{1-\rho^2}}\right) - \Phi\left(-\frac{z_b}{\sigma_z\sqrt{1-\rho^2}}\right)} + \frac{2\frac{z_b}{\sigma_z\sqrt{1-\rho^2}}\varphi\left(\frac{z_b}{\sigma_z\sqrt{1-\rho^2}}\right)}{\left(\Phi\left(\frac{z_b}{\sigma_z\sqrt{1-\rho^2}}\right) - \Phi\left(-\frac{z_b}{\sigma_z\sqrt{1-\rho^2}}\right)\right)^2} \right)$$

$$\hat{z} = \frac{\sigma_z}{\rho\sigma_x} \hat{x}, \quad \varphi(x) = \frac{1}{\sqrt{2\pi}} e^{-\frac{1}{2}x^2}$$


---

### 5.3.2.3 Optimal State Estimation under Disturbance: Vector Case

Recall the system and measurement equations of (3.4) - (3.5) and rewrite them as

$$x_k = \Phi_{k-1}x_{k-1} + \Gamma_{k-1}u_{k-1} + \Lambda_{k-1} \begin{pmatrix} w_{1,k-1} \\ w_{2,k-1} \\ \vdots \\ w_{l_w,k-1} \end{pmatrix} = \bar{x}_k + \begin{pmatrix} w'_{1,k-1} \\ w'_{2,k-1} \\ \vdots \\ w'_{l_w,k-1} \end{pmatrix} \quad (5.10)$$

$$\begin{pmatrix} z_{1,k} \\ z_{2,k} \\ \vdots \\ z_{m,k} \end{pmatrix} = \begin{pmatrix} h_{11,k} & h_{12,k} & \cdots & h_{1n,k} \\ h_{21,k} & h_{22,k} & \cdots & h_{2n,k} \\ \vdots & \vdots & \vdots & \vdots \\ h_{m1,k} & h_{m2,k} & \cdots & h_{mn,k} \end{pmatrix} \begin{pmatrix} x_{1,k} \\ x_{2,k} \\ \vdots \\ x_{n,k} \end{pmatrix} + \begin{pmatrix} v_{1,k} \\ v_{2,k} \\ \vdots \\ v_{m,k} \end{pmatrix} \quad (5.11)$$

where state  $x_k \in R^{n \times 1}$ , input  $u_{k-1} \in R^{l_u \times 1}$ , system transition matrix  $\Phi_{k-1} \in R^{n \times n}$ ,  $\Gamma_{k-1} \in R^{n \times l_u}$  and  $\Lambda_{k-1} \in R^{n \times l_w}$ . In (5.10), let  $(\Phi_{k-1}x_{k-1} + \Gamma_{k-1}u_{k-1})$  be  $\bar{x}_k$  and the state error vector  $(w'_{1,k-1} \cdots w'_{l_w,k-1})^T$  is defined by  $\Lambda_{k-1}(w_{1,k-1} \cdots w_{l_w,k-1})^T$ . We assume that  $(w_{1,k-1}, \dots, w_{l_w,k-1})$  of (5.10) are normally distributed. Subsequently  $(w'_{1,k-1}, \dots, w'_{l_w,k-1})$  are also normally distributed because a linear combination of normally distributed random variables has a normal distribution (Appendix E). Therefore each component of the state  $x_k$  is normally distributed around the corresponding component of  $\bar{x}_k$  in (5.10).

In (5.11), the  $i^{\text{th}}$  measurement is expressed as

$$z_{i,k} = h_{i1,k}x_{1,k} + h_{i2,k}x_{2,k} + \cdots + h_{in,k}x_{n,k} + v_{i,k} \quad (5.12)$$

Since  $x_{1,k}, \dots, x_{n,k}$  are normally distributed, their linear combination ( $h_{i1,k}x_{1,k} + \dots + h_{in,k}x_{n,k}$ ) is also normally distributed (Appendix E). Let the linear combination of ( $h_{i1,k}x_{1,k} + \dots + h_{in,k}x_{n,k}$ ) be the scalar  $x_{G,k}$ , then

$$\begin{aligned} x_{G,k} &= N(\bar{x}_{G,k}, \sigma_G) \\ z_{i,k} &= x_{G,k} + v_{i,k} \end{aligned} \quad (5.13)$$

where  $\bar{x}_{G,k}$  is the same linear combination composed of components of  $\bar{x}_k$ . If the  $i^{\text{th}}$  measurement is disturbed,  $v_{i,k}$  has a uniform distribution and can be replaced by  $U(-b_o, b_o)$  where  $b_o$  is the possible maximum bound of the disturbance. All terms in (5.13) are scalars, therefore (5.13) has the exactly same format as (5.4). According to the lessons from 5.3.2.2, (5.13) is converted into

$$\begin{aligned} x_{G,k} &= N(\bar{x}_{G,k}, \sigma_G \sqrt{m}) \\ z_{i,k} &= x_{G,k} + N(0, \sigma_z \sqrt{m}) \end{aligned} \quad (5.14)$$

where  $\sigma_z$  is set to be greater than at least ten times of  $b_o$  and  $m$  is calculated by (5.9). The factor  $\sqrt{m}$  is commonly applied to the standard deviations of state and measurement. Accordingly,  $\sqrt{m}$  is cancelled out during the calculation of the optimal state estimation as seen in (5.8). Therefore, (5.15) yields the same state estimation as (5.14).

$$\begin{aligned} x_{G,k} &= N(\bar{x}_{G,k}, \sigma_G) \\ z_{i,k} &= x_{G,k} + N(0, \sigma_z) \end{aligned} \quad (5.15)$$

This result is important because  $x_{G,k}$  of (5.15) is identical to (5.13). Only the distribution of  $z_{i,k}$  is changed. This means that if a measurement is disturbed, it can be treated as a normal distribution whose standard deviation is  $\sigma_z$ . Therefore the Kalman filter process (3.6)-(3.10) can be utilized even when measurements are disturbed. It is

important to understand  $\sigma_z$  is not a statistical property. Instead, it is set to make the truncated distribution mimic the uniform distribution.  $\sigma_z$  is supposed to be much larger than the truncated bound of disturbances. Let  $\sigma_{z,noise}$  be the standard deviation of the undisturbed measurement error, then

$$\sigma_z = \sigma_{z,noise} \eta_i \quad (5.16)$$

The measurement error covariance matrix ( $R_k$ ) in (3.8) is calculated by  $\mathcal{E}\{v_k v_k^T\}$ . If the  $i^{\text{th}}$  measurement is disturbed,  $R_k$  will become

$$R_k = \begin{pmatrix} \sigma_{1,k,noise}^2 & & & \\ & \ddots & & \\ & & \sigma_{i,k,noise}^2 & \\ & & & \ddots \\ & & & & \sigma_{m,k,noise}^2 \end{pmatrix} \begin{pmatrix} 1 & & & \\ & \ddots & & \\ & & \eta_{i,k}^2 & \\ & & & \ddots \\ & & & & 1 \end{pmatrix} = R_{k,noise} M \quad (5.17)$$

If measurements are not disturbed, the modification matrix ( $M$  in(5.17)) is the identity matrix. Otherwise,  $\eta$  of the disturbed measurement component is calculated by (5.16).

### 5.4 Sensor Fusion through the Kalman Filter

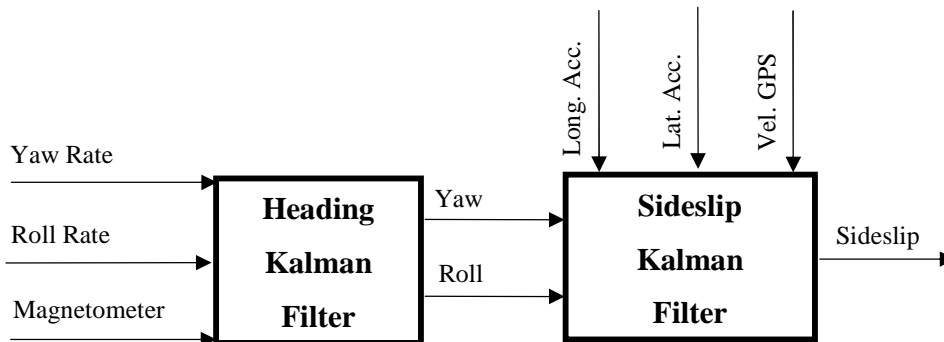


Figure 5.9 Schematic diagram of the dual Kalman filters

Figure 5.9 shows the schematic overview of two Kalman filters in series that estimate the vehicle sideslip angle. The Heading Kalman filter yields yaw and roll angles by processing angular rate measurements of the IMU and magnetic field measurements. Then the vehicle sideslip is calculated through the Sideslip Kalman filter by combining vehicle velocities measured by a single GPS receiver and vehicle accelerations from an IMU.

#### 5.4.1 Heading Kalman Filter

For the time update equation, the kinematics of angular rates and angles are employed as

$$\begin{bmatrix} \dot{\psi} \\ \dot{\phi} \end{bmatrix} = \begin{bmatrix} 0 & 0 \\ 0 & 0 \end{bmatrix} \begin{bmatrix} \psi \\ \phi \end{bmatrix} + \begin{bmatrix} r_m - b_r \\ p_m - b_p \end{bmatrix} + noise$$

where

$$\begin{bmatrix} r_m & p_m \end{bmatrix} \quad \text{yaw rate and roll rate measurements} \quad (5.18)$$

$$\begin{bmatrix} b_r & b_p \end{bmatrix} \quad \text{biases in yaw rate and roll rate measurements}$$

*noise*      the Gaussian white noise

The pitch angle is not included as a state due to the zero pitch assumption. The author does not attempt to estimate yaw rate and roll rate biases in real-time because they are easily calculated during vehicle standstill.

The magnetometer is used for the measurement update. Since it is highly nonlinear, the Extended Kalman filter is employed. Therefore (3.14) is calculated with  $(\hat{\psi}_k^-, \hat{\phi}_k^-)$  and (3.16) is used where  $(\hat{\psi}_k^-, \hat{\phi}_k^-)$  are the predicted state estimates through the time update. As the Heading Kalman filter relies on the magnetometer measurement, it is highly susceptible to large disturbances. Lessons learned from the Section 5.3 are applied here; hence the measurement error covariance matrix has the modification matrix as (5.17) if measurements are disturbed.

### 5.4.2 Sideslip Kalman Filter

In the ISO coordinate system, the kinematics relating accelerations and velocities are

$$\begin{aligned}
 a_{x,m} &= \dot{U} - \dot{\psi}V + b_x + w_x \\
 a_{y,m} &= \dot{V} + \dot{\psi}U + b_y + g \sin \phi + w_y
 \end{aligned}$$

where

$$\begin{aligned}
 \begin{bmatrix} a_{x,m} & a_{y,m} \end{bmatrix} & \text{longitudinal/lateral acceleration measurements} \\
 \begin{bmatrix} U & V \end{bmatrix} & \text{longitudinal/lateral velocities} \\
 \begin{bmatrix} b_x & b_y \end{bmatrix} & \text{biases in } \begin{bmatrix} a_{x,m} & a_{y,m} \end{bmatrix} \\
 g \sin \phi & \text{gravitational component by roll and road bank angle} \\
 \begin{bmatrix} w_x & w_y \end{bmatrix} & \text{the Gaussian white noise}
 \end{aligned} \tag{5.19}$$

As the yaw rate ( $\dot{\psi}$ ) is obtained by subtracting the yaw rate bias from the yaw rate measurements, (5.19) is rearranged to form the time update equation as

$$\begin{bmatrix} \dot{U} \\ \dot{b}_x \\ \dot{V} \\ \dot{b}_y \end{bmatrix} = \begin{bmatrix} 0 & -1 & \dot{\psi} & 0 \\ 0 & 0 & 0 & 0 \\ -\dot{\psi} & 0 & 0 & -1 \\ 0 & 0 & 0 & 0 \end{bmatrix} \begin{bmatrix} U \\ b_x \\ V \\ b_y \end{bmatrix} + \begin{bmatrix} 1 & 0 \\ 0 & 0 \\ 0 & 1 \\ 0 & 0 \end{bmatrix} \begin{bmatrix} a_{x,m} \\ a_{y,m} - g \sin \phi \end{bmatrix} + noise \tag{5.20}$$

Accelerometer bias estimation is a challenging task in today's ESC product. It is mainly due to the difficulty in road bank estimation. As the proposed method is capable of estimating vehicle roll angles including road bank angles, accelerometer bias is expected to be accurately estimated. This is why biases of accelerometers are augmented into the states to be estimated in (5.20).

A single antenna GPS provides the vehicle velocity in the G-frame. Since the vehicle heading is known from the Heading Kalman filter, vehicle velocity measurement by the GPS in the G-frame can be converted into longitudinal, lateral and vertical velocities via

$$\begin{bmatrix} U^{GPS} \\ V^{GPS} \\ V_{ver}^{GPS} \end{bmatrix} = \begin{bmatrix} \cos \psi & \sin \psi & 0 \\ -\cos \phi \sin \psi & \cos \phi \cos \psi & \sin \phi \\ \sin \phi \sin \psi & -\sin \phi \cos \psi & \cos \phi \end{bmatrix} \begin{bmatrix} V_N^{GPS} \\ V_W^{GPS} \\ V_U^{GPS} \end{bmatrix}$$

where

$$\begin{bmatrix} V_N^{GPS} & V_W^{GPS} & V_U^{GPS} \end{bmatrix} \text{ GPS velocities in the G-frame} \quad (5.21)$$

[North, West, Upward]

$$\begin{bmatrix} U^{GPS} & V^{GPS} & V_{ver}^{GPS} \end{bmatrix} \text{ GPS velocities in the v-frame}$$

Therefore, when GPS velocity measurements are available, the measurement update equations are

$$\begin{bmatrix} U^{GPS} \\ V^{GPS} \end{bmatrix} = \begin{bmatrix} 1 & 0 & 0 & 0 \\ 0 & 0 & 1 & 0 \end{bmatrix} \begin{bmatrix} U \\ b_x \\ V \\ b_y \end{bmatrix} + noise \quad (5.22)$$

Once estimations of longitudinal and lateral velocities are obtained, the sideslip angle is given by

$$\hat{\beta} = \tan^{-1} \left( \frac{\hat{V}}{\hat{U}} \right) \quad (5.23)$$

where  $\hat{\beta}$ ,  $\hat{U}$ , and  $\hat{V}$  are estimations of the sideslip angle, longitudinal velocity, and lateral velocity by the Sideslip Kalman filter. GPS receivers are known to have significant delays, especially for low-cost units. This delay is handled by the measurement shift technique described in Section 3.3.1.

## 5.5 Observability Analysis

Theories presented in Section 3.2 are applied to the Heading and Sideslip Kalman filters for the stochastic observability analysis. Since this is a time-varying system, the observability is dependent on trajectories of the state. Therefore the author followed procedures below.

- Choose a maneuver
- Choose an integer  $N$  of (3.20)
- Build  $O(k, k - N)$  and  $C(k, k - N)$  of (3.18) and (3.19)
- Evaluate  $\alpha_o, \beta_o, \alpha_c,$  and  $\beta_c$  of (3.18) and (3.19)

Since  $P_0$  is set to be positive definite, this system is stochastically observable as long as all of  $\alpha_o, \beta_o, \alpha_c,$  and  $\beta_c$  are positive according to (3.23). The author selected maneuvers of single lane change (SLC), double lane change (DLC), slalom (SLL), and J-turn.  $N$  of 1, 2, and 3 are analyzed.

### 5.5.1 Heading Kalman Filter Analysis

The plant and measurement equations are described in (5.18) and (5.2), respectively. Since (5.2) is nonlinear, the Jacobian is used for the observability analysis. Figure 5.10 shows  $\alpha_o, \beta_o, \alpha_c,$  and  $\beta_c$  of the Heading Kalman filter of the selected maneuver. Regardless of  $N$ , they are all positive except for  $\alpha_o$ . To investigate further,  $\alpha_o$  is plotted along with the yaw rate absolute value (Figure 5.11). The yaw rate is generated through maneuvers of SLC, DLC, SLL, and J-turn.  $\alpha_o$  shows clear dependency on yaw rates and it is positive only when the vehicle turns. In other words, vehicle heading angles (yaw and roll) are observable by the Kalman filter of (5.18) and (5.2) when the vehicle turns. Otherwise, the observability is not guaranteed.

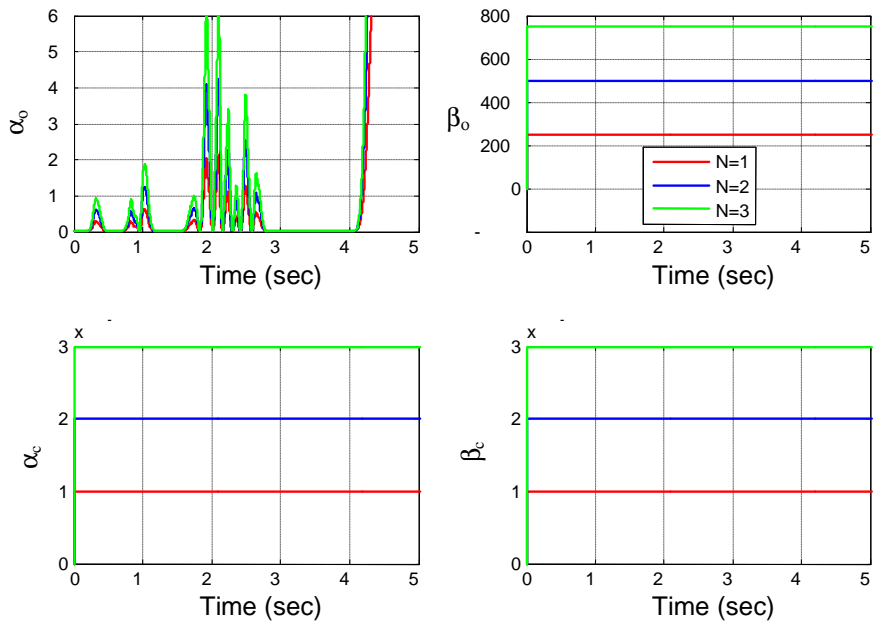


Figure 5.10  $\alpha_o$ ,  $\beta_o$ ,  $\alpha_c$ , and  $\beta_c$  of the Heading Kalman filter

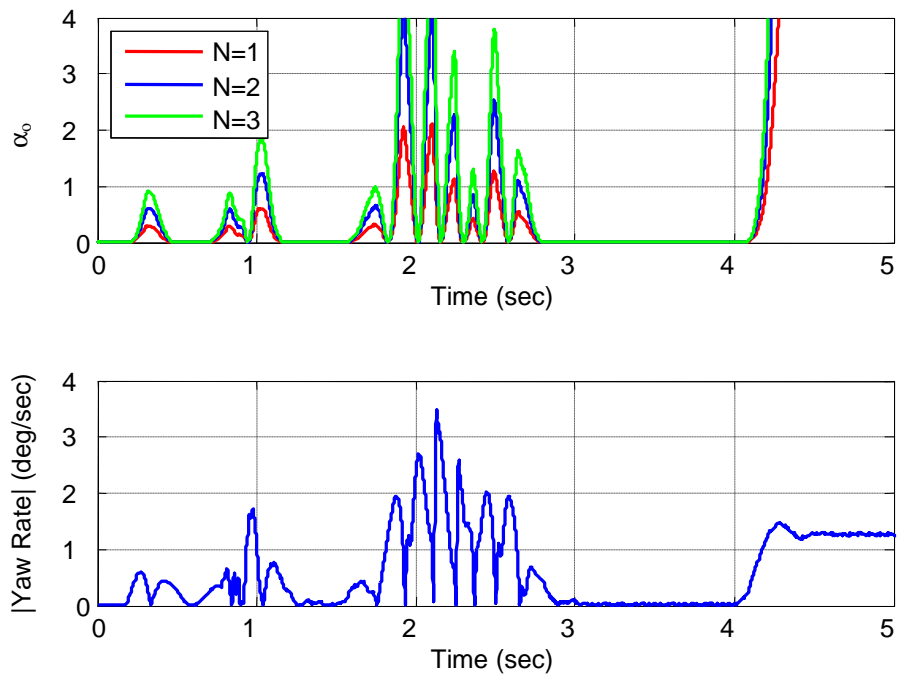


Figure 5.11  $\alpha_o$  and the absolute value of yaw rate



### 5.5.2 Sideslip Kalman Filter Analysis

Equation (5.20) and (5.22) are employed for the Sideslip Kalman filter observability analysis and Figure 5.12 shows  $\alpha_o$ ,  $\beta_o$ ,  $\alpha_c$ , and  $\beta_c$  of the Sideslip Kalman filter.

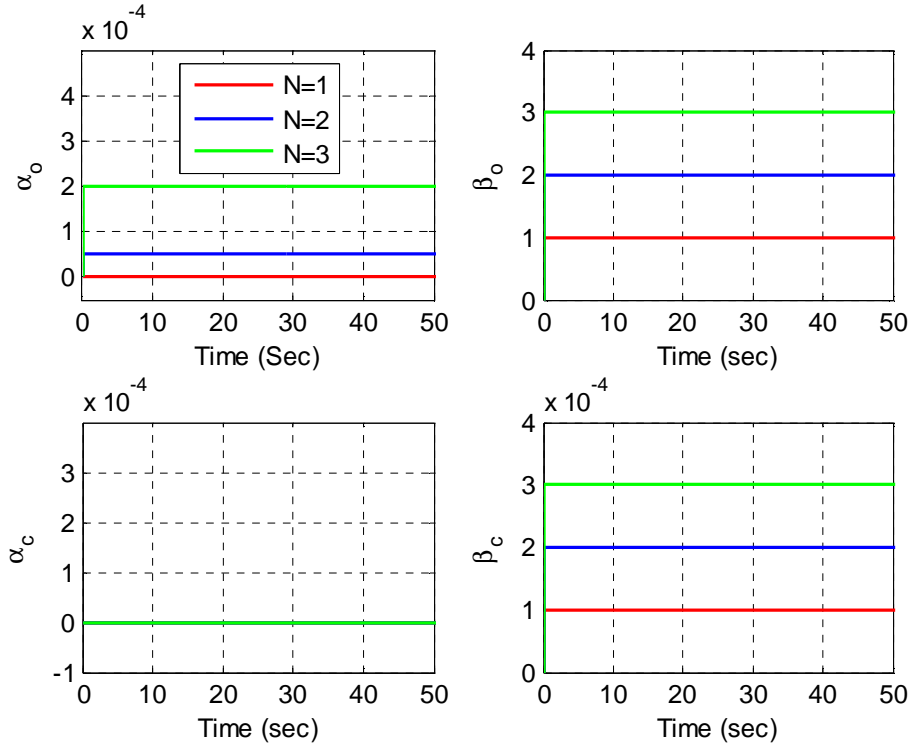


Figure 5.12  $\alpha_o$ ,  $\beta_o$ ,  $\alpha_c$ , and  $\beta_c$  of the Sideslip Kalman filter

Regardless of N, all the values are positive except for  $\alpha_c$ , which is a constant zero. Hence, the stochastic observability is not guaranteed according to (3.23) because the system is not uniformly completely controllable.

The immediate root-cause is two empty rows (2<sup>nd</sup> and 4<sup>th</sup> rows) in system matrices of (5.20). This occurs due to state augmentation with the sensor biases. The biases in the longitudinal and lateral accelerometers ( $b_x$  and  $b_y$ ) are removed from (5.20). Then  $\alpha_o$ ,  $\beta_o$ ,  $\alpha_c$ , and  $\beta_c$  are changed as seen in Figure 5.13. As all the values are positive, the stochastic observability is guaranteed if the sensor biases do not augment the state. Therefore if the sensor biases are estimated by a separate method rather than state

augmentation, the corresponding Sideslip Kalman filter will be stochastically observable. This will be discussed in the future work section.

By augmenting the state with the accelerometer biases, the stochastic observability condition is violated. However, this does not necessarily mean that the system is unobservable because the stochastic observability condition is a sufficient condition. In fact, the simulation and experimental result of the following section show that all the states are estimated even with the augmented state. Therefore the author uses the state augmentation to estimate the sensor biases as seen in (5.20).

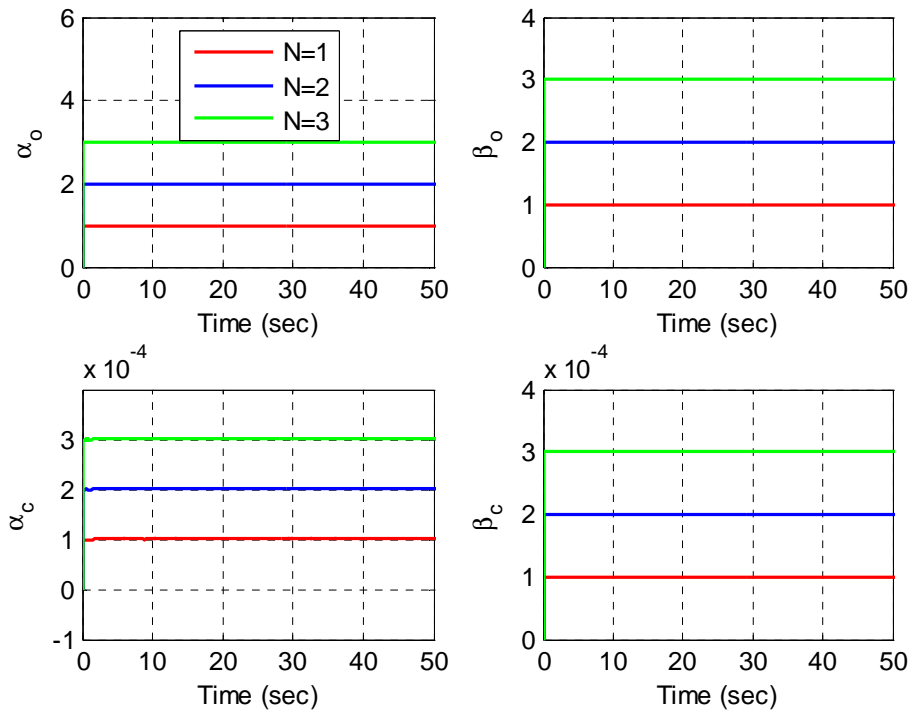


Figure 5.13  $\alpha_o, \beta_o, \alpha_c,$  and  $\beta_c$  of the Sideslip Kalman filter after removing the longitudinal/lateral biases from the state

### 5.5.3 Bicycle Model

The stochastic observability analysis of the Heading Kalman filter reveals that the vehicle heading angles (yaw and roll) are not guaranteed to be observable when the vehicle moves straight. When the author processed the experimental data, this loss of the

observability was seen. The author relies on the bicycle model during straight driving because it can estimate vehicle sideslip accurately when the vehicle does not turn as seen in Section 4.4.4. Nominal vehicle parameters are used and the vehicle is considered to move straight if the absolute value of the steering consistently stays below  $20^\circ$ .

## 5.6 Simulations and Experimental Results

### 5.6.1 Simulations

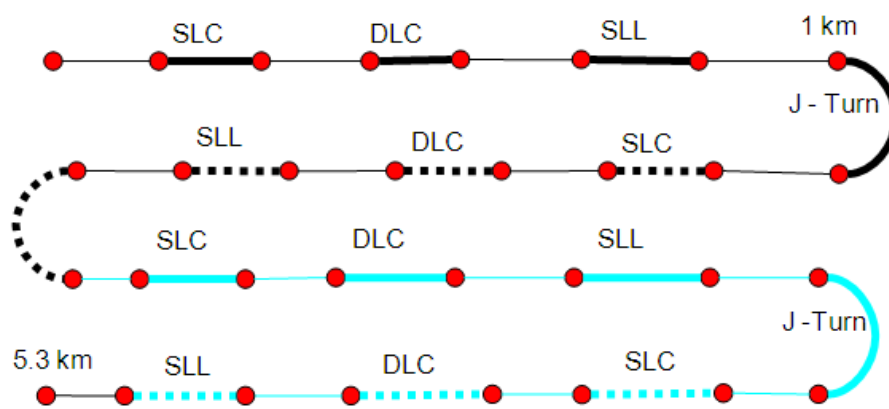


Figure 5.14 The layout of the simulating ‘test track’

Comprehensive simulations were run using the Carsim<sup>TM</sup>, which is a proven tool for vehicle dynamics simulations and analyses. To cover various driving conditions, four types of maneuvers are combined with two friction types and two road bank types as listed in Table 5.2. Figure 5.14 shows the simulation layout. Black lines represent asphalt and cyan lines icy surfaces. Friction coefficient of 0.8 is used for the asphalt and 0.3 is used for the icy surfaces. Solid lines are flat surfaces while dotted lines are banked surfaces. The road bank angle is 15 % for the asphalt road, and 10 % for the icy surfaces. The total length of the road is 5.3 km. Vehicle speed and steering angles are properly manipulated to (1) generate considerable slips and (2) keep the vehicle from spin-out. For realistic simulations, various error sources are injected including biases in IMU, delay in GPS and random disturbances in a magnetometer as presented in Table 5.2.

Table 5.2 Simulation properties

<b>Simulation Properties</b>	
Maneuver Type	Single Lane Change (SLC) Double Lane Change (DLC) Slalom (SLL) J-turn
Frictional Coefficient	0.8 for asphalt 0.3 for ice
Road Bank Type	0 deg for flat 5.71 deg (10%) for banked ice 8.53 deg (15%) for banked asphalt
Vehicle Type	Small size passenger car
<b>Injected Error Properties</b>	
IMU	Standard Deviation of White Noise 0.01 m/s <sup>2</sup> for acceleration 0.1 deg/s for rate gyros Injected Bias 0.5 m/s <sup>2</sup> for acceleration 2.0 deg/s for rate gyros
GPS	Standard Deviation of White Noise 0.01m/s Delay 400 ms
Magnetometer	Standard Deviation of White Noise 0.02 Disturbances 24 occurrences at random timing with random magnitude in [0.5, 2.0]

Figure 5.15 (a) shows deviations of the magnetic field norm from unity. Several peaks in the figure indicate simulated disturbances in the magnetic field. Figure 5.15 (b) and (c) show that yaw and roll angles are accurately estimated even though the magnetic field measurements are intermittently disturbed. The yaw angle RMS error is  $0.60^\circ$  and roll angle RMS error is  $0.22^\circ$ .

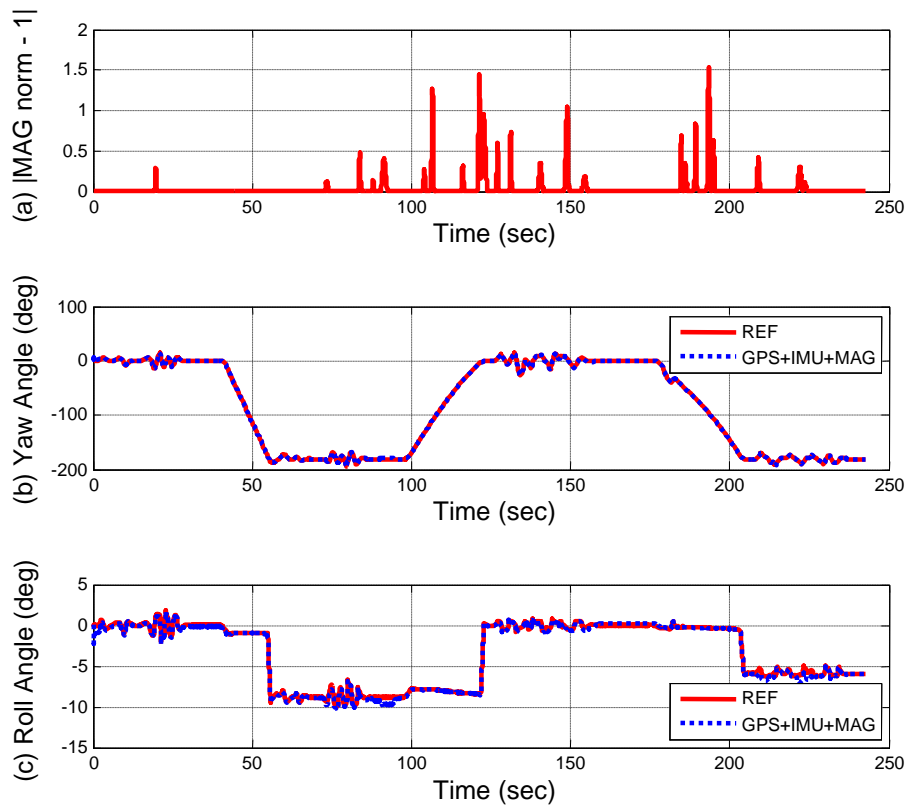


Figure 5.15 Simulation results; (a) deviation of magnetic field norm due to injected disturbances, (b) yaw angle estimation, and (c) roll angle estimation.

Sideslip angle estimation performance of four selected road segments is presented in Figure 5.16. The first 10 seconds of Figure 5.16 (a) shows considerable errors due to initialization. However, once initialization is completed, sideslip angle estimation stays close to the true values. Figure 5.16 (a) and (c) confirm that the proposed method can yield an accurate sideslip angle estimation at two considerably different surface frictions. Figure 5.16 (b) and (d) demonstrate that the method works even when the vehicle is on banked roads.

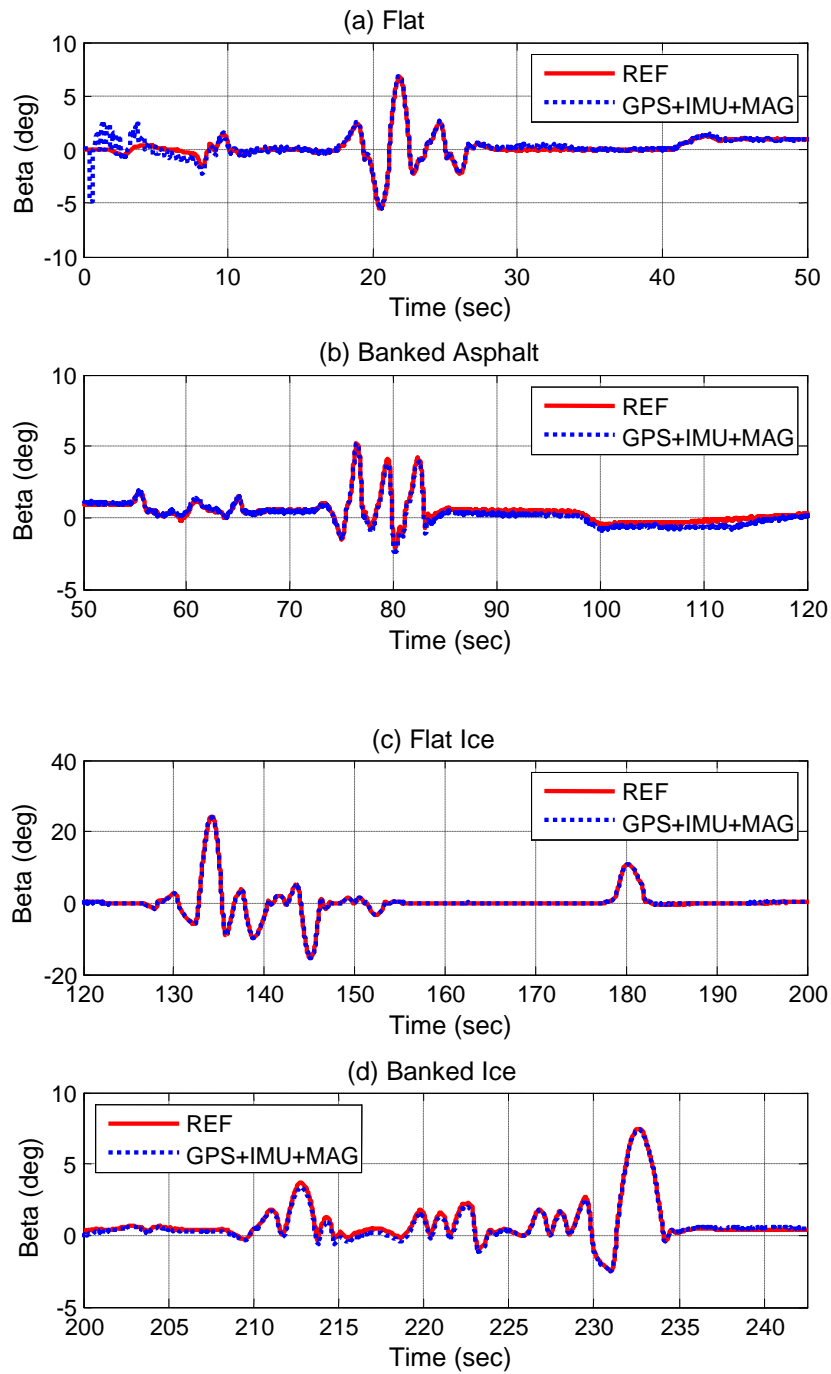


Figure 5.16 The sideslip angle estimation performance on different friction and road bank levels; (a) flat asphalt, (b) banked asphalt, (c) flat ice, and (d) banked ice.

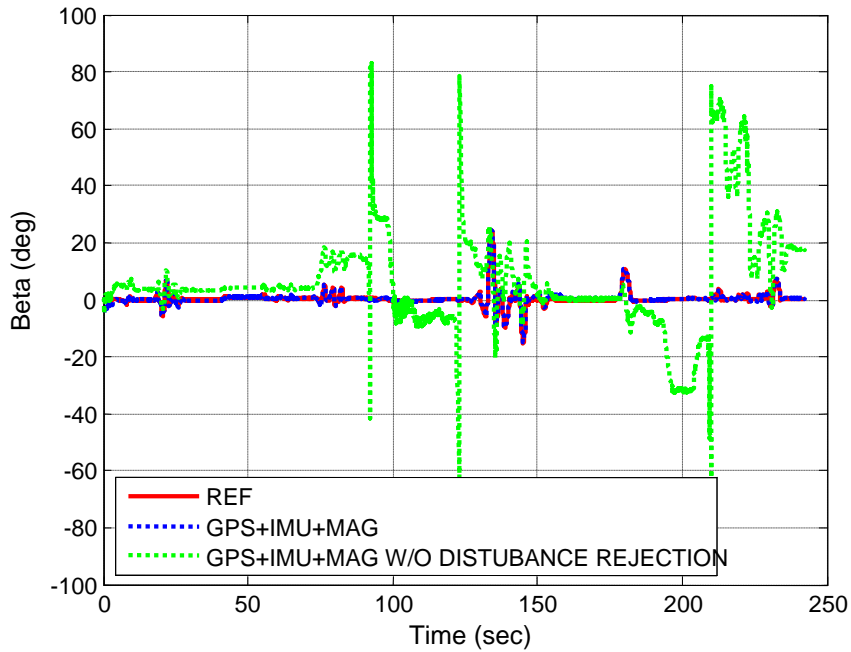


Figure 5.17 The sideslip angle estimation performance with and without magnetic disturbance rejection logic.

Figure 5.17 is the vehicle sideslip estimation plot. The sideslip RMS error is  $0.68^\circ$ . The green dotted line is the estimation outcome without the magnetic disturbance rejection logic. Superior accuracy of the blue dotted line to the green dotted line demonstrates that magnetic disturbances are successfully rejected by the proposed method.

Biases in longitudinal and lateral accelerometers are estimated through the state augmentation as seen (5.20). Unlike biases in the rate gyro, accelerometer bias estimation is more challenging because the gravity component on a banked road has the same effect on the accelerometer as do the biases. To obtain the genuine sensor bias, the bank influence must be removed. However, using today's on-board sensors accurate road bank angle estimations are difficult. As the proposed method accurately estimates road bank angles, accelerometer biases can be accurately calculated. For the verification,  $0.5 \text{ m/s}^2$  offsets are injected in the accelerometer measurements and offsets of  $8 \text{ m/s}^2$  are injected later for extreme case simulation. Four graphs in the Figure 5.18 show that the proposed method estimates the injected biases successfully. This is somewhat interesting result

because Section 5.4.2 shows that the stochastic observability of the Sideslip Kalman filter is not guaranteed due to the state augmentation with the sensor biases. Even though the condition for the stochastic observability is violated, the state still can be fully determined by measurements because the stochastic observability condition is a sufficient condition. Accurate state estimation performance seen in Figure 5.16 and Figure 5.18 indicates that the Sideslip Kalman filter is the case.

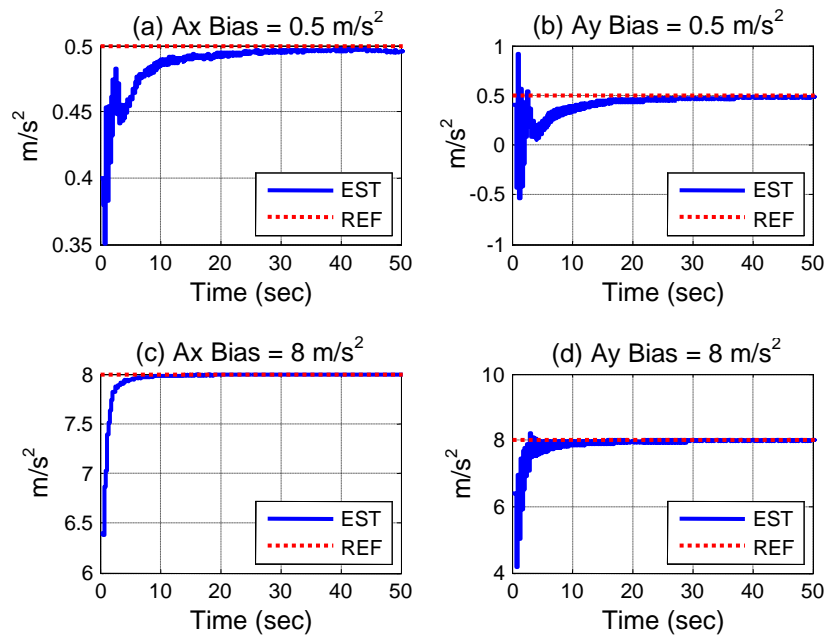


Figure 5.18 Accelerometer bias estimation performance

### 5.6.2 Experimental Verifications

Experimental verification was conducted in two different ways. One is to run pre-defined maneuvers on a test track, and the other is to drive the vehicle in a neighborhood area emulating daily driving. A GM Silverado truck was equipped with an Xsens MTi magnetometer, an IMU from a production ESC unit, and an Oxford RT2500 with a single GPS receiver (Figure 5.19). Xsens MTi is a heading angle reference system which combines measurement of IMU and magnetometer. However, we used only the magnetometer measurement portion of it. Under disturbance-free circumstances, the



measurement noise level ( $1\sigma$ ) of magnetometer is 0.5 milli-Gauss. Xsens MTi provides three dimensional magnetic field measurements in a normalized unit at 120 Hz update rate. The measurement noise level ( $1\sigma$ ) of the IMU is  $0.02 \text{ m/s}^2$  and  $0.08 \text{ deg/sec}$  for accelerometers and rate gyros, respectively. The IMU has an update rate of 166 Hz. Sideslip measurements provided by the RT2500 are treated as true values and will be called as “reference signals” hereinafter. Experimental verification uses the vehicle velocity measurement of RT2500 GPS at 100 Hz. However, to mimic the velocity signal of a low-cost GPS receiver, a 400 ms delay is injected. In addition, the data is down-sampled at 5 Hz.



Figure 5.19 The test vehicle (GM Silverado) with equipment. (Left) The GPS receivers is located on the roof of the vehicle, (Center) The Oxford RT2500 is installed in the vehicle, (Right) The magnetometer is installed on the rear of the vehicle.

#### 5.6.2.1 On-Track Experiments

Four types of maneuvers including single lane changes (SLC), double lane changes (DLC), slaloms (SLL) and J-turns were run on packed snow and ice surfaces at the TRW winter test track in Racó, Michigan. Two different vehicle speeds representing fast (90 KPH on snow, 50 KPH on ice) and slow (60 KPH on snow, 30 KPH on ice) were executed. J-turns were run on the packed snow surface only because ice and packed snow showed the same vehicle dynamic response with J-turn maneuver. Each driving scenario had 5 runs; a total of 70 data sets were collected. Figure 5.20 shows typical traces of experimental data where the red lines are reference signals from RT2500, blue dotted lines are estimations by the proposed method, and cyan blue envelopes are 95%

confidence ranges calculated from the state error covariance matrices. As seen in the figure, the sideslip estimation stays close to the reference signal. The sideslip RMS error from 70 collected runs is  $1.3^\circ$ . The J-turn trace shows estimation deviation at the end of the run because the J-turn results in significant vehicle speed reduction unlike other maneuvers. It is known that errors in sideslip estimation due to GPS noise grow as a vehicle speeds reduces [20].

Since the track had little magnetic disturbance, the aforementioned performance does not prove the robustness of the algorithm against magnetic disturbances. To verify the magnetic disturbance rejection algorithm, randomly generated disturbances are injected into the on-track data. The disturbance of  $[0.05,1]$  at 20% was added, which means that the norm of the randomly generated disturbance was between 0.05 and 1, and the disturbance was injected 20% of the time. This property is chosen to mimic actual disturbances based on collected highway data (Appendix F). With the injected disturbances, the sideslip RMS error from 70 data becomes  $1.98^\circ$ , which is about 50% higher than the magnetic disturbance-free data.

The impact of magnetic disturbance is studied further. A representative data of each maneuver (SLC, DLC, SLL and J-turn) is selected and the data is processed twenty times with randomly generated magnetic disturbances of various magnitude and occurrence rates. Figure 5.21 shows estimation performances with the magnetic disturbance of  $[0.05,1]$  at 20%. Blue lines are the sideslip estimations by the proposed method where green dotted lines are the estimation without the disturbance rejection algorithm. The results with disturbance rejection stay close to the reference signal and the results without disturbance rejection are much worse, demonstrating the robustness of the proposed method against magnetic disturbances. The sideslip RMS error from 80 runs (4 selected data  $\times$  20 runs) with the disturbance of  $[0.05,1]$  at 20% is  $1.28^\circ$ . Table 5.3 shows the sideslip RMS errors with different types of disturbance. When the occurrence rate is 20%, the disturbance has negligible effect. However, the RMS error increases to  $2.23^\circ$  with 40% occurrence rate, which is 75% worse than the disturbance-free performance.

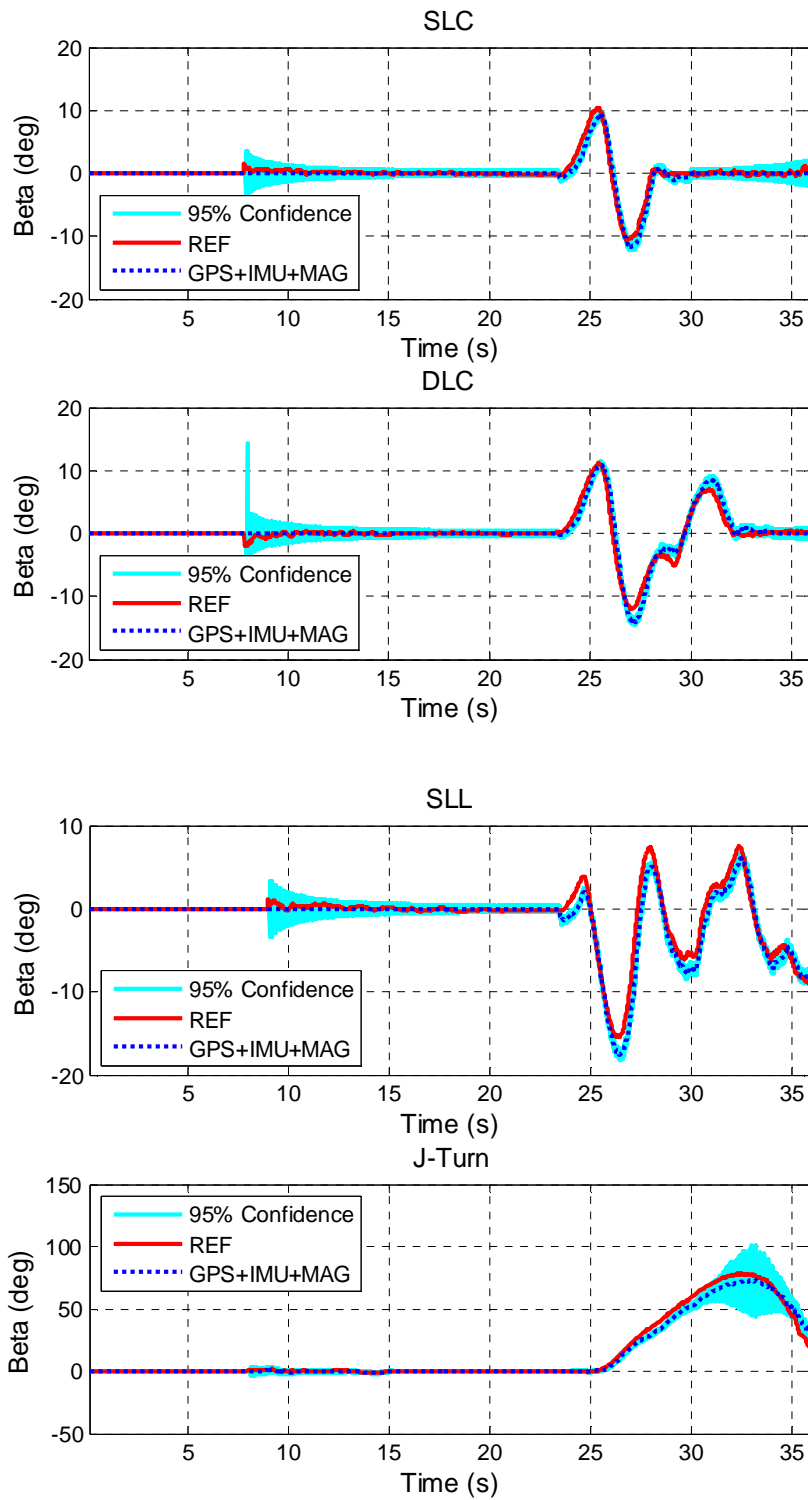


Figure 5.20 The sideslip estimation performance of on-track experiments; (a) single lane change (SLC), (b) double lane change (DLC), (c) slalom (SLL), and (d) J-turn

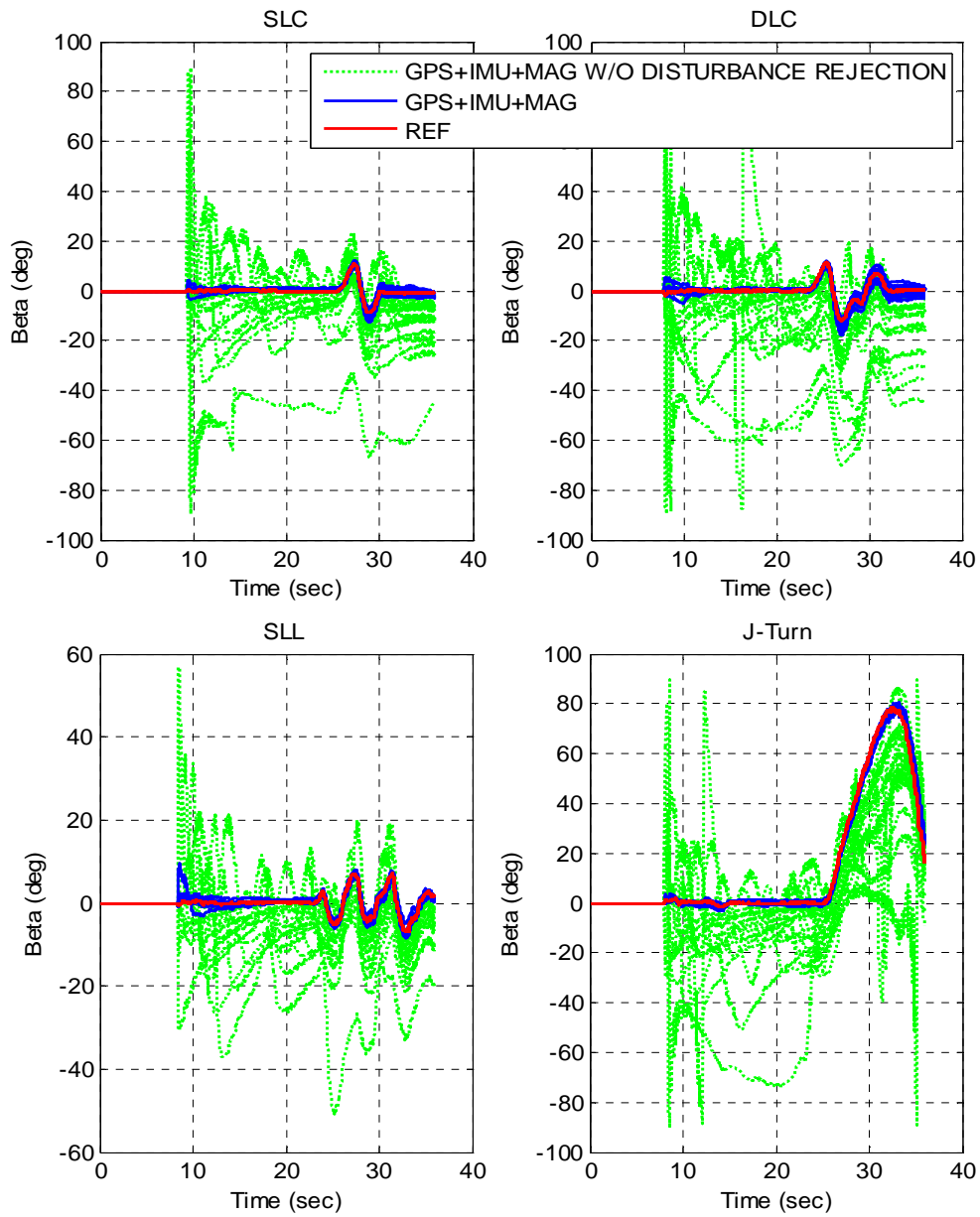


Figure 5.21 The sideslip estimation performance of on-track experiments of single lane change (SLC), double lane change (DLC), slalom (SLL) and J-turn with and without magnetic disturbance rejection. Results from 20 runs with disturbance of [0.05,1] at 20%.

Table 5.3 The performance with different disturbance levels

Disturbance Type	Sideslip RMS error
[0.01,0.015] at 20 %	1.05°
[0.05,1] at 20 %	1.28°
[1,2] at 20 %	1.22°
[0.05,1] at 40 %	2.23°

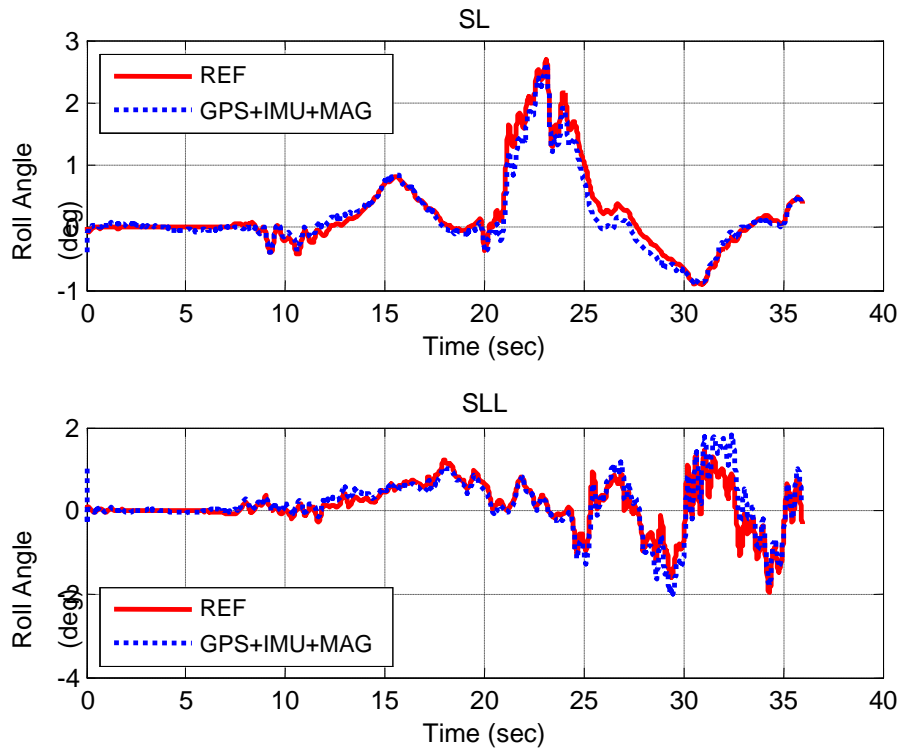


Figure 5.22 The roll angle estimation performance of on-track experiments; single lane change (SLC) and slalom (SLL)

Figure 5.22 shows traces of roll angle estimation. Since track surfaces were flat, the magnitude of vehicle roll angles were insignificant. The RMS error is  $0.43^\circ$ .

### 5.6.2.2 Neighborhood Area Experiments

The test vehicle was driven on neighborhood areas of Kinross, Michigan on February 25<sup>th</sup>, 2012. Figure 5.23 shows the top view of the area. On that day, all the roads were covered with packed snow. Magnetic disturbance sources, including passing vehicles, houses, and utility poles with electric transformers, were present in the area. A total of 9 data sets were collected and each run was 2 to 3 minutes long. Figure 5.24 shows an example trace of steering angle, yaw rate and vehicle speed to give an idea of the driving maneuvers. Several aggressive cornering maneuvers were tried to create considerable sideslip angles on snow covered roads.



Figure 5.23 Top view of the neighborhood area used for test (Kinross, Michigan)

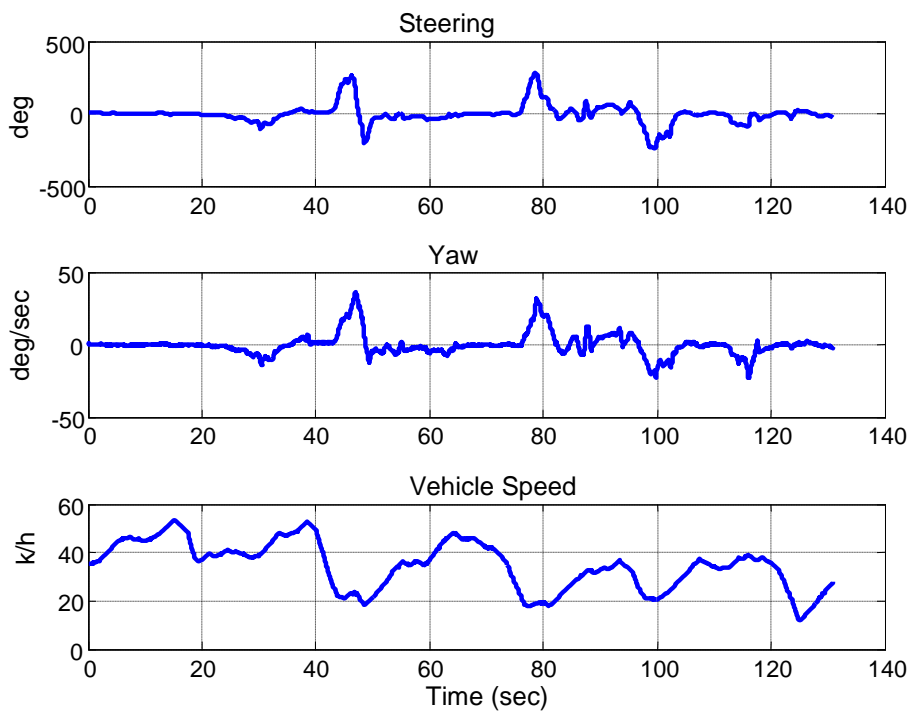


Figure 5.24 An example of steering angle, yaw rate, and vehicle speed during neighborhood area experiments.

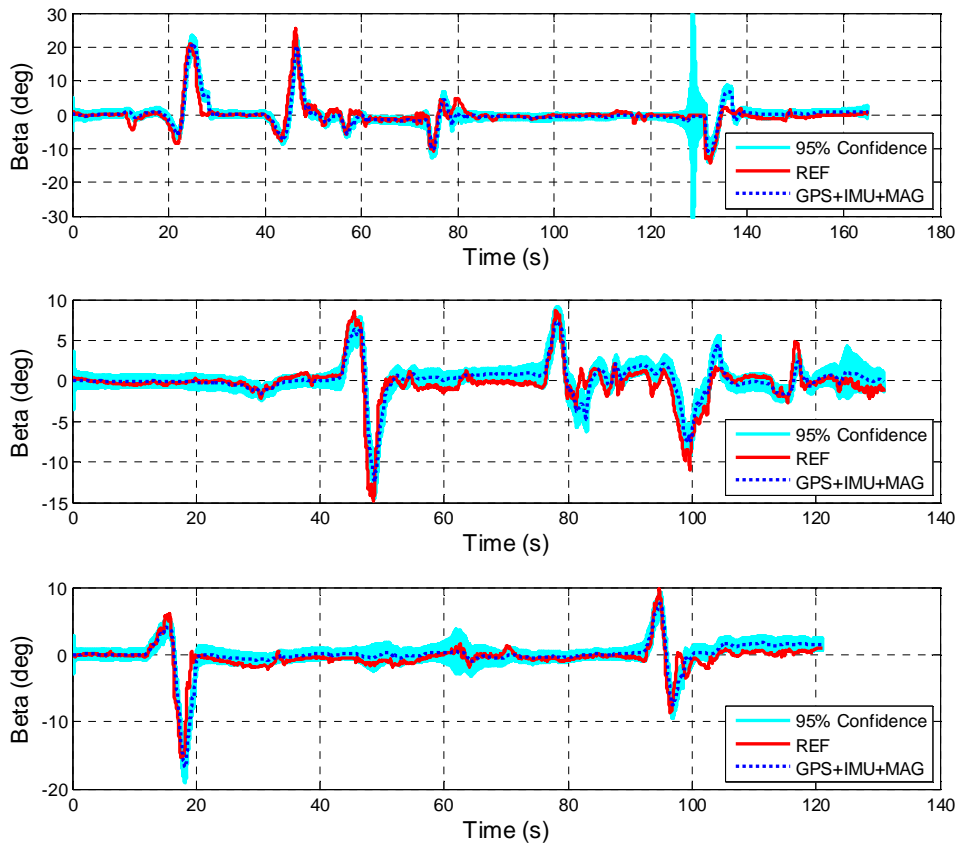


Figure 5.25 The sideslip estimation performance in the neighborhood area experiments

Figure 5.25 shows three representative traces of neighborhood driving test. Overall, the estimation follows the reference signal successfully. However, the sideslip RMS error from 9 collected runs is  $1.67^\circ$ , which is worse than the simulations or on-track data. There are two possible reasons for the performance degradation; road pitch angles and noisy magnetic field. Figure 5.26 presents graphs of another test data. Unlike the simulation or on-track environments, the neighborhood area had several road segments of road grade angles. If the road has significant incline, it would be recognized as banked road in the proposed method due to zero pitch assumption. Roll estimation errors observed in Figure 5.26 (b) are believed to be partly due to road pitch angles. Errors in roll estimation would induce the sideslip estimation error because removal of roll gravitational effect from lateral measurements would be erroneous. This is seen in Figure

5.26 (b) from 100 sec to 140 sec.

Road pitch angles of all the neighborhood data and on-track data are plotted in Figure 5.27 (a). Blue dots represent on-track and red dots neighborhood area. Time axis is normalized to facilitate the comparison. It can be seen that that neighborhood area had wider range of road pitch angle than on-track area. Magnetic field norm deviation of the neighborhood data and on-track data are plotted in the same way in Figure 5.27 (b). This deviation is considered as magnetic field noise and two black lines are threshold envelopes to determine the magnetic disturbance. In other words, if the magnetic field norm deviates to cross the black line, its magnetic field is considered as being disturbed. It is clearly seen that neighborhood area had more noise in magnetic field than on-track. This explain further accuracy degradation of the neighborhood area compared to the on-track area.

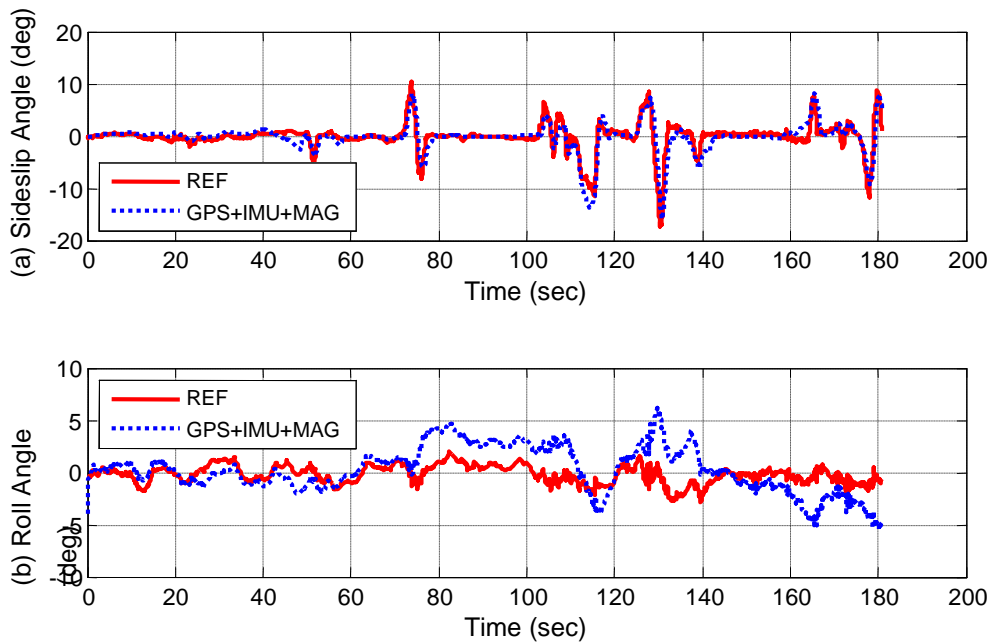


Figure 5.26 A neighborhood experiment data showing error source



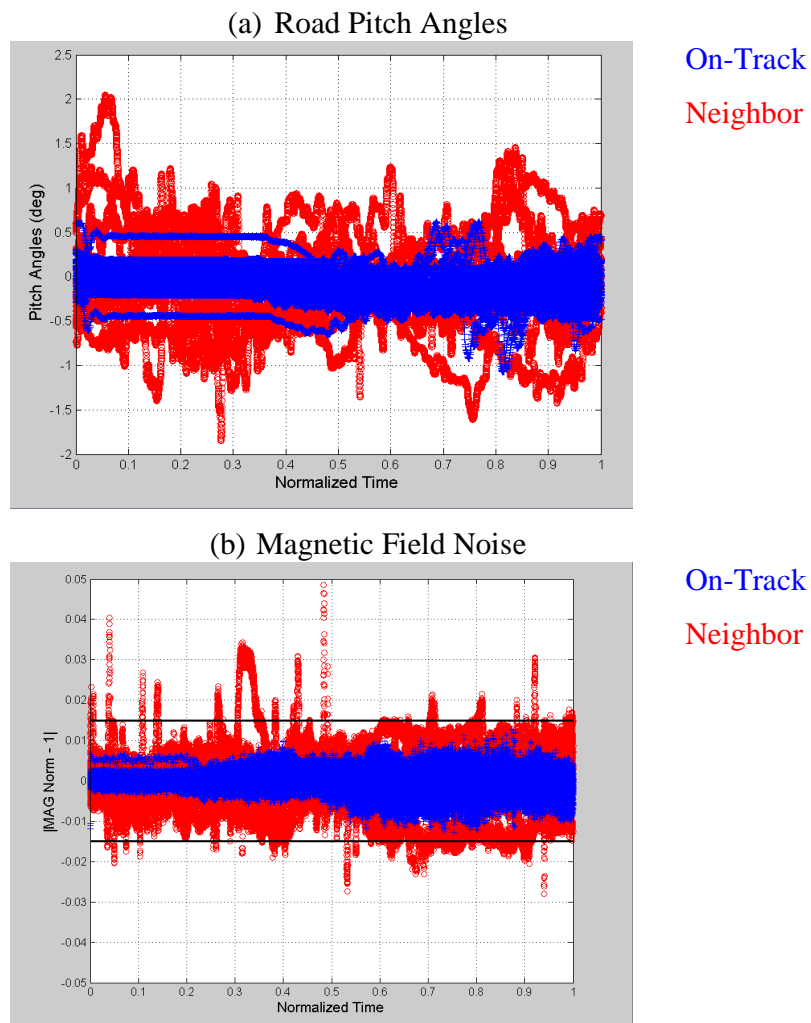


Figure 5.27 Comparison of road pitch angles and magnetic field noise. Red dots represent the neighborhood area and blue dots the on-track area.

## 5.7 Discussions

This chapter has discussed how to combine measurements of GPS, IMU and a magnetometer toward vehicle sideslip angle estimation. Using a magnetometer is the unique feature which makes the proposed method different from other sideslip estimation methods. The author proposed two Kalman filters to (1) extract vehicle yaw/roll angles from a magnetometer and (2) estimate sideslip angles based on the obtained yaw/roll

angles. As a result, the vehicle sideslip angle can be estimated regardless of road bank angles on various frictional surfaces at low-cost.

Because the Earth's magnetic field is very weak, the magnetometer measurements are susceptible to large errors. We have shown that the large disturbance can be detected by monitoring the magnetic field norm. To reject magnetic disturbances, a stochastic filter has been proposed and integrated on the Kalman filter framework. As the vehicle yaw and roll angles are obtained by merging IMU and a magnetometer, the vehicle sideslip angle is easily calculated by using the GPS velocity measurements. The latency in GPS measurements are handled by the measurement shift technique. The proposed method has been verified by a comprehensive set of simulations and experiments.

The sideslip RMS error in simulation is  $0.68^\circ$ . On-track experimental data show the RMS error of  $1.3^\circ$  and the neighborhood area data has the RMS error of  $1.67^\circ$ . This performance degradation is caused by noisy magnetic fields on the track and the public roads. Road pitch angles of the neighborhood area explain further performance degradation of neighborhood area data. If the road pitch angle is provided by a separate means such as digital road map, the sideslip estimation accuracy may be improved.

This method is assessed against the requirements stated in Section 1.3. The GPS receiver can cost only \$200 and a magnetometer price is in \$20~\$30 range. The IMU cost is estimated to be in \$10~\$20 range. Therefore total integration cost is at most \$250 which satisfies the low-cost requirement. In fact, if just GPS receiver and a core chip are used, the price will be lower. Vehicle parameters such as tire cornering stiffness, mass, and moment of inertia do not influence the estimation performance of the method. It is because the proposed method basically does not rely on the bicycle model during turning. The bicycle model is utilized during straight driving, but it was shown that the bicycle model performance is not influenced by accuracy of vehicle parameters during straight driving. Therefore robustness requirement #1 is satisfied. Simulation results showed that the proposed method was capable of providing accurate vehicle sideslip estimation on two different frictional surfaces (asphalt and ice) regardless of road bank angles. The experimental results support this by estimating the vehicle sideslip and roll angles on packed snow and ice surfaces. Consequently the robustness requirement #2 and #3 are met. Results from the simulation and on-track experiments showed that this method met

the accuracy requirement (RMS error of 1.5°). However, the result of the neighborhood area experiment showed that the accuracy performance could deteriorate by road pith angles and noisier magnetic field.

Even though the author relied on the magnetic norm to detect disturbances, a different disturbance detection method is available based on the mahalanobis distance [80-81]. Recall equations of (3.6)-(3.10) of Section 3.1 here. When a measurement update is available, the Kalman filter provides the innovation and its covariance. Then the mahalanobis distance is calculated as

$$\text{m-distance}(k) = (z_k - H_k \hat{x}_k^-)^T (H_k P_k^- H_k^T + R_k)^{-1} (z_k - H_k \hat{x}_k^-) \quad (5.24)$$

This is a scalar value representing normalized distance between a measurement and predicted state from the previous time step through the plant dynamics. If this distance is extremely high in the statistical sense, that measurement is rejected as outlier. The threshold to determine the outlier is calculated from the chi-square cumulative distribution.

Figure 5.28 shows the magnetic field norm, normalized innovation distance, and yaw angle estimations of the author's method and mahalanobis distance-based method. The simulation of Section 5.6.1 is used and 99% confidence value is used to set the disturbance detection threshold for the mahalanobis distance-based method. Several peaks in the figure (a) suggest disturbances in the magnetic field. In the figure (b), the innovation distances are normalized for direct comparison. The blue line is for the author's method and the green line is for mahalanobis distance. As can be seen from the figure (a) and (b), when disturbances occur, both methods successfully detect and reject them. As a result, both methods can estimate the vehicle yaw angles accurately even when the magnetic field is disturbed.

The mahalanobis distance-based disturbance rejection assumes that the state prediction from the previous time step ( $H_k \hat{x}_k^-$  in equation(5.24)) is reasonably accurate. If this assumption is violated, disturbances detection would be erroneous and induced errors may not be recovered. The simulation has run once more in the same way except that 4 deg/sec yaw rate was injected to the yaw rate measurement from 120 sec to 145 sec.

Figure 5.29 shows the associated graphs. Several peaks in the magnetic field norm suggest disturbances. Up to 120 sec, both methods successfully reject disturbances. The injected yaw rate from 120 sec to 145 sec introduces errors in  $H_k \hat{x}_k^-$  in equation(5.24). During that time, both methods are negatively influenced. However, the mahalanobis distance falsely grows and once it passes the disturbance detection threshold, even legitimate measurements are rejected due to the false disturbance detection. As a result, the yaw angle estimation of the mahalanobis distance-based method stays inaccurate where the author’s method recovered the estimation accuracy once the injected bias is removed.

The mahalanobis-based method is very effective disturbance rejection logic. In most cases, it will work as designed. However, this dissertation deals with the ESC system which is a safety critical system. Consequently more robust disturbance detection system is preferred. In that sense, the magnetic field norm-based disturbance detection method has a value over the mahalanobis distance-based method.

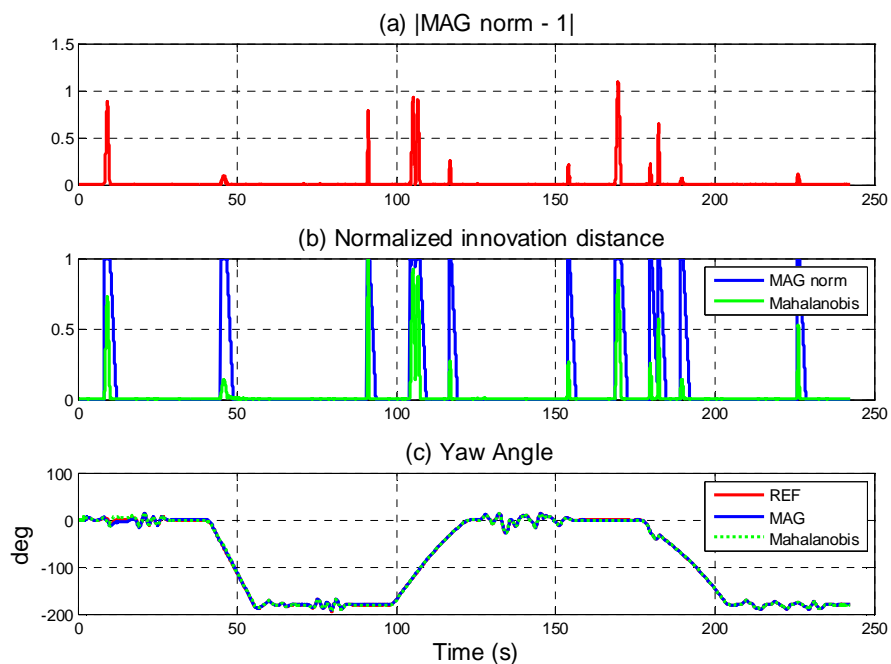


Figure 5.28 Magnetic field disturbance detection/rejection performance comparison.

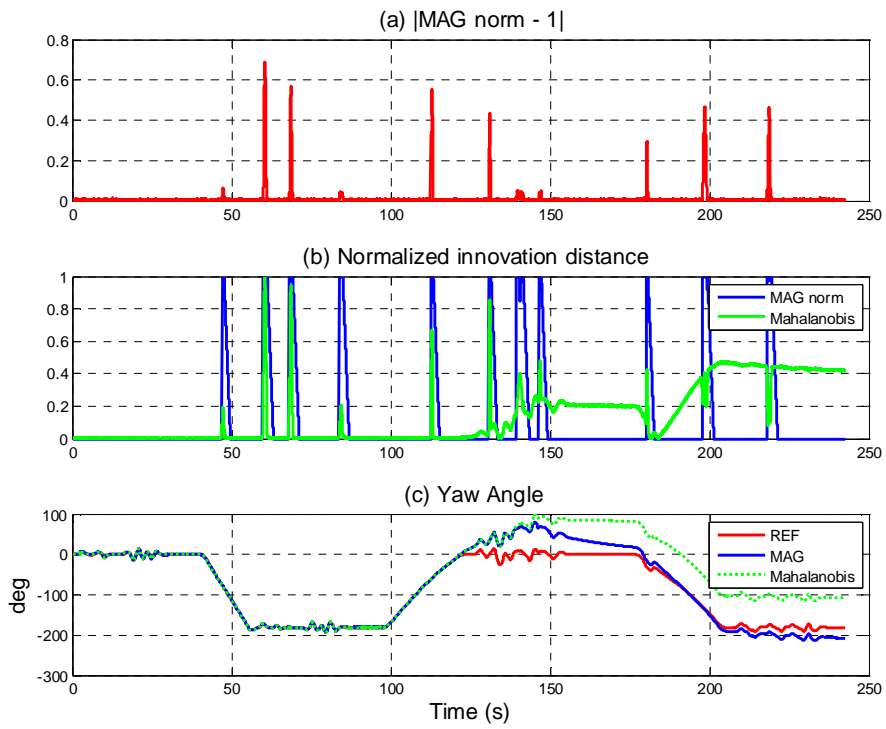


Figure 5.29 Magnetic field disturbance detection/rejection performance comparison. 4 deg/sec bias is injected to yaw rate measurements from 120 sec to 145 sec.

## CHAPTER 6

# CONCLUSIONS AND FUTURE WORK

### 6.1 Conclusions

The author has investigated low-cost methods to estimate the vehicle sideslip angle using GPS technology. As GPS can measure velocity via the Doppler Effect, the coarse angle (the direction where a vehicle moves) is easily measured. Accordingly, the problem comes down to how to measure vehicle heading angles. The author has proposed two methods; (1) two-GPS receiver-based and (2) GPS/magnetometer-based.

The two-GPS method must be distinguished from dual antenna method proposed by Ryu [29]. Ryu's method measures phase shift of the carrier waves arriving at two different antennae, where the author's method uses velocities of two GPS receivers. The author's method drops the integrating cost to several hundred dollars whereas Ryu's method costs more than \$10,000. As the two-GPS method is based on kinematics, it does not require accurate vehicle parameters such as tire cornering stiffness. In fact, two totally different types of vehicles (a pickup truck and a sports car) were employed for experimental verification without technical problems. However, the two-GPS method has performance limitations. It can observe the vehicle sideslip angle only when a vehicle turns at considerable yaw rate. Experimental verification yielded the RMS error of  $2.6^\circ$  when the vehicle turns at yaw rate of  $10^\circ/\text{sec}$  or greater, where the Oxford RT2502 (which is identical to Ryu's method in concept) claims of the RMS error of  $0.4^\circ$ . The estimation accuracy would be degraded if the vehicle is on a banked road.

To estimate the vehicle sideslip regardless of road bank angles, the author has proposed to combine a magnetometer with IMU and GPS. A magnetometer can measure vehicle yaw and roll angles. The cost is about \$10 dollars per magnetometer. However, magnetometer measurements are highly susceptible to large errors and it keeps a magnetometer from being a popular sensor in automotive safety system. To resolve it, the

author proposed a stochastic filter and integrated it on the Kalman filter framework. At the end, measurements of GPS, IMU and a magnetometer are combined on the modified Kalman filter to yield the vehicle sideslip angle estimation. As a result, this method can estimate slip angles even when a vehicle is on banked road and the on-track experimental verification showed the satisfactory estimation accuracy (RMS error of  $1.3^\circ$ ). However, the experimental verification in neighborhood area revealed that road pitch and more noise in magnetic field deteriorated the estimation accuracy.

The author specified five requirements of a new method in Section 1.3. Both of the proposed methods met the low-cost requirement, robustness requirement #1, and robustness requirement #2. In other words, both of the proposed methods can estimate the vehicle sideslip angles on various frictional surfaces without information of vehicle parameters at low cost (<\$ 500). As the GPS/magnetometer-based method could measure vehicle roll angles, it satisfied the robustness requirement #3 while the two-GPS method did not. In terms of the estimation accuracy requirement, the GPS/magnetometer-based method showed the potential but it also showed that the estimation accuracy was vulnerable to road pitch angles and magnetic field noise. Future works for further improvements are presented in the following section.

## **6.2 Future Work**

### **6.2.1 Estimation Accuracy Improvement**

Experimental results of the neighborhood area showed that the estimation accuracy of the GPS/magnetometer-based method deteriorated due to unrecognized road pitch angles. The GPS/magnetometer-based method assumed zero pitch angles; hence it extracted only yaw and roll angles from magnetometer measurements. The magnetometer measurement equation of (5.1) will be reinvestigated to measure yaw, pitch, and roll angles of a vehicle.

### **6.2.2 Accelerometer Bias Estimation**

Estimation of a bias in an accelerometer signal is a challenging problem in the current ESC system. This is mainly because road bank/pitch angles cannot be accurately

measured with the current on-board sensors including the IMU, the wheel speed sensor, and the steering sensor. Since a magnetometer is capable of measuring road bank angles, accelerometer bias estimation was tried through state augmentation. However, due to the augmented state, the Heading Kalman filter lost the stochastic observability. Therefore, a separate method for accelerometer bias estimation is demanded. This will improve the stochastic observability.

### 6.2.3 Position-based Estimation

The author has focused on the GPS velocity measurement, rather than GPS position measurement. It is because the position measurement accuracy of a standard GPS is not accurate enough to be used for the sideslip and road bank angle estimation. A Differential GPS (DGPS) technology can provide the position measurement accurate enough for this study, but the DGPS requires a reference tower [26, 32]. This has been a significant drawback of position-based GPS methods for sideslip/road bank angle estimations. However, as pointed out in 1.2.3, the United States government is now building a network of permanent GPS base stations to provide a continuously operating referencing station (CORS) [27]. As of May 2010, the CORS network contains over 1,450 stations, and the network continues to expand. Accordingly, accurate position measurements may be available by national-wide DGPS in the near future.

The impact of accurate position measurements on sideslip and road bank angle estimations will be investigated. Combined with the advanced digital map technology, accurate positioning of a vehicle has huge potentials in vehicle active safety systems. For example, if the road bank angle information is available by the advanced digital map and the vehicle position is accurately known, road bank angle-related active safety functions can be improved.



## APPENDICES

### Appendix A

#### Allan Variance analysis of the velocity measurement from the GPS receiver (U-blox LEA 5)

The Allan variance can be viewed as the time domain equivalent of the power spectrum. Instead of power as a function of frequency it gives power as a function of averaging time. It is an efficient tool to identify the low-frequency component of noise source. To construct the Allan variance plot for the error analysis of a sensor, its time-series data needs to be collected when the sensor is isolated from any excitation ( Figure A.1(a)). Then the following steps need to be conducted.

1. Define a vector of averaging times,  $\tau_{av}$ , as:

$$\tau_{av} = [1 \text{ sec}, 2 \text{ sec}, \dots, T/2 \text{ sec}]$$

where T: total time duration of data recording

2. For each  $\tau_{av}$ , divide the entire data record into  $M=T/\tau_{av}$  clusters(Figure A.1(b))
3. For each  $k^{\text{th}}$  cluster, compute the time average. That is:

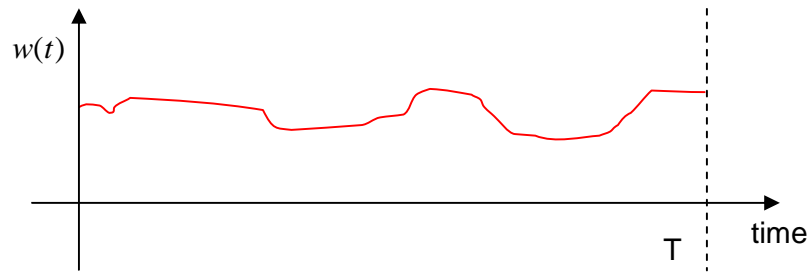
$$\bar{\omega}(k) = \frac{1}{\tau_{av}} \int_{t_k}^{t_k + \tau_{av}} \omega(t) dt$$

Red dots in Figure A.1(c) represent these averages.

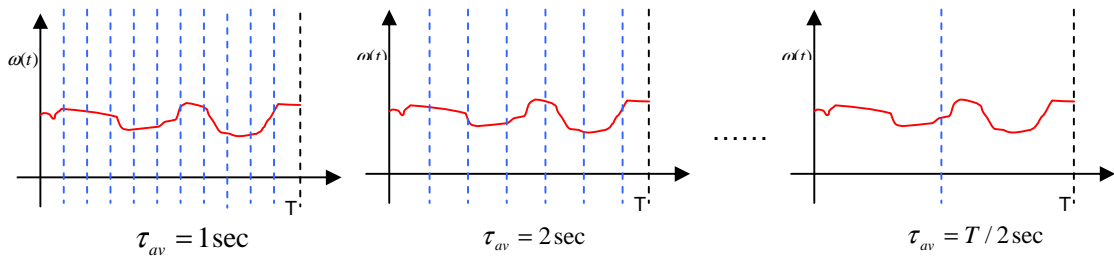
4. Use these cluster averages to form new variable called the Allan variance, which is defined as:

$$\sigma^2(\tau_{av}) = \frac{1}{2} \mathcal{E}[(\bar{\omega}(k+1) - \bar{\omega}(k))^2]$$

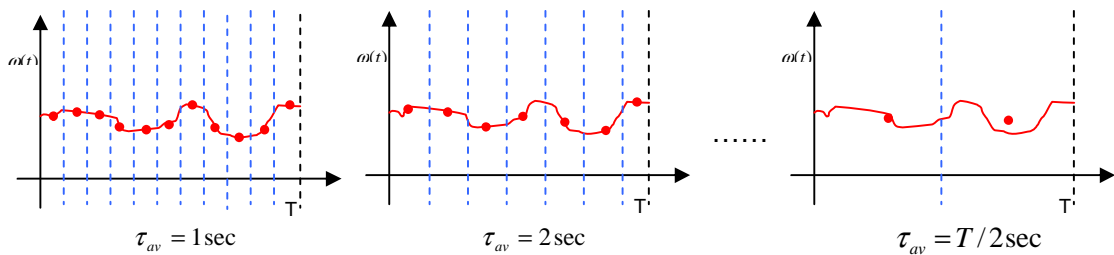
5. On a log-log scale, plot  $\sigma(\tau_{av})$ . This is the Allan variance plot



(a) Time-series data when a sensor is free-from excitation



(b) Clustering of time-series data



(c) Average calculation of each cluster

Figure A.1 Graphical procedures for Allan Variance plot: (a) Time-series data when a sensor is free-from excitation, (b) Clustering of time-series data, (c) Average calculation of each cluster

It is known that the Allan variance plot has a close relationship with the error dynamics [1]. Figure A.2 shows four different error dynamics match different curves in the Allan variance plot and Table A.1 summarizes the slopes of the Allan variance plot based on error dynamics.

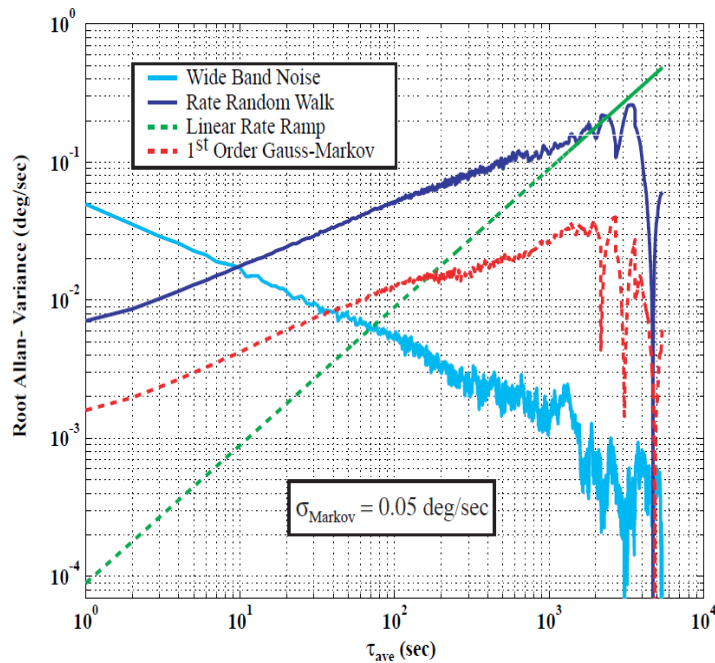
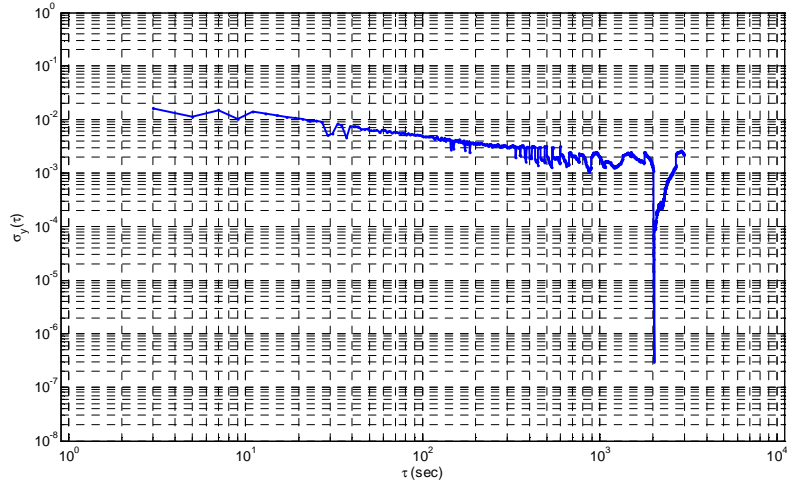


Figure A.2 Allan Variance for various error dynamics (Adapted from [1])

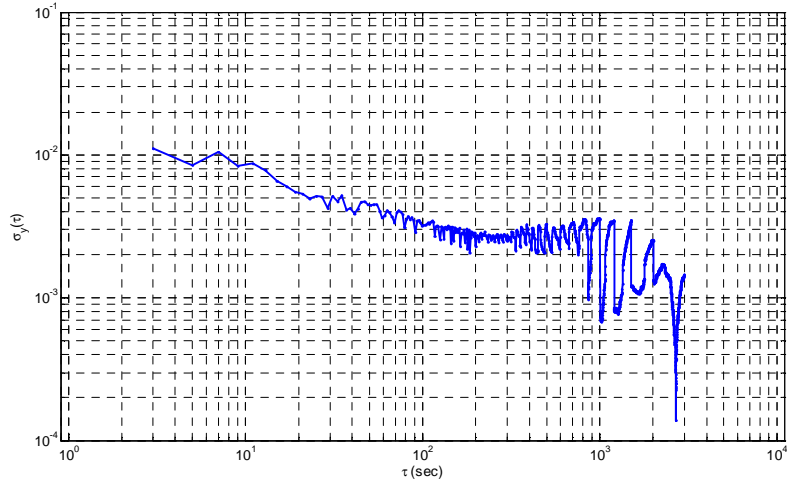
Table A.1 Summary of standard error sources and Allan variance slopes (Adapted from [1])

Error Dynamics	Allan Variance Slope
Wide-Band Noise	$-\frac{1}{2}$
First Order Gauss-Markov Process	$\frac{1}{2}$
Rate Random Walk	$\frac{1}{2}$
Linear Random Ramp	1
Quantization Noise	-1
Sinusoidal Input	1
Flicker Noise	0

(a) X-direction in ECEF



(b) Y-direction in ECEF



(c) Z-direction in ECEF

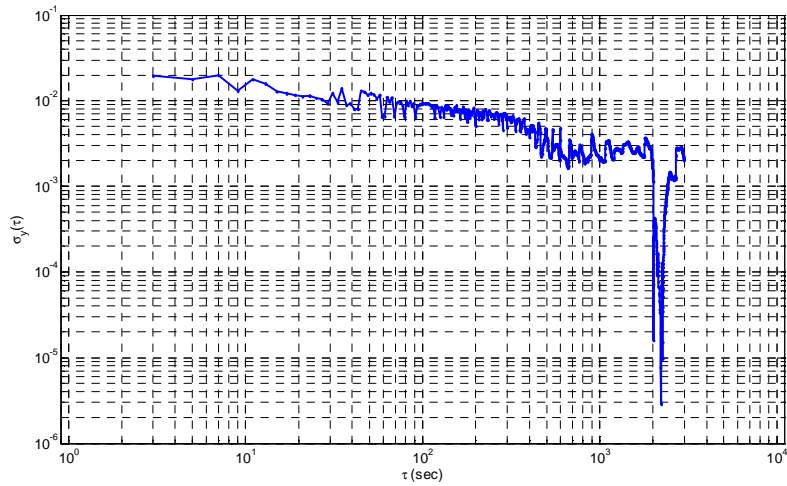


Figure A.3 Allan variance plots of three dimensional velocities from U-blox LEA 5: (a) X direction in ECEF, (b) Y-direction, and (c) Z-direction

This procedure has been conducted for the velocity measurement from the U-blox LEA 5 GPS receiver, which is mainly used for this research. Velocity data was collected for duration of 1.5 hours when the vehicle stands still. The Allan variance plots are presented in Figure A.3. There are three plots because one GPS receiver provides three-dimensional velocities. The Earth-Centered, Earth-Fixed (ECEF) coordinate was used. As can be seen, all three graphs show a slope of -1/2 in the log-log scale. This means that only white noise exists in the noise of velocity measurement from the GPS receiver.

## Appendix B

### Resolution analysis of the sideslip estimation method using two GPS receivers

$$V_{fn} = U \cos \psi - (V + L_f \dot{\psi}) \sin \psi \quad (4.1)$$

$$V_{fe} = U \sin \psi + (V + L_f \dot{\psi}) \cos \psi \quad (4.2)$$

$$V_{rn} = U \cos \psi - (V - L_r \dot{\psi}) \sin \psi \quad (4.3)$$

$$V_{re} = U \sin \psi + (V - L_r \dot{\psi}) \cos \psi \quad (4.4)$$

Recall the four basic kinematic equations of CHAPTER 4. If there are measurement errors in the left hand side terms, the accuracy of  $\{U, V, \psi, \dot{\psi}\}$  calculation would be affected. To assess this, Multi-variable Taylor expansion is applied [60]. That is:

$$f(\bar{x} + \bar{p}) = f(\bar{x}) + Df(\bar{x})\bar{p} + \bar{p}' D^2 f(\bar{x} + \bar{q})\bar{p} \quad (B.1)$$

$$\text{Where } Df(\bar{x}) = \left[ \frac{\partial f}{\partial x_1}, \dots, \frac{\partial f}{\partial x_n} \right] \text{ and } D^2 f(\bar{x}) = \begin{bmatrix} f_{x_1 x_1} & \dots & f_{x_1 x_n} \\ \vdots & \ddots & \vdots \\ f_{x_n x_1} & \dots & f_{x_n x_n} \end{bmatrix}$$

Applying (B.1) to (4.1)-(4.4) would result in (B.2)

$$\begin{bmatrix} \delta V_{fn} \\ \delta V_{fe} \\ \delta V_m \\ \delta V_{re} \end{bmatrix} = \begin{bmatrix} \cos \psi & -\sin \psi & -U \sin \psi - (V + L_f \dot{\psi}) \cos \psi & -L_f \sin \psi \\ \sin \psi & \cos \psi & U \cos \psi - (V + L_f \dot{\psi}) \sin \psi & L_f \cos \psi \\ \cos \psi & -\sin \psi & -U \sin \psi - (V - L_r \dot{\psi}) \cos \psi & L_r \sin \psi \\ \sin \psi & \cos \psi & U \cos \psi - (V - L_r \dot{\psi}) \sin \psi & -L_r \cos \psi \end{bmatrix} \begin{bmatrix} \delta U \\ \delta V \\ \delta \psi \\ \delta \dot{\psi} \end{bmatrix} + \begin{bmatrix} RT_1 \\ RT_2 \\ RT_3 \\ RT_4 \end{bmatrix} \quad (\text{B.2})$$

Where

$$RT_1 = -2\delta U \delta \psi \sin(\psi + q_\psi) - 2\delta V \delta \psi \cos(\psi + q_\psi) + \delta \psi^2 \{-(U + q_U) \cos(\psi + q_\psi) + (V + q_v + L_f (\dot{\psi} + q_{\dot{\psi}})) \sin(\psi + q_\psi)\} - 2\delta \psi \delta \dot{\psi} L_f \cos \psi \quad (\text{B.3})$$

$$RT_2 = 2\delta U \delta \psi \cos(\psi + q_\psi) - 2\delta V \delta \psi \sin(\psi + q_\psi) - \delta \psi^2 \{(U + q_U) \sin(\psi + q_\psi) + (V + q_v + L_f (\dot{\psi} + q_{\dot{\psi}})) \cos(\psi + q_\psi)\} - 2\delta \psi \delta \dot{\psi} L_f \sin \psi \quad (\text{B.4})$$

$$RT_3 = -2\delta U \delta \psi \sin(\psi + q_\psi) - 2\delta V \delta \psi \cos(\psi + q_\psi) + \delta \psi^2 \{-(U + q_U) \cos(\psi + q_\psi) + (V + q_v - L_r (\dot{\psi} + q_{\dot{\psi}})) \sin(\psi + q_\psi)\} + 2\delta \psi \delta \dot{\psi} L_r \cos \psi \quad (\text{B.5})$$

$$RT_4 = 2\delta U \delta \psi \cos(\psi + q_\psi) - 2\delta V \delta \psi \sin(\psi + q_\psi) - \delta \psi^2 \{(U + q_U) \sin(\psi + q_\psi) + (V + q_v - L_r (\dot{\psi} + q_{\dot{\psi}})) \cos(\psi + q_\psi)\} + 2\delta \psi \delta \dot{\psi} L_r \sin \psi \quad (\text{B.6})$$

Rearrange (B.2) like (B.7).

$$\begin{bmatrix} \delta V_{fn} \\ \delta V_{fe} \\ \delta V_m \\ \delta V_{re} \end{bmatrix} = \begin{bmatrix} LT_1 \\ LT_2 \\ LT_3 \\ LT_4 \end{bmatrix} + \begin{bmatrix} RT_1 \\ RT_2 \\ RT_3 \\ RT_4 \end{bmatrix} = \begin{bmatrix} LT_1(1 + \frac{RT_1}{LT_1}) \\ LT_2(1 + \frac{RT_2}{LT_2}) \\ LT_3(1 + \frac{RT_3}{LT_3}) \\ LT_4(1 + \frac{RT_4}{LT_4}) \end{bmatrix} \quad (\text{B.7})$$

Where  $LT_1$ - $LT_4$  are the expansion of Jacobian terms of (B.2). It is extremely difficult to find the exact answers of (B.7) as is. Therefore some tricks are employed to find the

reasonably close answer of (B.7). The tricks are (i) to assume  $\left| \frac{RT_1}{LT_1} \right| \sim \left| \frac{RT_4}{LT_4} \right|$  ( henceforth

referred to as  $\left| \frac{RT_{xx}}{LT_{xx}} \right|$ ) is negligibly small, (ii) to solve the linearized equations, and (iii)

plug the outcomes of (ii) into  $\left| \frac{RT_{xx}}{LT_{xx}} \right|$  to confirm the negligible assumption was

legitimate. If the Jacobian is not singular, solving the linearized equation would yield (B.8)~(B.11)

$$\delta U = -\left\{ (V - L_r \dot{\psi}) \cos \psi \delta V_{fn} + (V - L_r \dot{\psi}) \sin \psi \delta V_{fe} \right\} / \frac{L \dot{\psi}}{L \dot{\psi}} + \left\{ (V + L_f \dot{\psi}) \cos \psi \delta V_{rn} + (V + L_f \dot{\psi}) \sin \psi \delta V_{re} \right\} / \frac{L \dot{\psi}}{L \dot{\psi}} \quad (\text{B.8})$$

$$\delta V = \left\{ (-L_r \dot{\psi} \sin \psi + U \cos \psi) \delta V_{fn} + (L_r \dot{\psi} \cos \psi + U \sin \psi) \delta V_{fe} \right\} / \frac{L \dot{\psi}}{L \dot{\psi}} - \left\{ (L_f \dot{\psi} \sin \psi + U \cos \psi) \delta V_{rn} + (-L_f \dot{\psi} \cos \psi + U \sin \psi) \delta V_{re} \right\} / \frac{L \dot{\psi}}{L \dot{\psi}} \quad (\text{B.9})$$

$$\delta \psi = \frac{-\cos \psi \delta V_{fn} - \sin \psi \delta V_{fe} + \cos \psi \delta V_{rn} + \sin \psi \delta V_{re}}{L \dot{\psi}} \quad (\text{B.10})$$

$$\delta \dot{\psi} = \frac{-\sin \psi \delta V_{fn} + \cos \psi \delta V_{fe} + \sin \psi \delta V_{rn} - \cos \psi \delta V_{re}}{L} \quad (\text{B.11})$$

Assume  $\delta V_{fn} = \delta V_{fe} = \delta V_{rn} = \delta V_{re} \equiv \delta V_{GPS}$ , then

$$|\delta U| \leq \sqrt{2} |\delta V_{GPS}|, |\delta V| \leq \sqrt{2} |\delta V_{GPS}|, |\delta \psi| \leq \frac{2\sqrt{2}}{|L \dot{\psi}|} |\delta V_{GPS}|, |\delta \dot{\psi}| \leq \frac{2\sqrt{2}}{|L|} |\delta V_{GPS}| \quad (\text{B.12})$$

By using triangle inequality on (B.3)~(B.6), along with (B.12), (B.13)~(B.16) are induced.

$$\left| \frac{RT_1}{LT_1} \right| \leq \frac{8 |\delta V_{gps}|^2}{|L \dot{\psi}|^2} (2L |\dot{\psi}| + 3L_f |\dot{\psi}| + |V|) \quad (\text{B.13})$$

$$\left| \frac{RT_2}{LT_2} \right| \leq \frac{8 |\delta V_{gps}|^2}{|L \dot{\psi}|^2} (2L |\dot{\psi}| + 3L_f |\dot{\psi}| + |V|) \quad (\text{B.14})$$

$$\left| \frac{RT_3}{LT_3} \right| \leq \frac{8 |\delta V_{gps}|^2}{|L \dot{\psi}|^2} (2L |\dot{\psi}| + 3L_r |\dot{\psi}| + |V|) \quad (\text{B.15})$$

$$\left| \frac{RT_4}{LT_4} \right| \leq \frac{8 |\delta V_{gps}|^2}{|L \dot{\psi}|^2} (2L |\dot{\psi}| + 3L_r |\dot{\psi}| + |V|) \quad (\text{B.16})$$

$\left| \frac{RT_{xx}}{LT_{xx}} \right|$  decreases as the absolute value of yaw rate increases. Table B.1 displays the value of  $\left| \frac{RT_{xx}}{LT_{xx}} \right|$  when  $L=4.8\text{m}$  and  $|\delta V_{gps}| = 0.01\text{ m/s}$ , and if absolute value of the yaw rate is greater than  $10^\circ/\text{sec}$ , the assumption of negligible high order terms ( $RT_1 \sim RT_4$  in (B.2)) is legitimate.

Table B.1  $\left| \frac{RT_{xx}}{LT_{xx}} \right|$  as a function of yaw rate

YawRate( $^\circ/\text{sec}$ )	3	5	10	15	30	45	60
$\left  \frac{RT_{xx}}{LT_{xx}} \right $	1	0.6	0.3	0.2	0.1	0.06	0.05

$$\sigma^2(aX + bY) = a^2\sigma^2(X) + b^2\sigma^2(Y) + 2ab\text{Cov}(X, Y) \quad (\text{B.17})$$

Standard deviation of a linear combination of two signals is computed from (B.17). The east- and north-bound velocities of a GPS receiver are correlated where velocities of two different GPS receivers are uncorrelated. Therefore, applying it to (B.8)~(B.11) would result in (B.18)

$$\sigma(\delta\psi) = \frac{\sqrt{2\sigma^2(\delta V_{gps}) + 2\sin 2\psi \text{Cov}(\delta V_n, \delta V_e)}}{|L\dot{\psi}|},$$

$$\sigma(\delta V) = \frac{\sqrt{(2U^2 + (L_f^2 + L_r^2)\dot{\psi}^2)\sigma^2(\delta V_{gps}) + [(U^2 + L_r^2\dot{\psi}^2)\sin(2\psi + \psi_1) + (U^2 + L_f^2\dot{\psi}^2)\sin(2\psi + \psi_2)]\text{Cov}(\delta V_n, \delta V_e)}}{|L\dot{\psi}|}$$

where

$$\tan\psi_1 = \frac{2L_r\dot{\psi}U}{U^2 - L_r^2\dot{\psi}^2}, \tan\psi_2 = \frac{-2L_f\dot{\psi}U}{U^2 - L_f^2\dot{\psi}^2}, \text{and } \text{Cov}(\delta V_{fn}, \delta V_{fe}) = \text{Cov}(\delta V_m, \delta V_{re}) \equiv \text{Cov}(\delta V_n, \delta V_e) \quad (\text{B.18})$$



Since  $|\sin(\bullet)| \leq 1$ , (B.18) is converted into

$$\frac{\sqrt{2\sigma^2(\delta V_{gps}) - 2|Cov(\delta V_n, \delta V_e)|}}{|L\dot{\psi}|} \leq \sigma(\delta\psi) \leq \frac{\sqrt{2\sigma^2(\delta V_{gps}) + 2|Cov(\delta V_n, \delta V_e)|}}{|L\dot{\psi}|}, \quad (\text{B.19})$$

$$\left| \sigma^2(\delta V) - \frac{(2U^2 + (L_f^2 + L_r^2)\dot{\psi}^2)\sigma^2(\delta V_{gps})}{(L\dot{\psi})^2} \right| \leq \frac{(2U^2 + (L_f^2 + L_r^2)\dot{\psi}^2)|Cov(\delta V_n, \delta V_e)|}{(L\dot{\psi})^2}$$

Since  $\beta = \tan^{-1}(V/U) \approx V/U$ ,  $\delta\beta \approx \frac{\delta V}{U}$  if U behaves as a constant compared to V.

Therefore, we can get

$$\left| \sigma^2(\delta\beta) - \frac{(2U^2 + (L_f^2 + L_r^2)\dot{\psi}^2)\sigma^2(\delta V_{gps})}{(LU\dot{\psi})^2} \right| \leq \frac{(2U^2 + (L_f^2 + L_r^2)\dot{\psi}^2)|Cov(\delta V_n, \delta V_e)|}{(LU\dot{\psi})^2} \quad (\text{B.20})$$

## Appendix C

### Bivariate Normal-Uniform Distributions

Recall (5.4) which describes the bivariate normal-uniform distribution. Figure C.1 is a top view of the distribution.

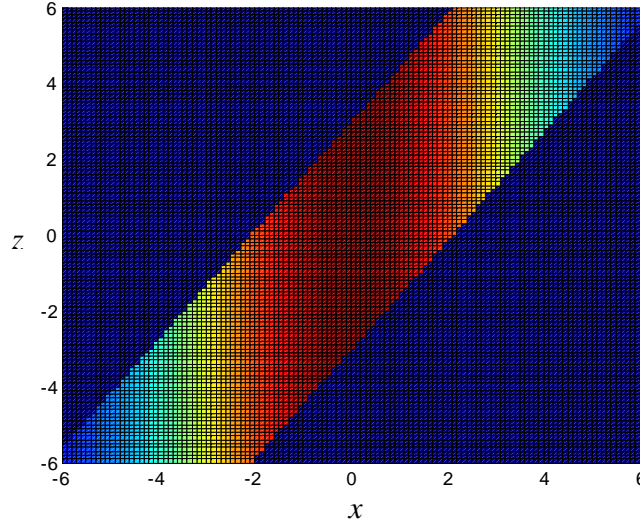


Figure C.1 Top view of bivariate normal-uniform distribution

The joint PDF  $f_{X,Z}(x, z)$  is equal to  $f(z|x) f(x)$ . Without loss of generality,  $\mu_x$  can be shifted to the origin. Therefore (C.1) represents the joint PDF.

$$f_{X,Z}(x, z) = \begin{cases} \frac{1}{4\pi\sigma b_0} e^{-\frac{1}{2}\left(\frac{x}{\sigma}\right)^2} & \text{where } cx - b_0 < z < cx + b_0 \\ 0 & \text{otherwise} \end{cases} \quad (\text{C.1})$$

According to (5.3), the optimal estimation would be

$$\hat{x} = \varepsilon(x|z) = \int x \frac{f_{X,Z}(x, z)}{f_Z(z)} dx = \int_{(z-b_0)/c}^{(z+b_0)/c} \left[ \frac{x e^{-\frac{1}{2}\left(\frac{x}{\sigma}\right)^2}}{\int_{(z-b_0)/c}^{(z+b_0)/c} e^{-\frac{1}{2}\left(\frac{s}{\sigma}\right)^2} ds} \right] dx$$

$$= \frac{\sigma^2 \left( e^{-\frac{1}{2\sigma^2} \left( \frac{z-b_0}{c} \right)^2} - e^{-\frac{1}{2\sigma^2} \left( \frac{z+b_0}{c} \right)^2} \right)}{\int_{(z-b_0)/c}^{(z+b_0)/c} e^{-\frac{1}{2} \left( \frac{s}{\sigma} \right)^2} ds} \quad (C.2)$$

## Appendix D

### Bivariate Normal-Truncated Normal Distribution

Recall (5.6) for the bivariate normal-truncated normal distribution and Figure D.1 is its top view.

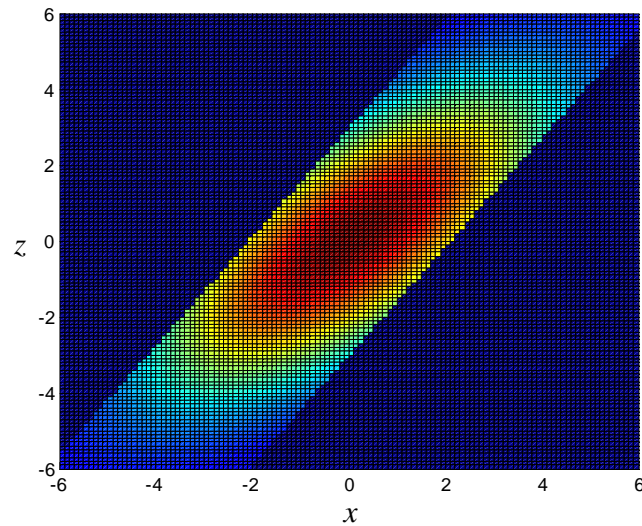


Figure D.1 Top view of the bivariate normal-truncated normal distribution

The joint PDF would be identical to the bivariate normal distribution as seen

$$f_{X,Z}(x, z) = \begin{cases} A \exp \left[ -\frac{1}{2(1-\rho^2)} \left( \left( \frac{x}{\sigma_x} \right)^2 - 2\rho \left( \frac{x}{\sigma_x} \right) \left( \frac{z}{\sigma_z} \right) + \left( \frac{z}{\sigma_z} \right)^2 \right) \right] & \text{where } |x - x_o| < x_b \\ 0 & \text{otherwise} \end{cases} \quad (D.1)$$

$$\text{where } x_o \equiv \rho \frac{\sigma_x}{\sigma_z} z \text{ and } x_b \equiv \rho \frac{\sigma_x}{\sigma_z} z_b$$

$A$  is a constant to be determined. The optimal MMSE estimation is calculated from (5.3) as seen below

$$\begin{aligned}
\hat{x} = \varepsilon(x|z) &= \int_{x_o-x_b}^{x_o+x_b} \frac{Ax \exp\left(-\frac{1}{2}\left(\frac{z}{\sigma_z}\right)^2\right) \exp\left(-\frac{1}{2}\left(\frac{x-x_o}{\sigma_x\sqrt{1-\rho^2}}\right)^2\right)}{\int_{x_o-x_b}^{x_o+x_b} A \exp\left(-\frac{1}{2}\left(\frac{z}{\sigma_z}\right)^2\right) \exp\left(-\frac{1}{2}\left(\frac{s-x_o}{\sigma_x\sqrt{1-\rho^2}}\right)^2\right) ds} dx \\
&= \int_{x_o-x_b}^{x_o+x_b} \frac{x \exp\left(-\frac{1}{2}\left(\frac{x-x_o}{\sigma_x\sqrt{1-\rho^2}}\right)^2\right)}{\int_{x_o-x_b}^{x_o+x_b} \exp\left(-\frac{1}{2}\left(\frac{s-x_o}{\sigma_x\sqrt{1-\rho^2}}\right)^2\right) ds} dx = \int_{-x_b}^{x_b} \frac{(t+x_o) \exp\left(-\frac{1}{2}\left(\frac{t}{\sigma_x\sqrt{1-\rho^2}}\right)^2\right)}{\int_{-x_b}^{+x_b} \exp\left(-\frac{1}{2}\left(\frac{s'}{\sigma_x\sqrt{1-\rho^2}}\right)^2\right) ds'} dt \\
&= \int_{-x_b}^{x_b} \frac{(t+x_o) \exp\left(-\frac{1}{2}\left(\frac{t}{\sigma_x\sqrt{1-\rho^2}}\right)^2\right)}{\sqrt{2\pi(1-\rho^2)}\sigma_x \left\{ \Phi\left(\frac{x_b}{\sigma_x\sqrt{1-\rho^2}}\right) - \Phi\left(\frac{-x_b}{\sigma_x\sqrt{1-\rho^2}}\right) \right\}} dt \\
&= \frac{\int_{-x_b}^{x_b} t \exp\left(-\frac{1}{2}\left(\frac{t}{\sigma_x\sqrt{1-\rho^2}}\right)^2\right) dt + x_o \int_{-x_b}^{x_b} \exp\left(-\frac{1}{2}\left(\frac{t}{\sigma_x\sqrt{1-\rho^2}}\right)^2\right) dt}{\sqrt{2\pi(1-\rho^2)}\sigma_x \left\{ \Phi\left(\frac{x_b}{\sigma_x\sqrt{1-\rho^2}}\right) - \Phi\left(\frac{-x_b}{\sigma_x\sqrt{1-\rho^2}}\right) \right\}} \\
&= 0 + x_o \int_{-x_b}^{x_b} \frac{\exp\left(-\frac{1}{2}\left(\frac{t}{\sigma_x\sqrt{1-\rho^2}}\right)^2\right)}{\sqrt{2\pi(1-\rho^2)}\sigma_x \left\{ \Phi\left(\frac{x_b}{\sigma_x\sqrt{1-\rho^2}}\right) - \Phi\left(\frac{-x_b}{\sigma_x\sqrt{1-\rho^2}}\right) \right\}} dt = x_o \cdot 1 = \rho \frac{\sigma_x}{\sigma_z} z \tag{D.2}
\end{aligned}$$

Where  $\Phi(x) = \int_{-\infty}^x \frac{1}{\sqrt{2\pi}} e^{-\frac{1}{2}t^2} dt$

(D.2) confirms that MMSE estimation of the bivariate normal-truncated normal distribution is identical to that of bivariate normal distribution. The constant in (D.1) is calculated from  $\int_{-\infty}^{\infty} \int_{-\infty}^{\infty} f_{X,Z}(x,z) dx dz = 1$  as seen below

$$\int_{-\infty}^{\infty} \int_{-\infty}^{\infty} f_{X,Z}(x,z) dx dz = \int_{-\infty}^{\infty} \int_{x_o-x_b}^{x_o+x_b} A \exp\left\{-\frac{1}{2}\left(\frac{z}{\sigma_z}\right)^2\right\} \exp\left\{-\frac{1}{2}\left(\frac{x-x_o}{\sigma_x\sqrt{1-\rho^2}}\right)^2\right\} dx dz$$

$$\begin{aligned}
&= A\sigma_x\sqrt{2\pi(1-\rho^2)}\left\{\Phi\left(\frac{x_b}{\sigma_x\sqrt{(1-\rho^2)}}\right)-\Phi\left(\frac{-x_b}{\sigma_x\sqrt{(1-\rho^2)}}\right)\right\}\int_{-\infty}^{\infty}e^{-\frac{1}{2}\left(\frac{z}{\sigma_z}\right)^2}dz \\
&= 2\pi A\sigma_x\sigma_z\sqrt{(1-\rho^2)}\left\{\Phi\left(\frac{x_b}{\sigma_x\sqrt{(1-\rho^2)}}\right)-\Phi\left(\frac{-x_b}{\sigma_x\sqrt{(1-\rho^2)}}\right)\right\}=1 \\
\therefore A &= \frac{1}{2\pi\sigma_x\sigma_z\sqrt{(1-\rho^2)}\left\{\Phi\left(\frac{x_b}{\sigma_x\sqrt{(1-\rho^2)}}\right)-\Phi\left(\frac{-x_b}{\sigma_x\sqrt{(1-\rho^2)}}\right)\right\}} \tag{D.3}
\end{aligned}$$

The corresponding variance is calculated as follows

$$\begin{aligned}
\text{variance} &= \int_{-\infty}^{\infty}\int_{-\infty}^{\infty}(x-x_o)^2 f_{X,Z}(x,z)dxdz \\
&= \int_{-\infty}^{\infty}\int_{x_o-x_b}^{x_o+x_b}A(x-x_o)^2 \exp\left\{-\frac{1}{2}\left(\frac{z}{\sigma_z}\right)^2\right\}\exp\left\{-\frac{1}{2}\left(\frac{x-x_o}{\sigma_x\sqrt{1-\rho^2}}\right)^2\right\}dxdz \\
&= \int_{-\infty}^{\infty}A\exp\left\{-\frac{1}{2}\left(\frac{z}{\sigma_z}\right)^2\right\}\int_{-x_b}^{x_b}x^2 \exp\left\{-\frac{1}{2}\left(\frac{x}{\sigma_x\sqrt{1-\rho^2}}\right)^2\right\}dxdz \\
&= \frac{\int_{-\infty}^{\infty}\frac{1}{\sqrt{2\pi}\sigma_z}\exp\left\{-\frac{1}{2}\left(\frac{z}{\sigma_z}\right)^2\right\}dz\int_{-x_b}^{x_b}\frac{x^2}{\sqrt{2\pi}\sigma_x\sqrt{1-\rho^2}}\exp\left\{-\frac{1}{2}\left(\frac{x}{\sigma_x\sqrt{1-\rho^2}}\right)^2\right\}dx}{\Phi\left(\frac{x_b}{\sigma_x\sqrt{1-\rho^2}}\right)-\Phi\left(\frac{-x_b}{\sigma_x\sqrt{1-\rho^2}}\right)} \\
&= \sigma_x\sqrt{1-\rho^2}\left[\frac{1}{\Phi\left(\frac{x_b}{\sigma_x\sqrt{1-\rho^2}}\right)-\Phi\left(\frac{-x_b}{\sigma_x\sqrt{1-\rho^2}}\right)}+\frac{\frac{2x_b}{\sigma_x\sqrt{1-\rho^2}}\phi\left(\frac{x_b}{\sigma_x\sqrt{1-\rho^2}}\right)}{\left\{\Phi\left(\frac{x_b}{\sigma_x\sqrt{1-\rho^2}}\right)-\Phi\left(\frac{-x_b}{\sigma_x\sqrt{1-\rho^2}}\right)\right\}^2}\right] \\
&= \sigma_x\sqrt{1-\rho^2}m \tag{D.4}
\end{aligned}$$

Where  $\phi(x) = \frac{1}{\sqrt{2\pi}}e^{-\frac{1}{2}x^2}$

(D.4) proves that the variance of the MMSE of the bivariate normal-truncated normal distribution is very similar to that of bivariate normal distribution with only the modification factor ( $m$ ) added.

## Appendix E

### Proof: Linear combination of random variables of normal distributions is also normally distributed

Let two random variables of  $u$  and  $v$  are described by the bivariate normal distribution. Without loss of generality, the joint pdf is

$$f_{u,v}(u, v) = \frac{1}{2\pi\sqrt{1-\rho^2}} \exp\left(-\frac{u^2 - 2\rho uv + v^2}{2(1-\rho^2)}\right)$$

where (E.1)

$$\rho = \frac{\sigma_{uv}}{\sigma_u \sigma_v}$$

Let  $x$  be the linear combination of  $u$  and  $v$  as

$$x = h_1 u + h_2 v \tag{E.2}$$

For any point on the linear manifold of (E.2), let  $s$  be the distance of the point from the origin whose positive direction matches to the positive  $u$ . Then

$$\Delta u = s \cos \theta = \frac{h_2}{\sqrt{h_1^2 + h_2^2}} s \quad \text{and} \quad \Delta v = s \sin \theta = -\frac{h_1}{\sqrt{h_1^2 + h_2^2}} s$$

$$\therefore u = \frac{h_2}{\sqrt{h_1^2 + h_2^2}} s \quad \text{and} \quad v = \frac{x}{h_2} - \frac{h_1}{\sqrt{h_1^2 + h_2^2}} s \tag{E.3}$$

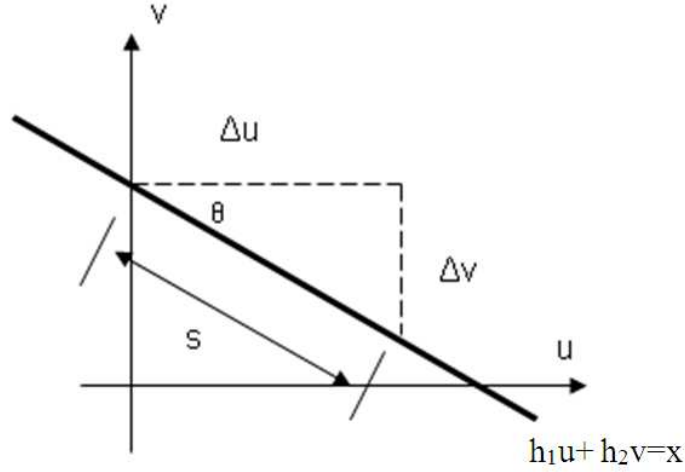


Figure E.1 Top view of linear combination of two random variables

Plugging (E.3) into (E.1), we have

$$f_{s,x}(s, x) = \frac{1}{2\pi\sqrt{1-\rho^2}} \exp\left(-\frac{1}{2(1-\rho^2)} g(s, x)\right) \quad (\text{E.4})$$

where

$$g(s, x) = \frac{h_2^2}{h_1^2 + h_2^2} s^2 - 2\rho \frac{h_2 s}{\sqrt{h_1^2 + h_2^2}} \left( \frac{x}{h_2} - \frac{h_1 s}{\sqrt{h_1^2 + h_2^2}} \right) + \left( \frac{x}{h_2} - \frac{h_1 s}{\sqrt{h_1^2 + h_2^2}} \right)^2$$

$g(s, x)$  of (E.4) is rearranged as

$$g(s, x) = \frac{h_1^2 + 2\rho h_1 h_2 + h_2^2}{h_1^2 + h_2^2} s^2 - \frac{2}{\sqrt{h_1^2 + h_2^2}} \left( \rho + \frac{h_1}{h_2} \right) s x + \left( \frac{1}{h_2} \right)^2 x^2 \quad (\text{E.5})$$

Let  $a \equiv \frac{h_1^2 + 2\rho h_1 h_2 + h_2^2}{h_1^2 + h_2^2}$ ,  $b \equiv \frac{1}{\sqrt{h_1^2 + h_2^2}} \left( \rho + \frac{h_1}{h_2} \right)$ , then

$$\begin{aligned} g(s, x) &= as^2 - 2bsx + \left( \frac{1}{h_2} \right)^2 x^2 = a \left( s - \frac{b}{a} x \right)^2 + \left( \left( \frac{1}{h_2} \right)^2 - \frac{b^2}{a} \right) x^2 \\ &= a \left( s - \frac{b}{a} x \right)^2 + \frac{1 - \rho^2}{h_1^2 + 2\rho h_1 h_2 + h_2^2} x^2 \end{aligned} \quad (\text{E.6})$$

Subsequently, we have

$$\begin{aligned} f_{s,x}(s, x) &= \frac{1}{2\pi\sqrt{1-\rho^2}} \exp \left( -\frac{1}{2(1-\rho^2)} \left[ a \left( s - \frac{b}{a} x \right)^2 + \frac{1-\rho^2}{h_1^2 + 2\rho h_1 h_2 + h_2^2} x^2 \right] \right) \\ &= \frac{1}{\sqrt{2\pi a}} \exp \left( -\frac{x^2}{2(h_1^2 + 2\rho h_1 h_2 + h_2^2)} \right) \frac{1}{\sqrt{2\pi \frac{1-\rho^2}{a}}} \exp \left( -\frac{1}{2 \frac{1-\rho^2}{a}} \left( s - \frac{b}{a} x \right)^2 \right) \end{aligned} \quad (\text{E.7})$$

Therefore

$$\begin{aligned} P_x(x) &= \int_{-\infty}^{\infty} f_{s,x}(s, x) ds \\ &= \frac{1}{\sqrt{2\pi a}} \exp \left( -\frac{x^2}{2(h_1^2 + 2\rho h_1 h_2 + h_2^2)} \right) \int_{-\infty}^{\infty} \frac{1}{\sqrt{2\pi \frac{1-\rho^2}{a}}} \exp \left( -\frac{1}{2 \frac{1-\rho^2}{a}} \left( s - \frac{b}{a} x \right)^2 \right) ds \quad (\text{E.8}) \\ &= \frac{1}{\sqrt{2\pi a}} \exp \left( -\frac{x^2}{2(h_1^2 + 2\rho h_1 h_2 + h_2^2)} \right) \end{aligned}$$

It has been just shown that the linear combination of two random variables of the



bivariate normal distribution ( $x = h_1u + h_2v$ ) also has a normal distribution. Expansion of this result to ‘N’ dimension is simple. Let  $(x_1, x_2, \dots, x_N)$  to be a set of random variables from a multivariate normal distribution and random variable  $x$  is its linear combination

$$x = h_1x_1 + h_2x_2 + \dots + h_Nx_N \quad (\text{E.9})$$

Based on the result of two random variables,  $h_1x_1 + h_2x_2$  has a normal distribution. Therefore  $(h_1x_1 + h_2x_2) + h_3x_3$  is also normally distributed. By applying the same operation consecutively,  $x$  is easily shown to have a normal distribution. This proves that a linear combination of normally distributed random variables has a normal distribution even when the random variables are correlated.

## Appendix F

### Magnetometer measurements on the highway (I-75, Michigan)

To assess disturbance levels in real road circumstances, a vehicle is driven on the Michigan highway (I-75) for 5 hours. Several data were collected during the trip and the total data length is 50 minutes. Figure F.1 shows the plot of the magnetic field norm by concatenating piece-wise data.

The deviation of the magnetic field norm from unity is considered as disturbance. Data of the first half contain less noise than the other half because they were collected in quiet circumstances. In other words, highway traffic of the first half of data collection was much lower than the later part of collection. The red dotted lines of the figure represent  $\pm 0.05$  envelopes from unity. Let’s define the area where the magnetic field norm lies inside of the envelope as ‘useful’ area. The magnetic fields of the ‘useful’ area are considered as clean signals, hence are good to be used for the Heading Kalman filter. The percentages of time occupied by the ‘useful’ area are calculated according to the envelope size (Table F.1). If the envelope is tightened to  $\pm 0.01$ , the Heading Kalman

filter would have measurement updates only for 65 % of the time. However, with the tight envelope, the magnetometer measurements would be very clean for usage. If the envelope is  $\pm 0.05$ , the measurements are utilized for 98 % of the time. In this case the Kalman filter would suffer from the contaminated error. After several trials and error, the author selected  $\pm 0.015$  as the threshold, then the ‘useful’ area takes roughly 80% of running time. This threshold is the optimal number by considering the percentage of the ‘useful’ area and noise levels. This is why the simulated disturbance has 20% of occurrence time.

Table F.1 Percentage of the ‘useful’ area

Envelop Size	0.01	0.02	0.03	0.05
% of ‘useful’ area	65	86	94	98

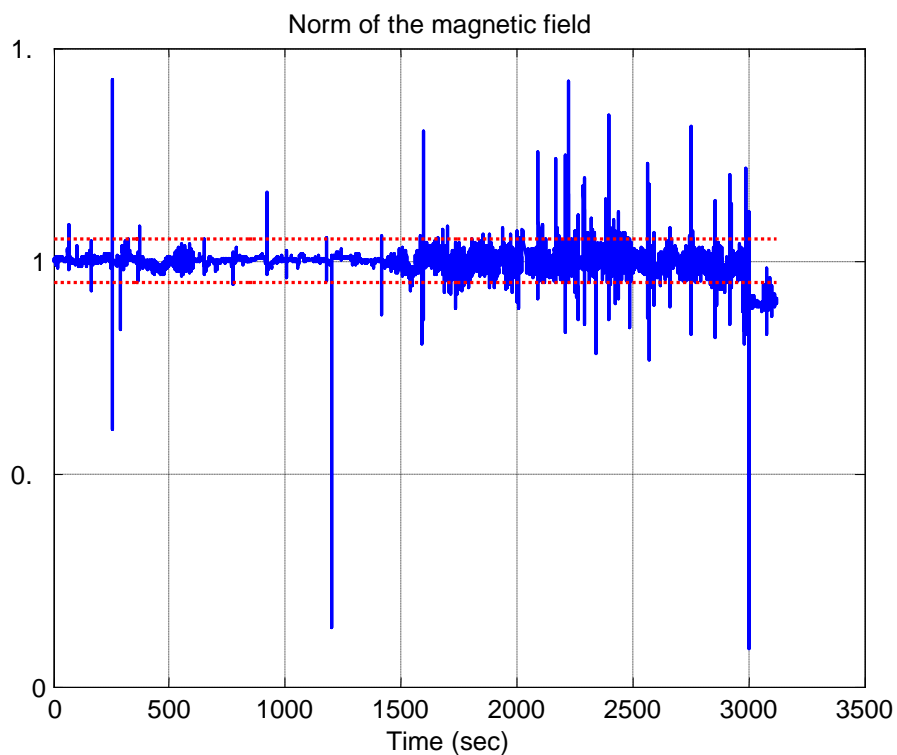


Figure F.1 Norm of the magnetic field collected on a section of Michigan highway (I-75)

## BIBLIOGRAPHY

- [1] Gebre-Egziabher, "DESIGN AND PERFORMANCE ANALYSIS OF A LOW-COST AIDED DEAD RECKONING NAVIGATOR," Doctor of Philosophy, Department of Aeronautics and Astronautics, Stanford University, 2004.
- [2] N. H. T. S. Administration, "Federal Motor Vehicle Safety Standards; Electronic Control Systems; Controls and Displays," vol. 72, N. H. T. S. Administration, Ed., ed, 2007, pp. 17236-17322.
- [3] N. H. T. S. Administration, "Light-Duty Vehicle Greenhouse Gas Emission Standards and Corporate Average Fuel Economy Standards," vol. 75, N. H. T. S. Administration, Ed., ed, 2010, pp. 25324-25728.
- [4] N. H. T. S. Administration, "Vehicle Weight, Fatality Risk and Crash Compatibility of Model Year 1991-99 Passenger Cars and Light Trucks," N. H. T. S. Administration, Ed., ed, 2003.
- [5] T. D. Gillespie, *Fundamentals of Vehicle Dynamics*. Warrendale, PA: Society of Automotive Engineers, Inc., 1992.
- [6] J. Farrelly and P. Wellstead, "Estimation of Vehicle Lateral Velocity," in *IEEE International Conference on Control Applications*, Dearborn, MI, USA, 1996, pp. 552-557.
- [7] U. Kiencke and A. Daiss, "Observation of Lateral Vehicle Dynamics," *Control Engineering Practice*, vol. 5, pp. 1145-1150, 1997.
- [8] M. C. Best, *et al.*, "An Extended Adaptive Kalman Filter for Real-time State Estimation of Vehicle Handling Dynamics," *Vehicle System Dynamics*, vol. 34, pp. 57-75, 2000.
- [9] J. Stephan, *et al.*, "Virtual Sensor: Application to Vehicle Sideslip Angle and Transversal Forces," *IEEE Transactions on Industrial Electronics*, vol. 51, pp. 278-289, 2004.
- [10] H. Cherouat, *et al.*, "Vehicle velocity, side slip angles and yaw rate estimation," presented at the IEEE ISIE, Dubrovnik, Croatia, 2005.
- [11] P. Yih, *et al.*, "Vehicle State Estimation using Steering Torque," in *Proceeding of the 2004 American Control Conference*, Boston, Massachusetts, 2004.
- [12] X. Gao and Z. Yu, "Vehicle Sideslip Angle Estimation by using High Gain Observer," in *AVEC 9th International Symposium on Advanced Vehicle Control*, Kobe, Japan, 2008.
- [13] H. F. Grip, *et al.*, "Nonlinear Vehicle Side-Slip Estimation with Friction Adaptation," *Automatica*, vol. 44, pp. 611-622, 2008.

- [14] D. Piyabongkarn, *et al.*, "Development and Experimental Evaluation of A Slip Angle Estimator for Vehicle Stability Control," in *Proceeding of the 2006 American Control Conference*, Minneapolis, Minnesota, 2006.
- [15] L. Li, *et al.*, "A Robust Observer Designed for Vehicle Lateral Motion Estimation," in *IEEE proceedings on Intelligent Vehicle Symposium*, 2005, pp. 417-422.
- [16] L. Imsland, *et al.*, "Vehicle Velocity Estimation using Modular Nonlinear Observers," *Automatica*, vol. 42, pp. 2091-2103, 2006.
- [17] A. Y. Ungoren, *et al.*, "Experimental Verification of Lateral Speed Estimation Methods," in *AVEC 6th International Symposium on Advanced Vehicle Control*, Hiroshima, Japan, 2002.
- [18] Y. Fukada, "Slip-Angle Estimation for Vehicle Stability Control," *Vehicle System Dynamics*, vol. 32, pp. 375-388, 1999.
- [19] A. Nishio and K. Tozu, "Development of Vehicle Stability Control System Based on Vehicle Sideslip Angle Estimation," presented at the SAE, New York, 2001.
- [20] D. M. Bevly, "Global Positioning System (GPS): A Low-Cost Velocity Sensor for Correcting Inertial Sensor Errors on Ground Vehicles," *Journal of Dynamic System, Measurement, and Control*, vol. 126, pp. 255-264, 2004.
- [21] D. M. Bevly, *et al.*, "Estimation of Critical Tire Parameters Using GPS Based Sideslip Measurements," presented at the SAE International, 2005.
- [22] D. M. Bevly, *et al.*, "The Use of GPS Based Velocity Measurements for Measurement of Sideslip and Wheel slip," *Vehicle System Dynamics*, vol. 38, pp. 127-147, 2003.
- [23] D. M. Bevly, *et al.*, "Integrating INS sensors with GPS Measurements for Continuous Estimation of Vehicle Sideslip, Roll and Tire Cornering Stiffness," *IEEE Transactions on Intelligent Transportation Systems*, vol. 7, pp. 483-493, 2006.
- [24] R. Anderson and D. M. Bevly, "Estimation of Slip Angles using a Model Based Estimator and GPS," in *Proceeding of the 2004 American Control Conference*, Boston, Massachusetts, 2004.
- [25] D. Hrovat, *et al.*, "VEHICLE DYNAMIC MEASURING APPARATUS AND METHOD USING MULTIPLE GPS ANTENNAS," USA Patent, Dec. 30, 2003, 2003.
- [26] J. A. Farrell, *et al.*, "Carrier Phase GPS-Aided INS-Based Vehicle Lateral Control," *Journal of Dynamic System, Measurement, and Control*, vol. 125, pp. 339-353, 2003.
- [27] N. G. Survey. *Continuously Operating Reference Station*. Available: <http://www.ngs.noaa.gov/CORS/>
- [28] J. Ryu and J. C. Gerdes, "Integrating Inertial Sensors with GPS for Vehicle Dynamics Control," *Journal of Dynamic System, Measurement, and Control*, vol. 126, pp. 243-254, 2004.
- [29] J. Ryu, *et al.*, "Vehicle Sideslip and Roll Parameter Estimation Using GPS," in *AVEC 6th International Symposium on Advanced Vehicle Control*, Hiroshima, Japan, 2002.
- [30] H. Blomenhofer, *et al.*, "Development of a Real-Time DGPS System in the Centimeter Range," presented at the IEEE PLANS, Las Vegas, NV, 1994.

- [31] S. Bajikar, *et al.*, "Evaluation of In-Vehicle GPS-Based Lane Position Sensing for Preventing Road Departure," presented at the Proceedings of the IEEE Conference on Intelligent Transportation Systems, Boston, MA, 1997.
- [32] E. D. Kaplan and C. J. Hegarty, *Understanding GPS: principles and applications*, 2nd ed. Norwood, MA: Artech House, 2006.
- [33] J. Ryu, "STATE AND PARAMETER ESTIMATION FOR VEHICLE DYNAMICS CONTROL USING GPS," Doctor of Philosophy, Department of Mechanical Engineering, Stanford University, 2004.
- [34] L. J. Adams, *The Global Positioning System*. Washington, D.C.: National Academy Press, 1995.
- [35] B. W. Parkinson and J. J. Spilker Jr., *Global Positioning System: Theory and Applications* vol. 2. Washington, D.C.: American Institute of Aeronautics and Astronautics, Inc., 1996.
- [36] J.-A. Avila-Rodriguez, *et al.*, "Revised Combined GALILEO/GPS Frequency and Signal Performance Analysis," in *ION GNSS*, Long Beach, CA, 2005.
- [37] J. Furthner, *et al.*, "Time Dissemination and Common View Time Transfer with Galileo: How Accurate Will It Be?," presented at the 35th Annual Precise Time and Time Interval Meeting, San Diego, CA, 2003.
- [38] K. O'Keefe, *et al.*, "Global Availability and Reliability Assessment of the GPS and Galileo Global Navigation Satellite Systems," *Canadian Aeronautics and Space Journal*, vol. 48, 2002.
- [39] C. Seynat, *et al.*, "A Performance Analysis of Future Global Navigation Satellite Systems," *Journal of Global Positioning Systems*, vol. 3, pp. 232-241, 2004.
- [40] S. Verhagen, "Performance Analysis of GPS, Galileo and Integrated GPS-Galileo," in *15th International Technical Meeting of the Satellite Division of the Institute of Navigation*, Portland, OR, 2002, pp. 2208-2215.
- [41] PriceGrabber.com. (2007, *Consumer Behavior Report; GPS Pricing Trends*. Available: [https://mr.pricegrabber.com/2007\\_GPS\\_Pricing\\_Trends\\_Report.pdf](https://mr.pricegrabber.com/2007_GPS_Pricing_Trends_Report.pdf)
- [42] R. Stengel, *Optimal Control and Estimation*. New York: Dover Publications, Inc., 1994.
- [43] V. L. Bageshwar, *et al.*, "A Stochastic Observability Test for Discrete-Time Kalman Filters," *Journal of Guidance, Control, and Dynamics*, vol. 32, 2009.
- [44] B. Delyon, "A Note on Uniform Observability," *IEEE Transactions on Automatic Control*, vol. 46, pp. 1326-1327, 2001.
- [45] J. Deyst, John J., "Correction to "Conditions for Asymptotic Stability of the Discrete Minimum-Variance Linear Estimator"," *IEEE Transactions on Automatic Control*, vol. 18, pp. 562-563, 1973.
- [46] J. Deyst, John J. and C. F. Price, "Conditions for Asymptotic Stability of the Discrete Minimum-Variance Linear Estimator" *IEEE Transactions on Automatic Control*, vol. AC-13, pp. 702-705, 1968.
- [47] K. Reif, *et al.*, "Stochastic Stability of the Discrete-Time Extended Kalman Filter," *IEEE Transactions on Automatic Control*, vol. 44, pp. 714-728, 1999.
- [48] H. W. Sorenson, "On the Error Behavior in Linear Minimum Variance Estimation Problems," *IEEE Transactions on Automatic Control*, vol. 12, pp. 557-562, 1967.
- [49] A. H. Jazwinski, *Stochastic processes and filtering theory*. New York: Academic Press, 1970.

- [50] R. Daily and D. M. Bevly, "The Use of GPS for Vehicle Stability Control Systems," *IEEE Transactions on Industrial Electronics*, vol. 51, 2004.
- [51] I. Y. Bar-Itzhack and Y. Vitek, "The Enigma of False Bias Detection in a Strapdown System During Transfer Alignment," *J. Guidnace*, vol. 8, pp. 175-180, 1985.
- [52] G. H. Elkaim, *et al.*, "Comparison of Low-Cost GPS/INS Sensors for Autonomous Vehicle Applications," in *2008 IEEE/ION Position, Location and Navigation Symposium*, 2008, pp. 1133-1144.
- [53] D. T. Knight, "Achieving Modularity with Tightly-Coupled GPS/INS," in *Proceeding of the IEEE Plans '92*, Monterey, California, 1992, pp. 426-432.
- [54] B. Li, *et al.*, "A GPS-Slaved Time Synchronization System for Hybrid Navigation," *GPS Solutions*, vol. 10, pp. 207-217, 2006.
- [55] Q. Li and D. Rus, "Global Clock Synchronization in Sensor Networks," *IEEE Transactions on Computers*, vol. 55, pp. 214-226, 2006.
- [56] I. Skog and P. Handel, "A Low-Cost GPS Aided Inertial Navigation System for Vehicle Applications," in *Proceeding of EUSIPCO 2005*, Antalya, Turkey, 2005.
- [57] I. Skog and P. Handel, "Effects of Time Synchronization Errors in GNSS-aided INS," in *Proceedings of Position, Location and Navigation Symposium*, Monterey, California, 2008.
- [58] T. D. Larsen, *et al.*, "Incorporation of time delayed measurements in a Discrete-time Kalman Filter," in *Proceedings of the 37th IEEE conference on Decision & Control*, Tampa, Florida, 1998, pp. 3972-3977.
- [59] R. M. Eustice, *et al.*, "Visually Augmented Navigation for Autonomous Underwater Vehicles," *IEEE Journal of Ocean Engineering*, vol. 33, pp. 103-122, 2008.
- [60] D. Stefanica, *A Primer for the Mathematics of Financial Engineering*. New York: FE Press, 2008.
- [61] T. S. Kinjawadekar, "Model-Based Design of Electronic Stability Control System for Passenger Car Using Carsim and Matlab-Simulink," Master of Science, Department of Mechanical Engineering, The Ohio State University, 2009.
- [62] S. M. Arndt, *et al.*, "Effectiveness of Electronic Stability Control on Maintaining Yaw Stability When an SUV has a Rear Tire Tread Separation," presented at the SAE, 2009.
- [63] R. Anderson and D. M. Bevly, "Estimation of Tire Cornering Stiffness using GPS to Improve Model Based Estimation of Vehicle States," in *IEEE proceedings on Intelligent Vehicle Symposium*, Las Vegas, Nevada, 2005.
- [64] D. J. Broderick, *et al.*, "Modeling Vehicle Lateral Dynamics By Gaussian Processes," in *Dynamic System Control Conference*, Boston, MA, 2010.
- [65] C.-S. Liu and H. Peng, "A State and Parameter Identification Scheme for Linearly Parameterized Systems," *ASME Journal of Dynamics, Measurement and Control*, vol. 120, pp. 524-528, 1998.
- [66] J.-H. Yoon and H. Peng, "Vehicle Sideslip Angle Estimation Using Two Single-Antenna GPS Receivers," in *Dynamic System Control Conference*, Boston, MA, 2010.

- [67] J. Zuurbier and P. Bremmer, "State Estimation for Integrated Vehicle Dynamics Control," in *AVEC 6th International Symposium on Advanced Vehicle Control*, Hiroshima, Japan, 2002.
- [68] H. E. Tseng, "Dynamic Estimation of Road Bank Angle," *Vehicle System Dynamics*, vol. 36, pp. 307-328, 2001.
- [69] J.-O. Hahn, *et al.*, "Road Bank Angle Estimation Using Disturbance Observer," in *AVEC 6th International Symposium on Advanced Vehicle Control*, Hiroshima, Japan, 2002.
- [70] J.-O. Hahn, *et al.*, "Real-Time Identification of Road-Bank Angle Using Differential GPS," *IEEE Transactions on Control Systems Technology*, vol. 12, pp. 589-599, 2004.
- [71] J. Ryu and J. C. Gerdes, "Estimation of Vehicle Roll and Road Bank Angle," in *Proceeding of the 2004 American Control Conference*, Boston, Massachusetts, 2004.
- [72] J. L. Crassidis and E. G. Lightsey, "Attitude Determination Using Combined GPS and Three-Axis Magnetometer Data," *Space Technology, Journal of the International Forum on Automatic Control*, vol. 20, pp. 147-156, 2001.
- [73] G. A. Borges, *et al.*, "An IMU/Magnetometer/GPS-based localization system using correlated Kalman Filtering," presented at the XVII Congresso Brasileiro de Automatica, 2008.
- [74] S. Taghvaeeyan and R. Rajamani. (2001, Use of vehicle magnetic signatures for position estimation. *Applied Physics Letters* 99(134101).
- [75] E. Abbott and J. D. Powell, "Land-Vehicle Navigation Using GPS," in *Proceedings of the IEEE*, 1999, pp. 145-162.
- [76] P. Ripka, *Magnetic sensors and magnetometers*: Artech House, 2001.
- [77] B. R. Barmish and C. M. Lagoa, "The Uniform Distribution: A Rigorous Justification for its use in Robustness Analysis," *Mathematics of Control, Signals, and Systems*, vol. 10, pp. 203-222, 1997.
- [78] M. Prandini and M. C. Campi, "A new approach to controller design in presence of constraints," in *IEEE Conference on Decision and Control*, New Orleans, LA, USA, 2007.
- [79] M. L. Muhler and B. R. Barmish, "A Uniformity Principle for Probabilistic Robustness of the Discrete-Time Linear Quadratic Regulator," in *American Control Conference*, San Diego, CA, 1999.
- [80] M. S. Grewal and A. P. Andrews, *Kalman Filtering: Theory and Practice*: Prentice-Hall, Inc., 1993.
- [81] Y. Bar-Shalom, *et al.*, *Estimation with Application to Tracking and Navigation: Theory Algorithms and Software*: Wiley-Interscience, 2001.